Optical and Magneto-Optical Properties of type-II Excitons in ZnTe/ZnSe Stacked Submonolayer Quantum Dots

by

Bidisha Roy

A dissertation submitted to the Graduate Faculty in Physics
in partial fulfillment of the requirements for the degree of
Doctor of Philosophy, The City University of New York

2013

Optical and Magneto-Optical Properties of type-II Excitons in ZnTe/ZnSe Stacked Submonolayer Quantum Dots

This manuscript has been read and accepted for the Graduate Faculty in Physics in satisfaction of the dissertation proposal requirements for the degree of Doctor of Philosophy.

Professor Igor L. Kuskovsky

Date

Chair of Examining Committee

Professor Steven Greenbaum

Date

Executive Officer

Professor Maria C. Tamargo

Professor Vinod M. Menon

Professor Lev Murokh

Doctor Shiping Guo

Supervisory Committee

THE CITY UNIVERSITY OF NEW YORK

Abstract

Optical and Magneto-Optical Properties of type-II Excitons in ZnTe/ZnSe Stacked
Submonolayer Quantum Dots

by

Bidisha Roy

Adviser: Professor Igor L. Kuskovsky

In this thesis we plan to develop understanding of the fundamental physical and material properties of type-II excitons in stacked ZnTe/ZnSe submonolayer quantum dots (QDs). The samples, grown via combination of molecular beam epitaxy (MBE) and migration enhanced epitaxy (MEE) are studied using photoluminescence (PL), time-resolved PL (TRPL) and PL in external magnetic field (Magneto-PL) as well as Magneto-TRPL. This thesis aims to discuss the key realizations keeping in mind the fundamental and advanced interests for such and related systems.

In the first part of the thesis, effects of varying two crucial MBE growth parameters on the size and composition of the QDs are studied via detailed optical characterization with the goal of attaining better control over intentional growth.

The second part of the thesis is focused on the magneto-optical studies, wherein observation of the optical excitonic Aharonov-Bohm (AB) effect in these type-II QD system has been discussed in details. The AB phase is revealed via the optical emission in magnetic field, observed as oscillation (AB ‘peak’) in PL intensity. Presence of built-in electric field in the system is indicated from the narrow and robust AB oscillations. Detailed spectral analysis of the AB peak enabled us to determine lateral excitonic size with sub-nanometer precision as well as distinguish the presence of different QD stacks of the submonolayer QDs in the ensemble system.

Magneto-time resolved PL measurements were performed to understand the influence of AB effect on the lifetime of magneto excitons due to transitions of angular momentum between optically “bright” and “dark” excitonic states. Our understandings have been discussed to the extent of the achieved results.

Acknowledgments

When I joined the Ph.D. program in Physics, I practically didn't know about the real challenges that I was going to face. Neither did I know that I'll find wonderful people along the way who will make the journey a great lesson filled with scientific knowledge as well as living perspectives for my personal growth.

I was only fortunate to have found Prof. Igor Kuskovsky as my PhD. adviser. He has been the strongest guiding force during my past few years of learning- to do science and to appreciate that failures and successes are all 'educational' in their own ways. Like a great teacher, he played the role of being the biggest critic as well as the biggest source of encouragement for me. I am indebted to him for everything I acquired through knowing him- scientific, technical and philosophical, but especially for being the personality who influenced me in the most constructive ways. I believe I will be able to carry forth some of his vision, wherever I go in life.

It has been a privilege to have known Prof. Vinod Menon since the beginning days of my graduate life. He gave me motivation, patiently took time to help me numerous times in wiping out confusions and 'see' practically both scientific as well as other aspects of various problems that I put forward to him. He is a great mentor and researcher who will remain an example for me and I am grateful to him.

I am thankful to Prof. Maria Tamargo for providing the samples and her collaboration. I am inspired by her passion towards doing active research and on a personal front she has been very supportive and helpful at all occasions of need. Special thanks to Prof. Lev Murokh for many helpful discussions that we had in trying to find insightful physical descriptions to problems. I am extremely grateful to Prof. Fred Cadieu who helped in major ways during the experiments with the superconducting magnet in his lab. He also helped me with various technical issues through the installation and setting up of the 9T superconducting magnet in our lab. I want to sincerely thank Prof. Dmitry Smirnov and Younghee Kim at the National High Magnetic Field Laboratory (NHMFL, Florida), for being immensely helpful during hosting our experiments there.

My sincere thanks to Haojie Ji and Siddharth Dhomkar for making the great team that we are today and for their valued support during the experiments and group activities. I want to thank Weldon Mc.Donald, Dr. Vladimir Shuvayev, Dr. Uttam Manna and Dr. David Goldberg for being helpful at various times with different aspects related to the work presented here. I extend my gratitude to everyone at the Physics Department of Queens College for being a family at work.

I must admit, the ups and downs of this journey wouldn't have been as enjoyable without the great friendship I earned on the way. Dr. Saima Hussaini who continuously gave me much needed positive energy even in the hardest of situations, Zhou Shi and Harish Krishnamoorthy- without their company, sharing and help, I cannot even imagine to have endured the stressful times. I thank Dr. Dario Capasso who has always been available in trying to find a solution to many of my weirdest problems and showed great interest in my research.

I remember my dearest friend Sanchari, who in spite of her fight against Cancer for the last three years, filled my days with 'life' in her most endearing ways. She taught me the spirit of never giving in to adversities. I miss her everyday, but I carry our friendship with me.

At the end I would like to thank the people who make me what I am. My husband Deb, the friend and companion who held me through all the good and worse seasons along the way, he empowers me with his unquestionable love and faith. My brother Bidyut, who is the pillar of strength and backbone to my world- he brings me up every time I fall. My parents, who keep me going with their unconditional support, they give me courage, ambition and purpose. It is to them, my family, that I dedicate this thesis.

I recollect the experiences of my graduate years and quote my favorite author and philosopher, Rabindranath Tagore, while I look forward from here, *"I have become my own version of an optimist. If I can't make it through one door, I'll go through another door - or I'll make a door. Something terrific will come no matter how dark the present."*

This work has been supported by the National Science Foundation under Award No. DMR-1006050.

Contents

List of Tables

List of Figures

Chapter 1

Introduction

"Frequently, I have been asked if an experiment I have planned is pure or applied research; to me it is more important to know if the experiment will yield new and probably enduring knowledge about nature. If it is likely to yield such knowledge, it is, in my opinion, good fundamental research; and this is much more important than whether the motivation is purely esthetic satisfaction on the part of the experimenter on the one hand or the improvement of the stability of a high-power transistor on the other. It will take both types to confer the greatest benefit on Mankind."

–William Shockley, Nobel lecture -1956 (The Nobel prize was awarded for "research on semiconductors and their discovery of the transistor effect")

Motivation

Progress in science and technology at the nano scale has opened up numerous opportunities both for fundamental and applied research which are leading towards envisioning novel devices and advanced applications. Quantum wells (QWs), nanowires (NW), quantum rings (QR), and quantum dots (QDs) are among the most important building blocks of opto-electronic and nano-photonic devices as these lower dimensional structures are capable of modifying the density of states and band structures of the semiconductors which can be engineered as per requirement. Therefore, the understanding of underlying fundamental physical phenomena in such structures is very important for future progress. This work is an effort in the same direction.

Keeping in mind the potential applications in photo-detection and quantum information, we have focused on fundamental properties of wide band gap nanostructured materials, with type-II band alignment. In particular, we study the properties of type-II submonolayer stacked QDs formed in epitaxially grown Zn-Se-Te multilayers.

Zn-Se-Te have well reported material parameters and well understood bulk alloys [1, 2] which possess interesting optical and electronic properties. Generally, the lower dimensional systems are particularly attractive due to their tunable optical properties and prospective applications. For Zn-Se-Te system, e.g. multiple ZnTe/ ZnSe quantum well (QW) and superlattice structures have been grown with the goal of achieving tunable optical properties via quantum confinement effects [3], there are possibilities that doped ZnTe/ ZnSe QDs can lead to development of efficient quantum dot infrared photodetectors (QDIP)[4].

We are particularly interested in ZnTe/ ZnSe based type-II QDs wherein we foresee novel prospects towards quantum information related applications. In general, storage and retrieval of light on demand without corrupting the information it carries, is an important challenge in the field of quantum information processing. Hence research in the areas of efficient optical quantum memory [5–9] and controlled light retardation (slow light) [10–13] has gained a lot of interest lately. In optical quantum computation, the role of quantum memory is to store quantum bits such that operations can be timed appropriately. Quantum memory must be able to store a state long enough to perform a particular task, so storage time is an essential criterion [6].

In this regard, the optical properties demonstrated by excitons in type-II QDs are promising for storage of light due to the spatially separated charge carriers, long radiative lifetimes and suppressed Auger recombination as well as the possibility of tuning a bright excitonic (BE) state into a dark excitonic (DE) state and vice versa via varying the applied electric and magnetic fields. Tuning between BE and DE states can be used as an alternative route to the optical quantum memory along with the advantages of inherent slow decay time and robustness of this effect from these systems. Also, the storage time criterion for efficient optical quantum memory can be challenged by this method because it will depend on the application and tuning of the external fields.

In the ZnTe-ZnSe systems holes are strongly confined within ZnTe, whereas electrons locate in ZnSe barriers, and only weakly attracted to holes via the Coulomb interaction, forming the spatially indirect (type-II) excitons [14, 15]. This leads to relatively long carrier lifetimes and cause dependence of photoemission and photocurrents on the intensity of excitation, as well as on external electric and magnetic fields [15–17]. These properties can be manipulated for new and enhanced materials and devices. By tuning the dot size, chemical composition, and the doping levels, one should be able to adjust the optical transitions to desired wavelengths. Obtaining high quality and controlled growth of QDs with uniform size distribution still remains a challenge, which is one of the prime requirements that may provide adequate spectral response with lesser inhomogeneous broadening.

We have performed optical studies which provide insight to effects of changing growth conditions on the size, composition and density of ZnTe stacked submonolayer QDs in ZnSe matrix.

Also, these type-II QDs exhibit a fundamentally intriguing effect that can be observed in the magnetic field - the excitonic Aharonov-Bohm (AB) effect, which arises from the interaction of the vector potential with the electric dipole. Depending on the strength of the electron-hole coupling, different observations are expected in the magneto-optical properties. We achieved high degree of precision in determining the lateral excitonic size and extracted vital qualitative information about the stacks of these sub-monolayer QDs. A presence of built-in electric field in the system has also been predicted from our studies.

An important consequence of the excitonic AB effect to the radiative carrier dynamics would be its influence on the lifetime of AB excitons and if that can be tuned by the application of additional external fields. This can be a landmark towards obtaining tunability of excitonic data storage in advanced quantum information related areas as mentioned before. We present our relevant understandings.

This thesis is divided into three main parts. In the first part we discuss the relevant background information, in the second part we present the results of Optical and magneto-Optical studies and in the third part we discuss some unresolved issues with future scopes of research.

1.1 Background

1.1.1 Semiconductor Heterostructures and Band Alignment

A heterojunction is formed when two dissimilar semiconductors are joined adjacent to one another and heterostructures are formed from multiple heterojunctions. This concept brought in ground breaking development in the world of semiconductors for the properties of devices can now be engineered by changing material composition as per requirement and it is possible to confine electronic states by producing lower dimensional systems. The Nobel prize in 2000 was awarded in the field of developing "semiconductor heterostructures used in high-speed- and opto-electronics", which followed tremendous increase in the research in low dimensional heterostructures. Semiconductor heterostructures have found many practical applications since then. Heterostructure-based electronic devices are widely used in many areas of daily human activities e.g. telecommunication systems utilizing double-heterostructure(DH) lasers, light-emitting diodes (LEDs) and bipolar transistors, low-noise, high-electron-mobility transistors used in high-frequency devices, DH laser has been used as part of the compact disk (CD) player ([18] and references there in). At larger scales, solar cells incorporating heterostructures are used extensively in both space and terrestrial programs [18]. Semiconductor heterostructures can also be used for advanced electronic devices (e.g., modulation-doped field-effect transistors [19], heterojunction bipolar transistors [20, 21], resonant tunneling devices [22]), optical and photonic components (e.g., waveguides, mirrors, microresonators)[23–25], and optoelectronic devices and structures (e.g. laser diodes, photodetectors, biological sensors etc.) [26–29]. Perhaps the most important technological aspect is that they can be used for electronic, photonic, and optoelectronic purposes, and hence may allow the integration of all of these for further sophisticated device applications. In this section we briefly introduce to this powerful concept.

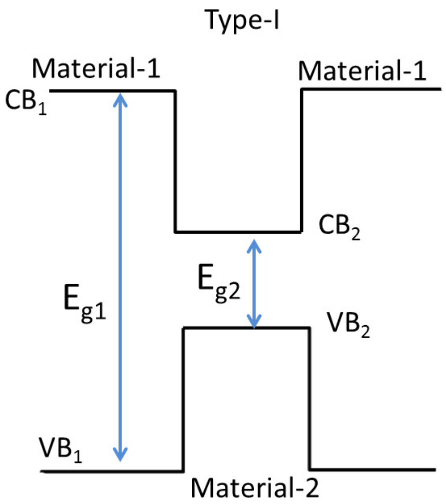

Figure 1.1: Type-I band alignment: Minimum of conduction band (CB2) and maximum of valence band (VB2)of smaller band gap material (material-2, in this case) lies within that of the larger band gap material-1

Within the effective mass approximation, the Schrödinger equation is followed by the charge carriers in a semiconductor, while when a heterojunction is formed, then the equation is valid within each (we note that the effective mass could be a function of position). The bandgaps of the materials can also be different. The discontinuity in either the conduction or the valence band can be treated by a constant potential term in the Schrödinger equation. The electronic properties which depend largely on the band offsets and on the bulk properties of the constituting materials, abruptly change at the interface.

Semiconductor heterostructures can be broadly divided into two groups on the basis of their band alignments. When the band gap of one material is completely nestled within that of the wider- band gap material; consequently both types of carriers are confined into the lower potential wells which are within the same material- such a band alignment is classified as type-I. A schematic of the type-I band alignment is shown in Figure 1.1.

In type-II band alignment, however, the band gaps of the materials are staggered such that material with the lower potential energy for electrons has the higher potential energy for holes and vice versa. (A schematic of two possible cases for type-II

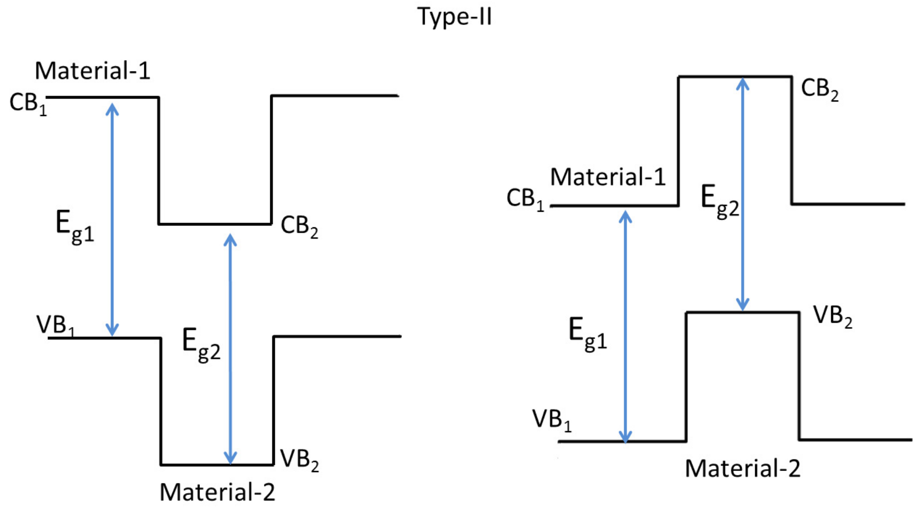

Figure 1.2: Type-II band alignment: This is a staggered configuration where two cases can be seen as shown above; one material acts as potential well for electrons and barrier for holes and the other material acts vice versa. The effective band gap is comprised by the energy difference between the lowest conduction band edge and highest valence band edge.

band alignment is shown in Figure 1.2).

This leads to the spatial separation of electrons and holes giving rise to an electric field that bends the conduction and valence bands and modifies energy levels and wavefunctions of the carriers. We note here that this ‘indirectness’ is only in the real space, in k-space the band gap can be still direct. However, a reduced overlap of electron and hole wavefunctions as compared to that in type-I heterostructures is natural in type-II systems. These structures can be especially useful for long wavelength opto-electronic applications because the effective band gap (comprised by the energy difference between the lowest conduction band edge and highest valence band edge) can be acquired to be very small. Such a band alignment offers more scope to band engineering because the carrier confinement now depends on the band offsets of the comprising materials rather than the band gap of each material.

In this thesis we concentrate on such a system with type-II band alignment and hence in the later sections we will discuss the signature properties of type-II structures in low dimensional regimes.

1.1.2 Quantum Confinement

When electrons and holes are confined by potential barriers to small regions of space where the dimensions of the confinement are comparable to the de Broglie wavelength of these charge carriers, pronounced quantisation effects develop. Semiconductor heterostructures keep the structural features of their bulk state while the electronic properties which depend on the density of states change as a function of the dimensionality. In general, charge carriers in semiconductors can be confined by potential barriers in one, two, or three spatial dimensions.

A three-dimensional bulk material can be modelled as an infinite crystal along all three dimensions. The periodic boundary conditions yield standing waves as solutions of the Schrödinger equation for free electrons. The energy of free electrons in bulk solids scales with the square of the k- wave vectors in the three dimensions, corresponding to a parabolic dependence on k. When one (QW-case) or two (QWR-case) of the three dimensions are reduced to order of nano-scales, charge carriers are confined along those one or two dimensions which results in corresponding quantization of the k vectors and modification of density of states and energy distribution (as shown in Figure 1.3).

When the charge carriers are confined in all the three dimensions (QD-case); each individual state can be represented by a point in the k-space. As a consequence, the energy bands converge to atom-like discrete energy states, which leads to the emergence of delta function peaks in the electronic density of states. Figure 1.3 shows the modifications of density of states $N(E)$ as a consequence of confinement from (a) bulk, to (b) 1-D, (c) 2-D and (d) 3-D confinements, for QWs, quantum wires (QWRs) and QDs (shown for the confined carrier only), respectively.

1.1.3 Excitons in Semiconductors

Exciton is a ‘quasiparticle’ concept, widely used in optics of semiconductors and central to understanding light-matter interaction. It can be simply described as an electron and hole pair created via excitation (e.g. by a photon) and bound together through their attractive Coulomb interaction. An exciton can move through the

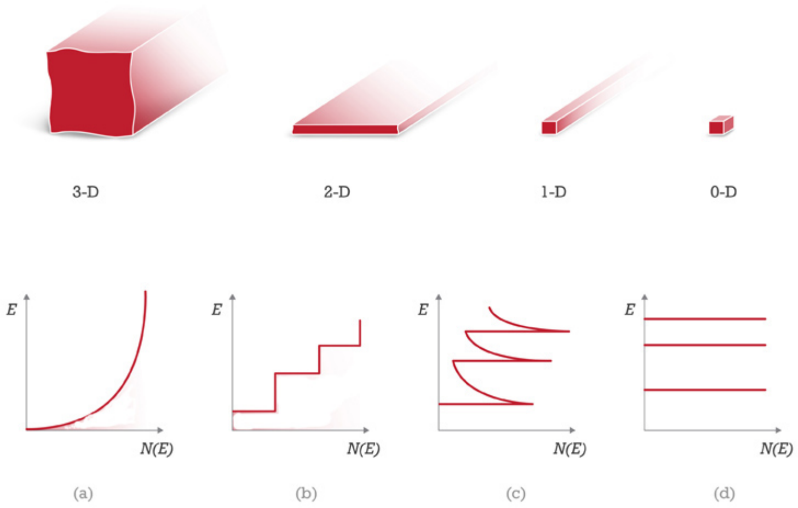

Figure 1.3: Density of states N(E) for (a) bulk semiconductor (3-D), (b) quantum well (2-D), (c) quantum wire (1-D), and (d) quantum dot (0-D).

crystal and can transport energy; it does not transport charge because it is electrically neutral.

There are two types of excitons that can be formed in non-metallic solids, namely Wannier-Mott excitons [30] and Frenkel excitons [31, 32]. Frenkel excitons generally occur in organic crystals where the electron-hole interaction is strong (Binding energy $\sim$ 100 to 300 meV) due to their close proximity ; exciton size (Bohr radius $\sim$ 10 Å) is on the order of unit cell. The concept of Wannier-Mott excitons is generally valid for inorganic semiconductors with generally small carrier effective masses, because these materials have high dielectric constants that reduce the Coulomb interaction between the electron and hole due to screening. Also the overlap of interatomic electronic wavefunctions enables the electrons and holes to be far apart but bound in an excitonic state. The Wannier excitons have larger size (Bohr radius of the order of tens of lattice constants, typically $\sim$ 30 - 100 Å) and smaller binding energies ($\sim$ 10 - 30 meV).

We focus our discussion on the Wannier-Mott excitons, which can be viewed as an effective hydrogen atom with the hole establishing the coordinate reference frame about which the reduced mass electron moves.

The time-independent Schrödinger's equation for an exciton can be written as:

$$\widehat{\mathbf{H}}\Phi(\mathbf{r_e},\mathbf{r_h}) = E\Phi(\mathbf{r_e},\mathbf{r_h}) \tag{1.1}$$

where the Hamiltonian operator, $\widehat{\mathbf{H}}$, in a semiconducting material with a zero-frequency dielectric constant of ε, can be written as:

$$\widehat{\mathbf{H}} = -\frac{\hat{\mathbf{p}}_{\mathbf{h}}^2}{2m_h} - \frac{\hat{\mathbf{p}}_{\mathbf{e}}^2}{2m_e} - \frac{e^2}{\varepsilon\left|\mathbf{r_e}-\mathbf{r_h}\right|} \tag{1.2}$$

where e is the charge of an electron, and $\hat{\mathbf{p}}_{\mathbf{e(h)}}$, $m_{e(h)}$, $\mathbf{r_{e(h)}}$, are the momentum operator, mass of electron (hole) and position vector of the electron (hole).

The Hamiltonian is similar to that of the hydrogen atom; therefore, the exciton is said to be a hydrogen-like particle. By applying the center-of-mass, and relative coordinate transformation:

$$\mathbf{R} = \frac{m_e\mathbf{r_e} + m_h\mathbf{r_h}}{m_e + m_h} \tag{1.3a}$$

$$\mathbf{r} = \mathbf{r_e} - \mathbf{r_h} \tag{1.3b}$$

the Schrödinger's equation in equation 1.1 transforms into two equations where the center-of-mass, and relative coordinates are decoupled:

$$-\frac{\hbar^2}{2M}\nabla_{\mathbf{R}}^2\psi(\mathbf{R}) = E_R\psi(\mathbf{R}) \tag{1.4a}$$

$$\left(-\frac{\hbar^2}{2\mu}\nabla_{\mathbf{r}}^2 - \frac{e^2}{\varepsilon r}\right)\phi(\mathbf{r}) = E_r\phi(\mathbf{r}) \tag{1.4b}$$

where μ is the reduced mass defined by, $\frac{1}{\mu} = \frac{1}{m_e} + \frac{1}{m_h}$.

Equation 1.4a is the Schrödinger's equation for a free particle which gives energy:

$$E_R = \frac{\hbar^2k^2}{2M} \tag{1.5}$$

where k is the wave number of the exciton. Equation 1.4b leads to energy quantization giving the total exciton energy as:

$$E_n = E_{gap} + \frac{\hbar^2k^2}{2M} - \frac{R_y^*}{n^2} \tag{1.6}$$

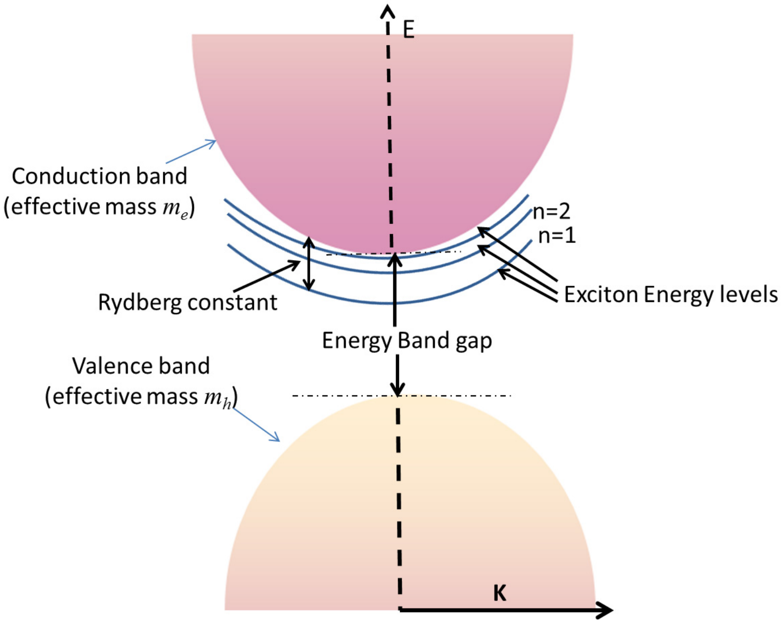

Figure 1.4: Semiconductor band structure with exciton energy levels.

where R_y^* is the Rydberg constant for the exciton defined by $R_y^* = \mu e^4 / 2\hbar^2 \varepsilon^2$. A schematic of the exciton energy levels is shown in figure 1.4.

We note that in the event of photon generated excitons, due to wave vector conservation, k should be equal to the photon wavevector, which is negligible, i. e. excitons with $k = k_e - k_h \approx 0$ emit optically.

1.1.4 Excitons in confined systems

In bulk semiconductors, the exciton wave number is not quantized due to the lack of quantum confinement. However, excitons in confined systems have a component of the wave vector quantized for each direction of confinement.

In heterostructures, when the exciton Bohr radius is comparable to the dimensions of the system, due to confinement effects, binding energy of exciton is modified. The total energy of exciton in heterostructures is given by:$E_{total} = E_{gap} + E_e + E_h + E_X$, where E_e and E_h are the electron and hole energies arising from the quantum confinement and E_X is the exciton binding energy given by the last term of equation 1.6. Due to the structural dependence of the confinement energies, as well as that of the Coulomb potential, the total exciton energy is structure dependent. The energy spectrum and wave-functions of quantum confined excitons can be strongly different from those of bulk excitons. From a simplistic point, it can be noted that for type-I systems the binding energy increases (w.r.t. that in bulk) if the exciton confinement strengthens. For type-II systems, however this can be inverted due to the spatial separation of electron and hole. In all cases, generally, the excitonic wavefunctions and energies are dependent on parameters (e.g. well width for QW, size and thickness for QDs) that control the extent of quantum confinement. Excitonic wavefunctions, and energies are calculated numerically for specific material systems and confinement potentials using variational methods in effective mass approximation. More detailed calculations involving self consistent addressing of Coulomb interaction, complexity of band structures and anisotropic effects require high computational capabilities.

1.2 Optical Processes in Semiconductors

Optical studies constitute the most important means of determining the band structures of semiconductors.

1.2.1 Absorption

A photon of energy $h\nu$ greater than the bandgap energy E_{gap} can be absorbed in a semiconductor, which results in the excitation of an electron from the valence band to the conduction band. The optical absorption depends on the thickness of the material. If $I(x)$ is the light intensity at position x within the material and δI is the change in the light intensity in the small elemental volume of thickness δx at x, then δI will depend on the number of photons arriving at this volume $I(x)$ and the thickness δx:

$$\delta I = -\alpha I \delta x \tag{1.7}$$

where α is the absorption coefficient of the semiconductor, whose magnitude depends on the photon energy. Integration of the above equation for illumination with constant wavelength light yields the Beer-Lambert law, which reveals that the transmitted intensity decreases exponentially with the thickness:

$$I(x) = I_0(x)\exp(-\alpha x) \tag{1.8}$$

The absorption coefficient depends on the photo absorption processes occurring in the semiconductor. In the case of band-to-band (interband) absorption, α increases rapidly with the photon energy $h\nu$ above E_g. The general trend of the α vs. $h\nu$ behavior follows the corresponding density of states.

Fundamental Absorption processes in semiconductors

Photon induced electronic transitions can occur between different bands and can be used to determine the energy band gap in semiconductors. Strength of absorption band edge depends on whether the valence band maximum and the conduction band minimum occur at the same point in the Brillouin zone. Semiconductors whose fundamental absorption edge involves a direct transition (same k value) are said to have a direct absorption edge. Otherwise the absorption edge is said to be indirect. Diamond, Si, Ge, AlAs, AlSb, SiC and GaP have indirect absorption edges, while GaAs, GaSb, InP, GaN, InAs, InSb, ZnSe, ZnTe and all the II-VI semiconductors have direct absorption edges. Optical transitions across an indirect bandgap are not allowed by the wavevector conservation condition and such transitions between two bands with different wavevectors are possible with the involvement of phonons (although they are orders of magnitude weaker than direct transitions). Hence they can be observed only when their energy is below that of all the direct transitions. Excitonic absorption contribute below the band gap via the bound states. Such contribution due to discrete states are generally observed as independent lines corresponding to the excitonic states below the band gap. The intensity of optical absorption close to the band edge in semiconductors is examined with band theory together with effective mass approximation for the excitons [33]. A good understanding can be developed from Refs. [34, 35].

1.2.2 Radiative recombination and Photoluminescence

The optical absorption process leads to the production of excitons which have relatively short lifetimes and tend to recombine with the emission of photons in a process called radiative recombination. Spontaneous emission of light due to radiative recombination processes is called *photoluminescence* (PL). Such an optical transition can be direct or indirect depending on whether or not it is phonon-assisted. During an optical transition the momentum needs to be conserved. In a direct band gap material, radiative recombination occurs without phonon participation, and the process is efficient. In an indirect gap material, the excited carriers thermalize to the lowest conduction band minimum, which typically is at $k \neq 0$. Thus, the radiative recombination process is accompanied by phonon emission to account for the momentum change of the carrier.

The photon absorption results in an excess electron concentration Δn, equal to the excess hole concentration Δp. The time dependence of the excess carrier concentration is governed by the rate equation

$$-\frac{d\Delta n}{dt} = -\frac{\Delta n}{\tau} \tag{1.9}$$

where τ is the carrier lifetime which represents the average time a carrier spends in the given band before recombination. The radiative processes are also accompanied by non-radiative recombination processes e.g due to thermalization, or through successive emission of phonons, producing heat, or through Auger processes wherein the recombination energy is transferred to a third carrier, which is elevated into the conduction band if it is an electron (or lowered into the valence band if it is a hole). The effective recombination time is given by

$$\frac{1}{\tau_{eff}} = \frac{1}{\tau_{rad}} + \frac{1}{\tau_{non-rad}} \tag{1.10}$$

and the radiative efficiency is given by

$$\eta = \frac{1}{1 + \tau_{rad}/\tau_{non-rad}} \tag{1.11}$$

The emission of light during the recombination of the excited electron-hole pair can be seen as the transition of a charged carrier from an initial state i to a final state f induced by the time dependent perturbation $\hat{H}$. The 'transition rate' $W_{f,i}$ is governed by the Fermi's Golden rule:

$$W_{f,i} = \frac{2\pi}{\hbar} \left| \langle \psi_f | \hat{H} | \psi_i \rangle \right|^2 \delta(E_f - E_i \pm \hbar\omega) \tag{1.12}$$

ψ_i and ψ_f are the initial and final state wave-functions. In the case of excitonic transitions, the overlap integral of electron and hole wavefunctions directly relate to the probability of transition and is commonly termed as the 'oscillator strength'. We note that any kind of change in the confinement of the quantum structures generally deals with the modulation of the oscillator strength whereas the frequency dependence of the transition rate is associated to the photon density of states.

1.3 Optical properties of type-II nanostructures

The spatial separation of electrons and holes at the interface in type-II heterostructures, results in tunability of their optical properties and quantum mechanical tunneling at abrupt interfaces allows for effective overlapping of their wavefunctions. The extent of overlap governs the exciton oscillator strengths and the optical transition matrix elements which determine the optical properties of the systems, including the decay dynamics.

The electric field created due to the spatial separation of the e and h results in band bending (Figure 1.5) at the interface of the heterojunction which is dependent on the excitation intensity (and thus carrier density) and this reflects from the PL emission from these structures. At higher carrier densities the band bending effect is enhanced which manifests itself as an increase in the PL emission energy, due to the increase in the energy separation of the e-h energy levels caused by the raising (lowering) of the e (h) energy levels, which is observed as a characteristic blue shift from the type-II structures [36–38] when the excitation intensity I_{exc} is increased. Typically, the characteristic blue shift in energy closely follows $I_{exc}^{1/3}$ behavior [36].

Example of such type-II behavior is shown in figure 1.6 for GaSb/GaAs nanostructures [37] and such a behavior from earlier studies on ZnTe/ZnSe stacked QDs is shown in Figure 1.7 [39].

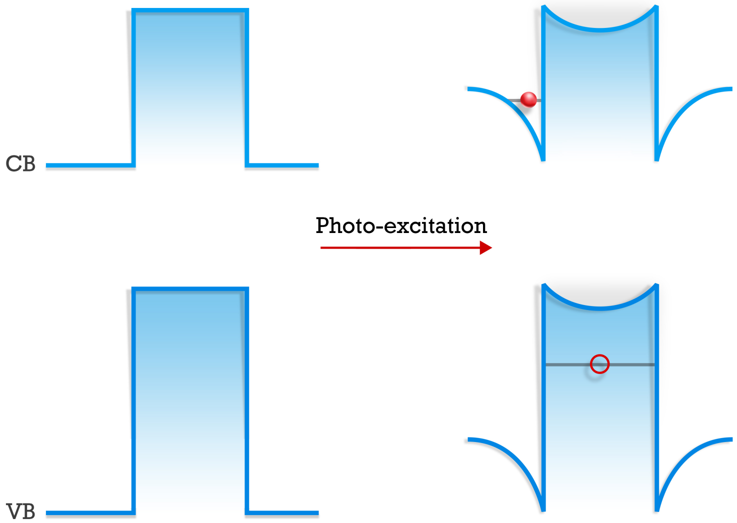

Figure 1.5: Band bending due to the electric dipole across the interface.

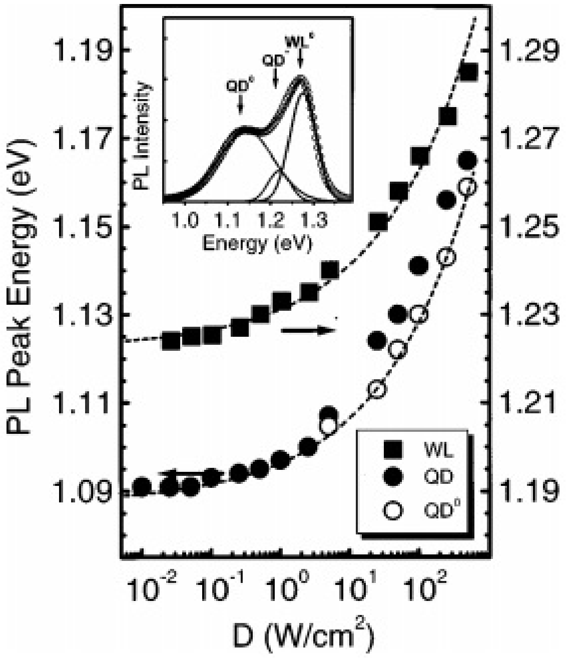

Figure 1.6: Dependence of PL emission energy on excitation density for type-II GaSb/GaAs QDs and Wetting layer (QW) fitted with 1/3rd power law [37].

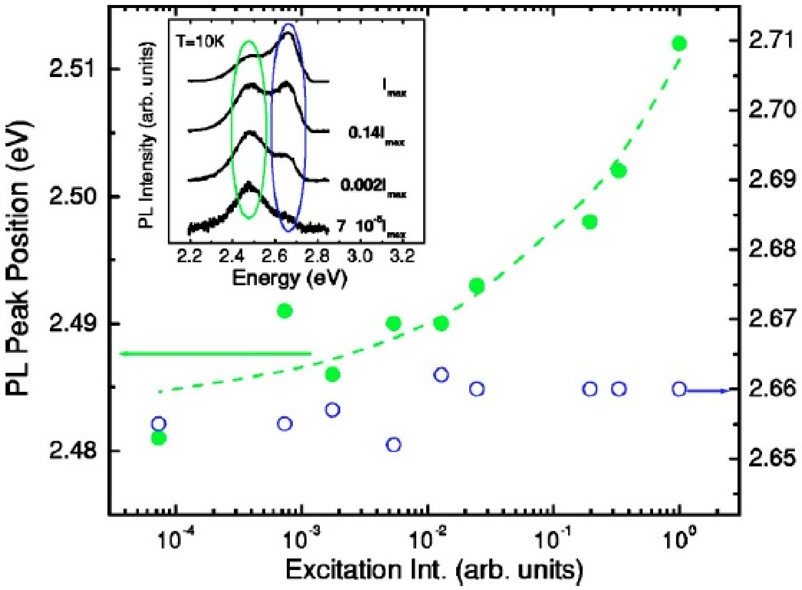

Figure 1.7: PL plot showing experimental observation of signature blue shift in type-II ZnTe/ZnSe QDs. The green closed circles show the behavior of the 'green' band PL which is dominated by QD emission [17].

In addition to possessing naturally longer carrier recombination lifetimes (in comparison to that in type-I structures) upto $\sim 1\ \mu s$ due to spatial separation of the photogenerated e and h, another optical signature of type-II structures is that the carrier recombination lifetimes are also expected to be carrier density dependent [36]. The larger the overlap of the carrier wavefunctions, the stronger is the oscillator strength and consequently at higher carrier densities (i.e. high excitation intensity), the decay time is reported to be shorter than at lower carrier densities. Figure 1.8 shows an example of such a typical behavior in ZnTe/ZnSe stacked QD system [40].

Thus both cw PL and TRPL are predicted and reported to be excitation intensity dependent which are considered hallmark for type-II heterostructures.

Later, in Chapters 5 and 6, we will show PL and TRPL experimental data on various samples and discuss in details the underlying physics and material properties revealed from such optical studies.

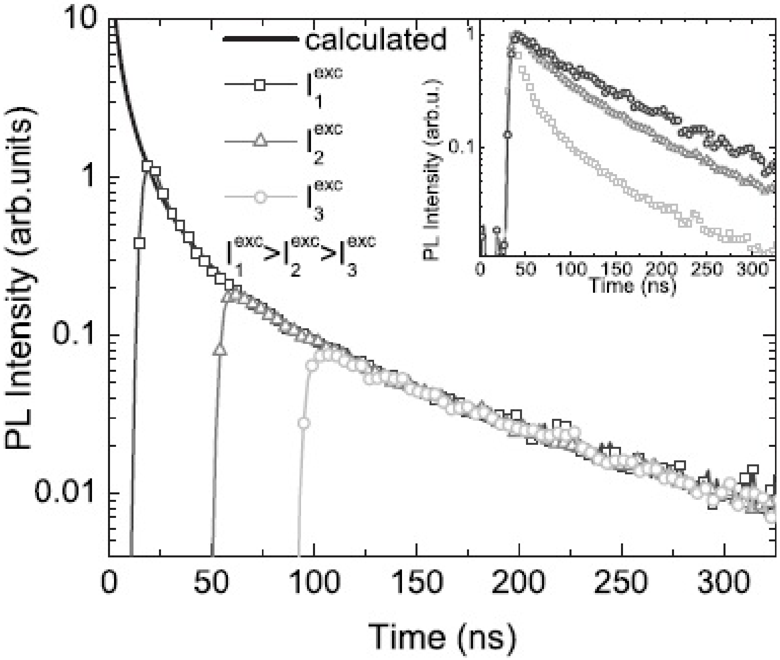

Figure 1.8: Time dependence of PL intensity for different excitation intensities, shown here for type-II ZnTe/ZnSe QDs [40] .

Chapter 2

Magneto- Optical Processes in Semiconductors

2.1 Effects of magnetic field on semiconductors

In solid state physics, study of materials in the presence of external magnetic field have been widely used in the investigation of the optical and transport properties of bulk and low dimensional semiconductors. The theory of the effect of a magnetic field on the optical absorption in semiconductors is developed on the basis of the effective-mass approximation [41]. Magnetic field quantize the energy states of the conduction bands and the valence bands in semiconductors. The quantization of the electronic states and the modification of the electronic wave function cause many new quantum phenomena.

2.1.1 Landau Energy levels

When a semiconductor is placed in a magnetic field B_z, the [conduction band] electron motion in the z- direction is not affected, but motion components in the transverse direction result in a periodic circular motion with angular frequency (called the cyclotron frequency):

$$w_c = \frac{qB_z}{m^* c} \tag{2.1}$$

where q is the charge, $m*$ is the effective mass of the carrier.

These orbits are quantized and the allowed transverse energies become:

$$E_x, y = \frac{q\hbar B_z}{m^* c}\left(n + \frac{1}{2}\right) \tag{2.2}$$

Landau quantization is a fundamentally quantum mechanical effect. $n = 0, 1, 2, ...$ is the Landau-level index corresponding to 1-D harmonic oscillator like states. In the longitudinal direction the energy of the carrier is independent of the magnetic field.

In actual semiconductors, the simplest approach to treat energy bands and Landau levels within the $\boldsymbol{k} \cdot \boldsymbol{p}$ approximation is the two band model with a single conduction and valence band and relatively small band gap, in that case the effect of other bands is neglected. The energy of the Landau levels express the non-parabolicity of the energy band at higher k values. Such two-band model works on narrow band gap material and non degenerate conduction and valence bands. In semiconductors with wide band gap and degenerate valence bands, complicated calculations, taking in account of the interband matrix element of the momentum operator and spin orbit interactions, are required to obtain the Landau energy level [42]. Details of such models is beyond the scopes of this thesis.

For lower dimensional systems, e.g. 2D confinement in quantum wells, the Landau levels are formed in each subband and corresponding to the complicated dispersion curves and interaction between the sub bands, the Landau level structure is also complicated for the conduction and valence bands[42]. In simplistic picture and the case of excitons, the essential physics remains the same (as in 3D case) except for one important qualitative difference: for a 2D system, the symmetry of hydrogenic exciton is unaffected by the application of magnetic field and the wave functions are expected to continuously transform from hydrogenic to harmonic-oscillator type (Landau level) type wavefunctions as the magnetic field is increased. For superlattice structures in magnetic fields Landau levels are formed in each miniband.

From the slope of the energy dependence on the magnetic field one can obtain the value of the electrons effective mass [43–46].

2.1.2 Diamagnetism and Zeeman Effects

In the context of photoexcited electron and holes, at low temperatures when they form bound excitonic states whose envelope functions are mathematically equivalent to hydrogen-atom wave functions (in the simplest one band effective mass approximation), the problem in the presence of magnetic field, low lying states are well described within perturbation theory. To order B^2 the change in energy is given by [47]:

$$\Delta E_n = \frac{e^2B^2}{8\mu_\perp}\langle n|\sum_i (x_i^2 + y_i^2)|n\rangle + \mu_B\vec{B}\cdot\langle n|\vec{L} + g\vec{S}|n\rangle + \sum_{m\neq n}\frac{|\langle n|\vec{L} + g\vec{S}|m\rangle|^2}{E_m - E_n} \quad (2.3)$$

The first term is the diamagnetic contribution to the energy, proportional to

$$\frac{q^2B^2}{8\mu_\perp}(x^2 + y^2)$$

and the square of wave-function in the plane perpendicular to the applied field. The diamagnetic shift is observed as characteristic quadratic shift to the energy of the system for not just hydrogenic ground state but also most bound states . Here $\mu_\perp$ is the reduced mass of the transverse effective masses of the charge carriers.

The second and the third terms denote the first and second order Zeeman effects due to orbital ($\vec{L}$) and spin ($\vec{S}$) angular momentum. In the simplistic picture spin Zeeman energy comes into play due to the interaction of the magnetic field with an orbiting electron. This causes a splitting of the energy level formerly occupied by the electron without the magnetic field and is given by $g\mu_B\vec{B}$, where g is the g-factor (related to gyromagnetic ratio) and μ_B is the Bohr-magneton. In semiconductor physics the effective g factor for various bulk and low dimensional materials are calculated [41] within $\boldsymbol{k}\cdot\boldsymbol{p}$ approximation and experimentally obtained via optical and magneto-optical studies; reflection, diamagnetic shift, magneto absorption and magneto-reflectance, photoluminescence, magneto-photoluminescence etc [43].

At high magnetic fields and for large orbits the splitting becomes quadratic in B. This nonlinear behavior occurs when B is greater than the internal field due to combined action of the spin and the orbit. For zero angular momentum (ground) states, the orbital paramegnetic Zeeman contribution is zero while the spin contribution is often ill-resolved for small values of g (e.g. in ensemble studies of QDs where spectra are inhomogenously broadened).

The above magnetic field effects are further modified for lower dimensional systems [42, 44, 45]. For example, the wave function extent of excitons confined in quantum potentials is smaller than that in a 3-D free space, so to observe a diamagnetic shift of the excitons higher magnetic fields are required [44].

Also in quantum dots, application of magnetic fields in the direction of growth can lead to interesting effect arising from the competition between the quantum potential and the magnetic field potential in the lateral direction [44]. Furthermore, when QDs are subjected to external magnetic fields, the B dependence is dependent on the strength of the field. For relatively weak fields, the quadratic (diamagnetic) dependence is observed which for strong fields, become linear (Landau)[45, 46]. Due to strong confinement in QDs, the size of the QDs can be approximated by the extent of wavefunction and one can extract both the size and effective mass from the two different field regimes as follows: the crossover region of the different field dependence is approximately expected where the exciton radius a_B, becomes of the order of the magnetic length $l = \sqrt{\hbar/eB}$.

Assuming for spherical QDs, in strong confinement regime, a_B is of the order of the dot size, the latter can be calculated. For instance, QD size is estimated to be 5 to 10 nm for our systems [17, 48]; hence the crossover should be observed at field values between $\sim$ 26 and 6.6 T (the limits are calculated for QD radius of 5 and 10nm, respectively). Thus we expect most of our experiments can fall into the weak or intermediate field regimes to exhibit the crossover. In strong field regime, linear B dependence can lead to estimation of the effective mass (from the slope) as discussed above [43–46].

2.2 The Aharonov-Bohm effect

In addition to the above mentioned effects, a fundamentally intriguing effect can be observed in systems of specific geometry; The Aharonov-Bohm (AB) effect [49] is purely quantum mechanical. To fully understand this effect and its non trivial nature it is essential to address few relevant concepts at first.

2.2.1 Adiabatic approximation and geometric phase

When a Hamiltonian changes very slowly from some initial form H^i to some final form H^f; the adiabatic theorem states that if the corresponding initial state wavefunction was the nth eigenstate of H^i, then under the Schrödinger equation, it will be carried into the nth eigenstate of H^f.

For a time-dependent hamiltonian, the eigenfunctions and eigenvalues are themselves time dependent:

$$H(t)\psi_n(t) = e_n(t)\psi_n(t) \tag{2.4}$$

The general solution to the time-dependent Schrödinger equation can be written as:

$$\Psi(t) = \sum_n c_n(t)\psi_n(t)e^{i\theta_n(t)} \tag{2.5}$$

where

$$\theta_n(t) \equiv -\frac{1}{\hbar}\int_0^t E_n(t')dt' \tag{2.6}$$

It turns out (and can be shown [50–52]) by considering time evolution of the coefficient $c_n(t)$ (equation 2.5) in adiabatic approximation gives:

$$c_m(t) = c_m(0)e^{\gamma_m(t)} \tag{2.7}$$

where

$$\gamma_m(t) = i\int_0^t \left\langle \psi_m(t')|\frac{\partial}{\partial t}\psi_m(t') \right\rangle dt' \tag{2.8}$$

and that $\Psi(t)$ in equation 2.5 remains the nth eigenstate of the evolving Hamilltonian only acquiring couple of phase factors:

$$\Psi_n(t) = e^{i\theta_n(t)}e^{i\gamma_n(t)}\psi_n(t) \tag{2.9}$$

The $\theta_n(t)$ (equation 2.6) is known as the ‘dynamic phase’ and $\gamma_n(t)$ (equation 2.8) is called the “**geometric phase**”.

The easiest way to understand why γ_n‘ is ‘geometric’ is the following; we can consider the gradual change in Hamiltonian is brought about by some slow changing parameter(s) $\mathbf{R}(t)$ where $\mathbf{R} \equiv (R_1, R_n, ...R_N)$, then equation 2.8 can be written as [50, 52]:

$$\gamma_n(t) = i \int_{\mathbf{R}_i}^{\mathbf{R}_f} \langle \psi_n | \nabla_R \psi_n \rangle \cdot d\mathbf{R} \tag{2.10}$$

where R_i and R_f are the initial and final values of $R(t)$ and ∇_R is the gradient w.r.t the R parameters. Now, If the Hamiltonian returns to its original form after a time T, the *net geometric phase change* is given by:

$$\gamma_n(T) = i \oint \langle \psi_n | \nabla_R \psi_n \rangle \cdot d\mathbf{R} \tag{2.11}$$

This expression for $\gamma_n(T)$ is called the **Berry's phase**[53]. We note that this line integral around a closed loop is in the parameter space and the Berry's phase depends on the path taken and not on how fast that path is traversed (provided it is slow enough to hold the adiabatic approximation).

2.2.2 Geometric phase and the Aharonov-Bohm effect

The AB effect describes that the wavefunction of a charged particle moving in a closed trajectory enclosing a magnetic flux acquires an extra phase, even though the particle itself remains in magnetic field free regions, due to its interaction with the vector potential of the magnetic field.

In the light of realization from the previous section this can be explained as the following; while slowly rotating along its trajectory, the charged particle encounters a slowly changing path dependent parameter (i.e. the position of the charged particle which determines the vector potential). This adiabatically affects the Hamiltonian acting on the charged particle. Hence, as shown above, the wavefunction of the charged particle accumulates the **'geometric phase'**.

Now we turn to one of the most standard ways to describe the AB effect which historically proved the fact that the electromagnetic vector potential is not a mere mathematical jargon but has non-trivial physical significance.

2.2.3 Wavefunction in vector potential

For a charged particle in electromagnetic field, the time dependent Schrödinger equation in terms of electromagnetic potentials is:

$$\left[\frac{1}{2m}\left(\frac{\hbar}{i}\nabla - q\mathbf{A}\right)^2 + V + q\phi\right]\Psi = i\hbar\frac{\partial\Psi}{\partial t} \tag{2.12}$$

To describe wavefunction of the charged particle, equation 2.12 needs to be solved, which can be simplified by using [51]:

$$\Psi(\vec{r},t) = e^{ig(\vec{r},t)}\Psi'(\vec{r},t), \tag{2.13}$$

where[1].

$$g(\mathbf{r}) \equiv \frac{q}{\hbar}\int_{\mathcal{O}}^{\mathbf{r}} \mathbf{A}(\mathbf{r}')\cdot d\mathbf{r}' \tag{2.14}$$

Initial point of integration $\mathcal{O}$ can be chosen arbitrarily, which is consequence of gauge freedom for electomagnetic potentials.

2.2.4 Magnetic Aharonov-Bohm effect

We consider an experiment (proposed by Aharonov and Bohm); where a beam of electrons is split into two, and passed by either side of a long solenoid (Figure 2.1, before being recombined. We note the beams pass though magnetic field free regions (outside the solenoid), however the vector potential [2],

$$\mathbf{A} = \frac{\Phi}{2\pi r}\hat{\phi} \tag{2.15}$$

is *not zero*, Φ being the magnetic flux enclosed by the electron trajectory. In classical electrodynamics, one would expect no interaction between electron beams and magnetic field, but due to interaction with the vector potential, wavefunctions of the two beams will accumulate **different phase factors** (as shown in equation 2.13) which can now be easily calculated by using 2.14:

$$g = \frac{q}{\hbar}\int \mathbf{A}\cdot d\mathbf{r} = \frac{q\Phi}{2\pi\hbar}\int\left(\frac{1}{r}\hat{\phi}\right).(r\hat{\phi}d\phi) = \pm\frac{q\Phi}{2\hbar} \tag{2.16}$$

---

[1] It is crucial that potential $\mathbf{A}$ is irottational (i.e. magnetic field $\mathbf{B}$ is zero), otherwise $g(\mathbf{r})$ is dependent on path of integration in equation 2.14, and hence would not define a function of $\mathbf{r}$

[2] Using the convenient gauge condition $\nabla\cdot\mathbf{A} = 0$

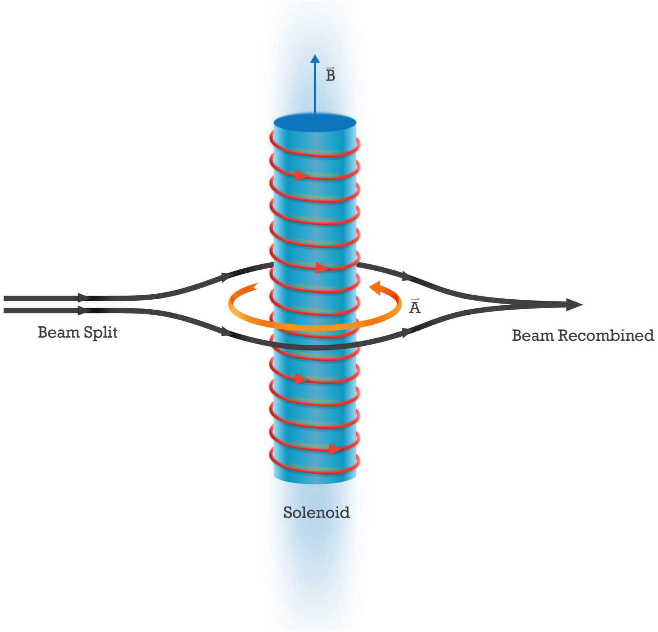

Figure 2.1: An experiment to demonstrate the AB effect; electron beam splits, with each beam passing on from either side of the solenoid. The beams never encounter the magnetic field while the vector potential influence the phase of their wavefunctions.

The plus (minus) sign applies to the beam traveling in the same (opposite) direction as **A** (or current in the solenoid). The **phase difference**:

$$\delta = \frac{q\Phi}{\hbar} \tag{2.17}$$

This phase difference leads to interference which can be measured experimentally [54].

We note that this phase difference δ (equation 2.17) can also be obtained via the geometrical Berry's phase calculation [50, 52] applying equation 2.11 which neatly confirms that AB-effect is a particular instance of the geometric Berry's phase.

It can be further noted [55, 56] that for a charged particle orbiting around a solenoid, the kinetic angular momentum $\mathbf{K} = \mathbf{r} \times m_q \mathbf{v}$ can change with increasing magnetic flux. This can be easily seen from the Hamiltonian describing such a cylindrically symmetric system where, for simplicity, we consider a charge on a circular orbit with fixed radius around the axis of symmetry of the solenoid

$$H = \frac{1}{2mr^2}\left[L_z + \frac{q\phi}{2\pi c}\right]^2$$

The Hamiltonian corresponds to the kinetic energy which is not a conserved quantity for time dependent flux. On the contrary the canonical angular momentum L_z commutes with the Hamiltonian even if the flux is time-dependent, L_z being the generator of the rotations around the z-axis. The canonical angular momentum is indeed the total angular momentum of the system, that is, the kinetic angular momentum K_q plus the electromagnetic angular momentum $\boldsymbol{L} = \boldsymbol{K} + \boldsymbol{M}$. In varying the flux of the solenoid we effectively change the kinetic angular momentum of the charge as well as the electromagnetic angular momentum while the total angular momentum is conserved.[3] The spectrum of the Hamiltonian is determined by the kinetic angular momentum and the AB effect is just a consequence of the quantization of the canonical angular momentum that does not depend upon the flux.

2.3 Early experiments verifying AB effect

Most of early experiments demonstrating AB effect were done in the field of magneto-transport in metal and superconducting rings [57]. Oscillation is observed with period of universal magnetic flux quantum $\Phi_0 = h/e$ in magneto resistance of the ring depending on magnetic flux enclosed governed by Landauer's formula [58–61].

The first demonstration of AB effect in semiconductor nanorings was the work of Ref. [61]. Since then AB effect in magneto transport of semiconductors gathered significant interest. With the progress of growth and fabrication techniques, research involving AB effect in semiconductors is explored in complicated systems; e.g GaAs/AlGaAs heterostructures [62], AlGaAs/GaAs system containing 2D- electron gas [63], GaAs hole system with strong spin orbit coupling [64], 2D-electron gas in InP/InGaP [65]. A good idea of quantum rings and treatment of AB effect persistent currents can be obtained from Ref. [66] and references therein.

In the following section we concentrate on the AB phase manifestation in semicon-

---

[3] This can also be easily seen classically where the conserved total angular momentum is given by

$$J_z = \left[r \times \left(mv + \frac{q}{c} A \right) \right]_z .$$

ductor nano-scale systems via the optical emission for systems with ring like geometry; the **excitonic AB-effect**.

2.4 Excitonic Aharonov Bohm Effect

The AB type-of topological phase shift for a dipole in a magnetic field is found to be equivalent to that of a charged particle in the AB settings (in the absence of magnetic field with zero Lorentz force) [67, 68] The manifestation of AB phase in the optical emission of excitons in quantum rings or type-II QDs with a ring-like topology has been theoretically predicted [69–72] and has commonly been addressed as *excitonic AB effect* or *optical AB effect.*

The generic quantum mechanical Hamiltonian in terms of electromagnetic potential is:

$$H = \frac{(\mathbf{p} - \mathbf{qA})^2}{2m} + V \tag{2.18}$$

where

$$(\mathbf{p} - \mathbf{qA})^2 = -\hbar^2 \left(\nabla^2 - \frac{iq\nabla \cdot \mathbf{A}}{\hbar} - \frac{i2q\mathbf{A} \cdot \nabla}{\hbar} - \frac{q^2}{\hbar^2}|\mathbf{A}|^2 \right) = -\hbar^2 \left(\nabla^2 - \frac{i2q\mathbf{A} \cdot \nabla}{\hbar} - \frac{q^2}{\hbar^2}|\mathbf{A}|^2 \right)$$

where in the last step we applied the gauge condition $\nabla \cdot \mathbf{A}$.

Considering the charged particle is adiabatically moving in a closed orbit of radius r, enclosing a constant magnetic field $\mathbf{B}$ with axially symmetric situation, in polar co-ordinates the vector potential,

$$\mathbf{A} = \frac{\Phi}{2\pi r}\hat{\phi}$$

with $\Phi = B\pi r^2$.

Using above and considering the case of an exciton, a model of two concentric one dimensional rings having different e and h radii R_e and R_h with angular co-ordinates θ_e and θ_h , respectively, enclosing a magnetic flux perpendicular to the plane of their motion,(Figure 2.2), the general Hamiltonian (equation 2.18) is of the form:

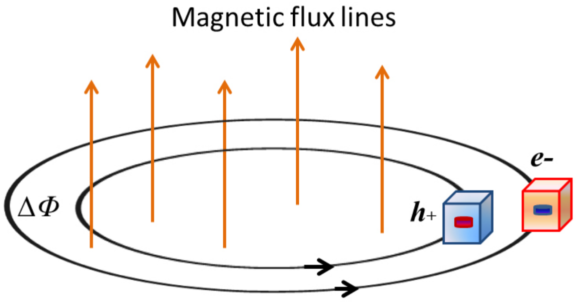

Figure 2.2: Schematic of polarized exciton(e and h are placed in separate boxes moving in different trajectories) enclosing magnetic flux. After a full revolution, the e and h accumulate different phases. The AB effect originates from the magnetic flux through the area between the two trajectories ($\Delta\Phi$).

$$\begin{aligned} H = &-\frac{\hbar^2}{2m_e R_e^2}\partial^2_{\theta_e} - i\hbar\frac{|e|B}{m_e c}\partial_{\theta_e} - \frac{\hbar^2}{2m_h R_h^2}\partial^2_{\theta_h} + i\hbar\frac{|e|B}{m_h c}\partial_{\theta_h} \\ &+\frac{1}{8}\frac{e^2B^2}{c^2}\left(\frac{R_e^2}{m_e}+\frac{R_h^2}{m_h}\right) + U_c(|\theta_e-\theta_h|) \end{aligned} \tag{2.19}$$

where $U_c(|\theta_e - \theta_h|)$ is the Coulomb interaction potential. In this settings we consider that the charged particle are moving adiabatically.

We can introduce convenient variables (as suggested in Ref.[71]):

$$\begin{aligned} \Delta &\equiv \theta_e - \theta_h \\ \theta_0 &= \frac{m_e {R_e}^2\theta_e + m_h {R_h}^2\theta_h}{m_e {R_e}^2 + m_h {R_h}^2} \\ R_0 &= \frac{R_e + R_h}{2} \\ M &= \frac{m_e {R_e}^2 + m_h {R_h}^2}{R_0^2} \end{aligned} \tag{2.20}$$

consequently we have,

$$\begin{aligned} \partial_{\theta_e} &= \partial_\Delta + \frac{m_e {R_e}^2}{MR_0^2}\partial_{\theta_0} \\ \partial_{\theta_h} &= -\partial_\Delta + \frac{m_h {R_h}^2}{MR_0^2}\partial_{\theta_0} \end{aligned} \tag{2.21}$$

$$\begin{aligned}-\frac{i\hbar|e|B}{C}\left[\frac{1}{m_e}\partial_{\theta_e}-\frac{1}{m_h}\partial_{\theta_h}\right] &= -\frac{i\hbar|e|B}{C}\left[\left(\frac{1}{m_e}+\frac{1}{m_h}\right)\partial_{\Delta}+\frac{R_e^2-R_h^2}{MR_0^2}\partial_{\theta_0}\right]\\ &= -\frac{i\hbar|e|B}{C}\frac{m_e+m_h}{m_em_h}\partial_{\Delta}- -\frac{i\hbar|e|}{\pi C}\frac{\Delta\phi}{MR_0^2}\partial_{\theta_0} \qquad (2.22)\end{aligned}$$

It follows that the Hamiltonian (equation 2.19) can be written as follows:

$$H=\frac{\hbar^2}{2MR_0^2}\left[-i\partial_{\theta_0}+\frac{\Delta\Phi}{\Phi_0}\right]^2+\left[-\frac{\hbar^2}{2}\frac{MR_0^2}{m_eR_e^2m_hR_h^2}\partial_{\Delta}^2\right.$$
$$\left.-\frac{i\hbar|e|B}{C}\frac{1}{\mu}\partial_{\Delta}+\mu_c(|\Delta|)+\frac{1}{8}\frac{e^2}{\pi C^2}\left(\frac{\Phi_e}{m_e}+\frac{\Phi_h}{m_h}\right)-\frac{1}{2MR_0^2}\frac{|e^2|}{\pi^2C^2}\Delta\Phi^2\right] \qquad (2.23)$$

with $1/\mu$, the reduced mass $\frac{m_e+m_h}{m_em_h}$. We can then decompose the Hamiltonian in $H = H_{\theta_0} + H_{\Delta}$ where H_{θ_0} is the angular part and H_{Δ} is the internal part. A separation of variables can be done for the wave function:

$$\psi(\theta_0,\Delta)=\psi_{\theta_0}(\theta_0)\psi_{\Delta}(\Delta)$$

It is crucial to note that

$$-i\partial_{\theta_e}-i\partial_{\theta_h}=-i\partial_{\theta_0}$$

defines the total angular momentum operator $\hat{L}_z$;

$$\hat{L}_z=\hat{L}_z^e+\hat{L}_z^h \qquad \text{such that} \quad \hat{L}_z\psi_{\theta_0}=L\psi_{\theta_0}$$

where L is the total angular momentum that clearly remains conserved because

$$\left[\hat{H}_{\theta_0},\hat{L}_z\right]=0 \quad \text{as well as} \quad \left[\hat{H},\hat{L}_z\right]=0$$

Two different limits of weakly and strongly bound excitons[71], (and while neglecting the internal Hamiltonian) has been discussed in appendix A following Ref. [71].

2.4.1 Disk-like type-II QDs

A more relevant special case for our particular system of disk like type-II QDs, wherein the hole is strongly confined within QD and the electron moves around it in an orbit of radius R_e (Figure 2.3), the Hamiltonian in 2.19 reduces to the form:

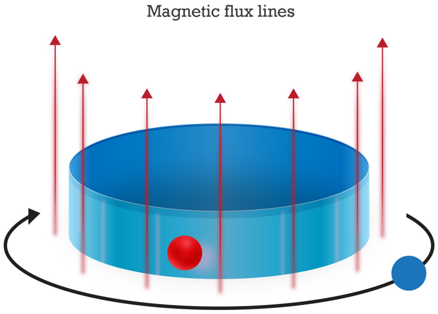

Figure 2.3: Schematic of a hole strongly confined within QD, while electron orbits around it in the presence of magnetic flux perpendicular to tha plane of motion; relevant to type-II QD systems with cylindrical symmetry, this is a suitable geometry to observe excitonic AB effect.

$$H = -\frac{\hbar^2}{2m_e R_e^2}\partial^2_{\theta_e} - i\hbar\frac{|e|}{2m_e R_e^2}\left(\frac{\Phi_e}{2\pi R_e}\right)\partial_{\theta_e} + \frac{|e|^2}{2m_e R_e^2}\left(\frac{\Phi_e}{2\pi R_e}\right)^2 + U_c(|\theta_e - \theta_h|) \tag{2.24}$$

with

$$U_c(|\theta_e - \theta_h|) = -\frac{|e|^2}{4\pi\epsilon R_e}$$

constant. The energy eigen value is given by:

$$E_L = \frac{\hbar^2}{2MR_e^2}\left(L + \frac{\Phi_e}{\Phi_0}\right)^2 - \frac{|e|^2}{4\pi\epsilon R_e} \tag{2.25}$$

In this case of strong hole confinement, as the magnetic flux increases, the ground state changes successively from $L = l_e = 0$ to non zero value ($L = l_e = -1$) which leads to a decrease in PL emission intensity due to transition of angular momentum state from optically 'bright' ($L = l_e + l_h = 0$) to optically forbidden 'dark' ($L \neq 0$) state. A 'peak' in magneto-PL of disk-like type-II QDs can appear in real experiments where the whole system is in the magnetic field, and the electron wavefunction is 'squeezed' closer to the QD boundary, leading to an increase in the electron-hole overlap, and thus increased PL intensity, which abruptly decreases when the electron undergoes angular momentum transition to the 'dark state'. The 'dark' excitons are expected to possess significantly longer recombination lifetime due to forbidden optical transition.

The 1^{st} transition of the electron orbital number to the non-zero value occurs at the field B_{AB} for which

$$\frac{\hbar^2}{2m_eR_e^2}\left(\frac{\Phi_1}{\Phi_0}\right)^2 = \frac{\hbar^2}{2m_eR_e^2}\left(-1+\frac{\Phi_1}{\Phi_0}\right)^2 \tag{2.26}$$

where

$$\Phi_1 = \pi R_e^2 B_{AB} = \frac{\Phi_0}{2} \tag{2.27}$$

We note, our results can also be achieved following the description of Govorov et. al. [71] in strongly bound exciton, by limiting the hole orbit radius to zero. We analyze in more details (Appendix A) the internal part of the Hamiltonian for exciton and also underline the similarity and differences in the settings with presence and absence of magnetic field.

The manifestation of AB effect via oscillation in optical PL emission as seen due to transition in angular momentum states has been widely researched theoretically(see for example references [70, 71, 73–76] and references therein) as well as interpreted experimentally [17, 77–83]

A different setting of the same problem has been discussed by Römer *et. al* [72], for ‘neutral’ excitons (for details see appendix A).

In later sections we will see that we found evidence of presence of built-in electric fields as indicated by the enhancement and narrowing of AB peaks, which is a conclusion extracted from both the pictures.

2.4.2 Defects and stacked QDs

Real QDs have defects and are usually elongated. For non-cylindrical dots the selection rules are relaxed and dipole emission is allowed for arbitrary L. Scattering impurities may enhance the PL intensity on otherwise “dark magnetic field windows. The states made of even orbital momenta become optically active due to the linear combination of states with different L [84].

The presence of impurity states are predicted to add additional features such as modulations in the PL intensity at certain magnetic field values and additional peaks and valleys at higher temperatures (the latter due to the contribution from higher energy excited states) for type-II QDs and quantum rings (QRs). Such an observation is reported for stacked typeII QDs in ref. [17]. Also for stacked QDs, which is similar to multiple quantum well systems, the interface defects are important and play the role of carrier trapping centers. This may result in a reduction of radiative recombination and can cause a decrease in the overall PL intensity [17, 81, 82].

Chapter 3

Experimental Setup

3.1 Molecular Beam Epitaxy

Multilayered Zn-Se-Te structures with sub-monolayer insertion of ZnTe were grown by a combination of Molecular Beam Epitaxy (MBE) and Migration Enhanced Epitaxy (MEE)[1] in a Riber 2300 system (samples are grown under the leadership of Prof. Maria Tamargo at the City College of CUNY). A schematic of the MBE chamber is shown in Figure 3.1. The system consists of two different ultra high vacuum chambers for II-VI and III-V materials wherein the samples can be transferred via the transfer module. Different effusion cells with controllable source temperatures are used in specific shutter sequences to achieve the desired growth. The growth is continuously monitored by Reflection high-energy electron diffraction (RHEED) oscillations. More details on growth and information about specific samples are described in following chapters.

Various samples were grown using specific shutter sequences and different growth parameters and detailed Optical and magneto-optical studies were performed on them.

---

[1] Migration enhanced epitaxy is a variant of conventional MBE, and it occurs when the growing surface is alternatively exposed to group II and group VI elements or to group III and group V elements. For a review, see e.g., Y. Horikoshi, Semicond. Sci. Technol. **8**, 1032 (1993)

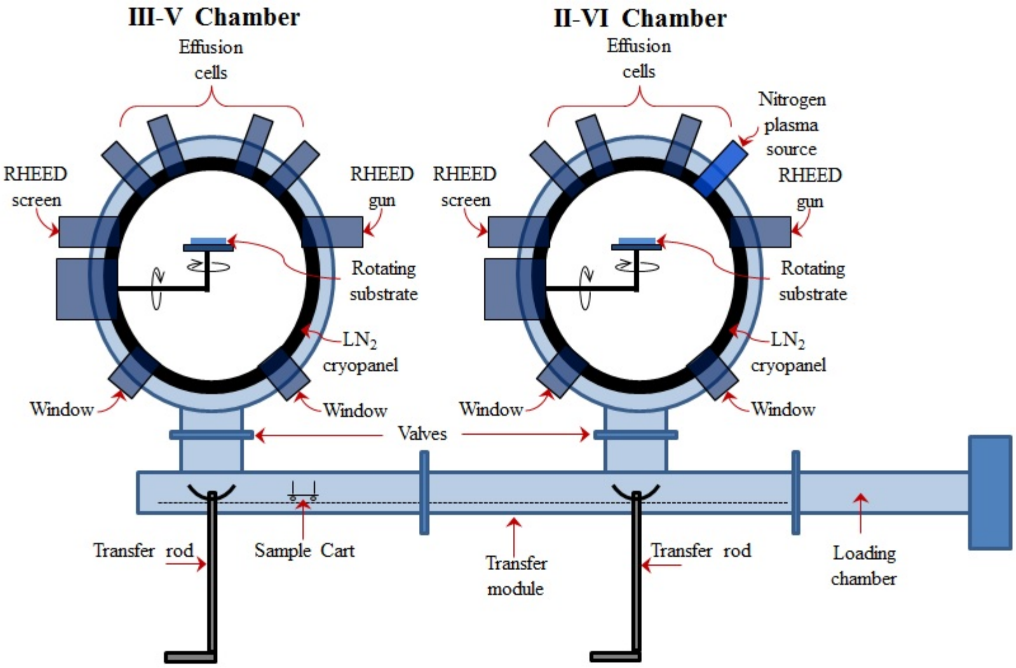

Figure 3.1: Schematic of MBE chamber used to grow the samples.

3.2 Photoluminescence

PL is a very useful non destructive characterization technique that can be used to investigate different kinds of radiative processes and extract fundamental information about material parameters of the sample. The PL spectra can deliver information about a variety of states; such as energy band extrema, free excitons, bound excitons associated with impurities and defects, and charged excitons. The method employs the measurement of emitted light as a function of wavelength (photon energy) when the sample is irradiated with photon beam of energy higher than the band gap of the material. Moreover, although the PL is produced by radiative processes, the thermally activated non-radiative recombinations affect the overall emission and thus allow to investigate them in indirect ways. To analyze PL spectra, the identification of the origin of the light emission is necessary.

3.2.1 PL experimental-set up

For PL measurements, the 351 nm emission line from an Ar laser was used for excitation. The excitation intensity was varied over 4 orders of magnitude using neutral density filters (NDF). The PL emission was detected by a TriVista SP2 500i Triple monochromator coupled to a thermo-electrically cooled photomultiplier tube (PMT) and a photon counting system. An ARS closed cycle refrigerating system was used for low temperature and temperature dependent measurements from 7 to 250 K for both cw and time resolved PL measurements. A schematic of this setup is shown in Figure 3.2

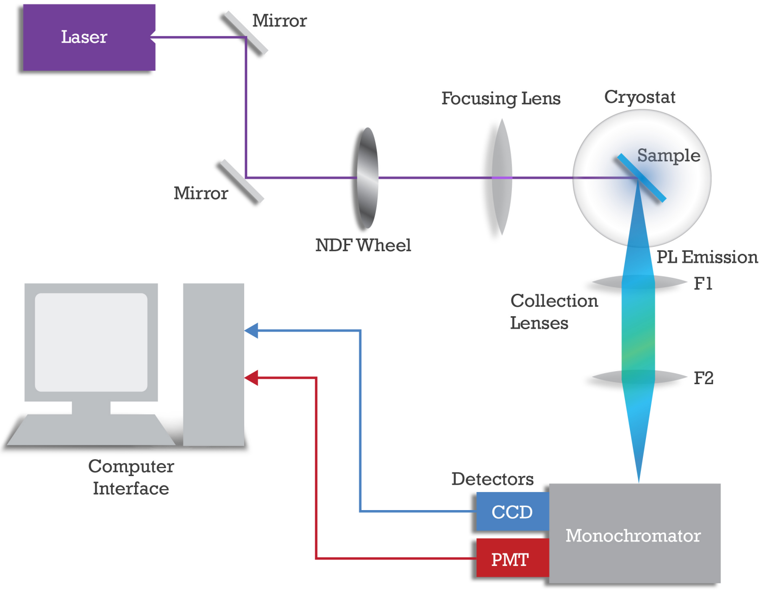

Figure 3.2: Schematic of low temperature and temperature dependent, high-resolution Photoluminescence set-up. The rotatable NDF wheel enables to change excitation intensity by upto 5 orders of magnitude. The PMT or CCD detectors for obtaining required resolutions in dfferent samples.

3.3 Time-resolved photoluminescence

Time-resolved photoluminescence (TRPL) is a powerful experimental tool to study carrier decay dynamics in materials after illumination with pulsed light source. This involves measuring of PL decay curves i.e. PL intensity as a function of time. Typically, a qualitative assessment about particular mechanisms can be made by examining raw decay data and proper fitting functions can be selected for extracting relevant parameters (e.g most directly to obtain the 'lifetime' of radiative processes). The PL lifetime is an average time for the carriers to remain in the excited state after photo-excitation and before emitting a photon.

3.3.1 TRPL experimental set up

Time-resolved PL studies were performed using the 337 nm line of a N_2 pulsed laser with 4 ns pulse width. The signal was recorded using a 500 MHz Tektronix TDS 654C oscilloscope. A schematic of this setup is shown in Figure 3.3.

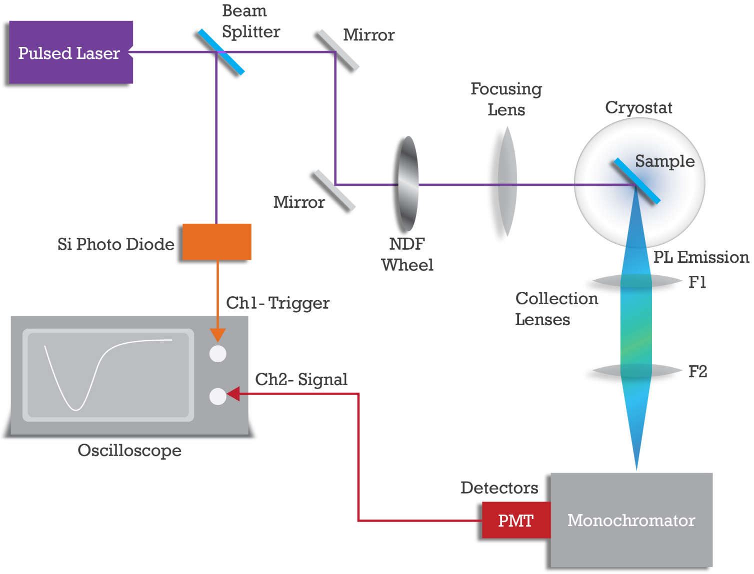

Figure 3.3: Schematic of low temperature and temperature dependent Time-resolved Photoluminescence set-up

The temporal information combined with spectral data (continuous wave- PL) can help determine the dynamics of carriers involved in the optical processes.

3.4 Secondary Ion Mass Spectroscopy

Secondary ion mass spectrometry (SIMS) is a technique that can determine elemental, isotopic, or molecular composition of a specimen, to great accuracy. The sample is subjected to a focused primary ion beam and the ejected secondary ions are collected and analyzed. The secondary ions are then accelerated, focused (by extraction lens), and analyzed by a mass spectrometer to determine the composition of the system. A schematic of SIMS measurement is shown in Figure 3.4

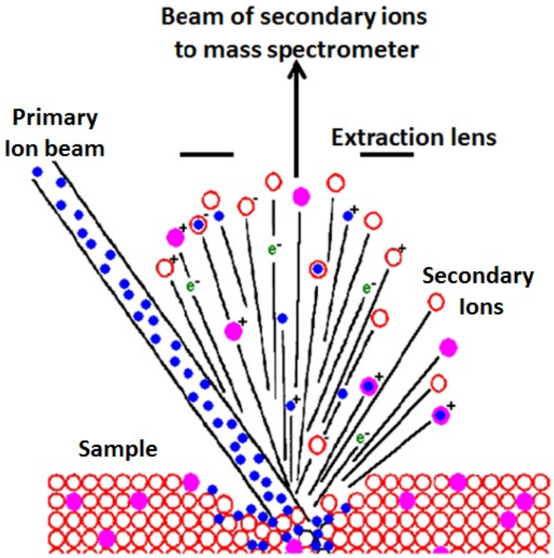

Figure 3.4: A basic schematic of SIMS measurement.

The bombarding primary ion beam produces monoatomic and polyatomic particles of sample material and resputtered primary ions, along with electrons and photons. The secondary particles carry negative, positive, and neutral charges and they have kinetic energies that range from zero to several hundred eV. Primary beam species useful in SIMS include Cs+, $O2+$, O , Ar+, and Ga+ at energies between 1 and 30 KeV. Primary ions are implanted and mix with sample atoms to depths of 1 to 10 nm.

SIMS measurements on our samples were done by EVANS Analytical Group at their lab in Sunnyvale, CA.

3.5 High resolution x-ray diffraction

A typical High resolution x-ray diffraction (HRXRD) setup consists of X-ray synchrotron radiation source, beam conditioners (collimated and monochromatic beam is obtained with the help of beam conditioners) on incident and diffracted beam side, a sample stage which is capable of movement in different directions (tilt and rotation for precise placement of sample) and detector. The technique is widely used for structural characterization of epitaxial layers to determine thickness and composition as well as to evaluate strain and relaxation within a given layer of a multilayer structure. Figure 3.5 shows a schematic of the basic principle of the technique.

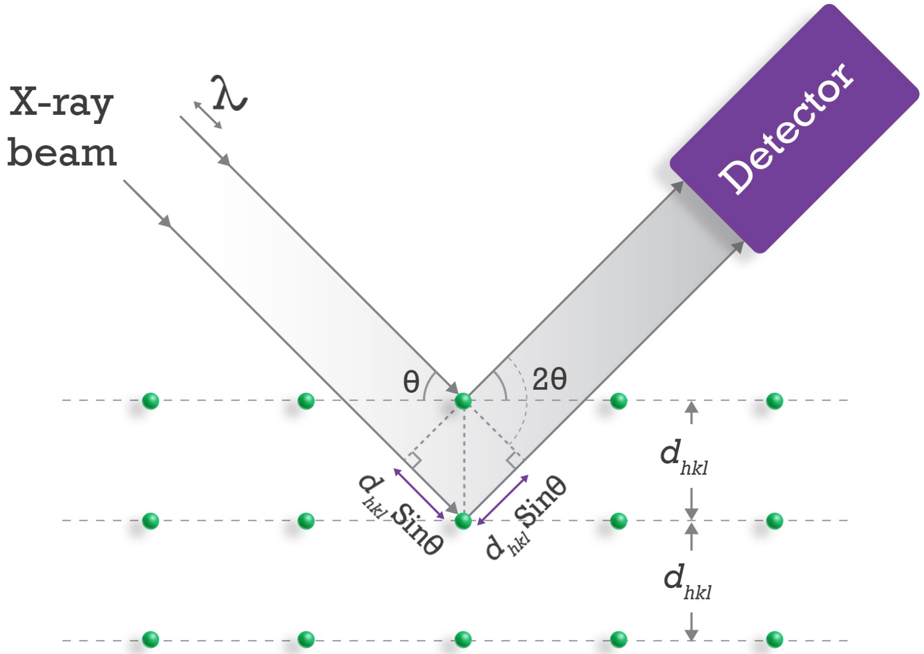

Figure 3.5: A basic schematic of HRXRD measurement.

This technique can be understood simply by reducing the Laue equation to Braggs law. Bragg's law gives the condition for coherent and incoherent scattering from the lattice sites in a crystal structure. Bragg diffraction occurs when an electromagnetic radiation with wavelength comparable to atomic spacing is incident upon a crystalline sample, are scattered by the underlying atoms and undergo constructive interference. The path difference between two waves undergoing constructive interference is given by $2d_{hkl}\sin\theta$, where θ is the scattering angle and h, k, and l, are the miller indices of the consecutive crystallographic planes (Figure 3.5). This path difference has to equal to the integer multiple of the wavelength to preserve the phase of incident and scattered waves. Bragg diffraction condition is given by $2d_{hkl}\sin\theta = n\lambda$ where, n is an integer, and λ is the wavelength of the electromagnetic radiation. HRXRD plot can thus be obtained by measuring the intensity of scattered waves as a function of scattering angle.

The HRXRD measurements were carried out at Beamline X20A at the National Synchrotron Light Source at the Brookhaven National Laboratory. All measurements were performed using monochromatic synchrotron radiation at 8 keV, with a double-crystal Ge (111) monochromator. To enhance the angular resolution, a Si (111) analyzer was placed in front of the detector.

3.6 Magneto-Photoluminescence

Magneto-cw PL was performed in the Faraday configuration (the field is parallel to the growth direction of the samples) up to either 9 T or 14 T. For cw PL measurements, 405 nm line from diode laser, or the 325 nm emission line from a HeCd laser, or 351 nm line of Ar laser, was used for excitation. The sample was placed inside the magnet on an optical probe with multiple optical fiber connections (specially designed for the magnets used). The PL emission was collected by optical fiber and detected by either a HR4000 Ocean Optics spectrometer (at Queens Collge of CUNY and at National High Magnetic Field Laboratory (NHMFL), Tallahassee, FL) or by a liquid- nitrogen (LN) cooled charge coupled device (CCD) camera coupled with a monochromator (at NHMFL, Tallahassee, FL). A simplified schematic of the experimental setup is shown in Figure 3.6.

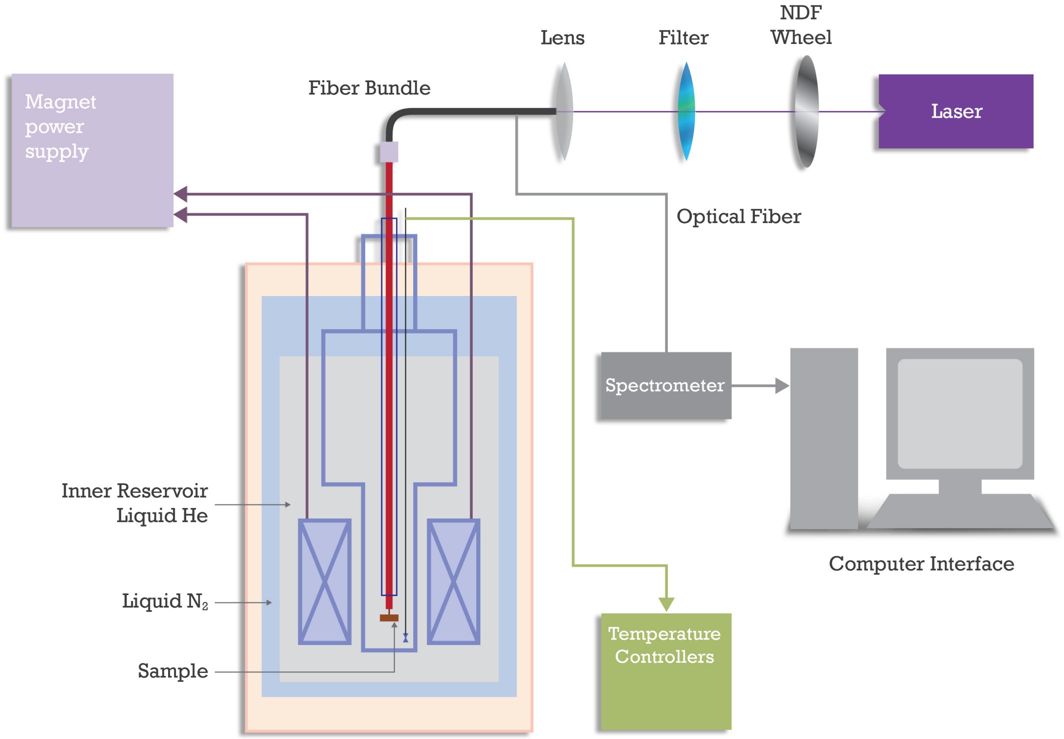

Figure 3.6: Schematic of Magneto-PL set-up

3.7 Magneto-TRPL

Magneto TRPL experiments were done to obtain information about lifetime of magneto-excitons, especially due the optical excitonic AB effect. Magneto-TRPL studies were performed using the 337 nm line of a N_2 pulsed laser with 4 ns pulse width. The sample was placed inside the magnet on an optical probe with multiple optical fibers (specially designed for the magnets used). A dichroic beam splitter was used to isolate the excitation and collection optical wavelengths. The signal was collected after focusing the PL on an optical fiber matched to the input of the monochromator, detected by thermo-electrically cooled low noise PMT and recorded using a 500 MHz Tektronix TDS 654C oscilloscope.

A simplified schematic of the experimental setup is shown in Figure 3.7.

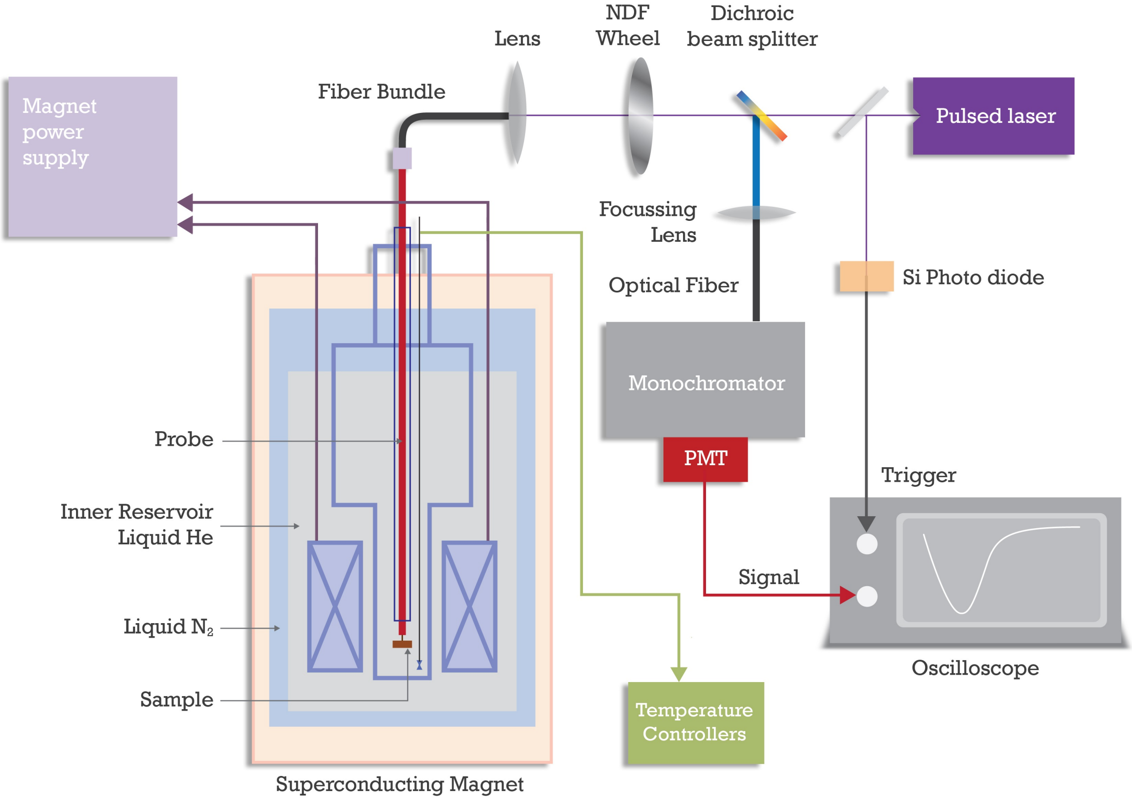

Figure 3.7: Schematic of Magneto-TRPL set-up

Chapter 4

Type-II ZnTe/ZnSe quantum dots-Optical Studies

4.1 Effects of varying MBE growth conditions

In this chapter we report optical studies on the effects of varying growth conditions on sets of samples.

4.1.1 Samples and Growth

Samples were grown on (001) GaAs substrates. Prior to the growth of the II-VI epilayers, a Zn irradiation of the GaAs surface was performed for 20 s at 200 °C. Then an undoped ZnSe buffer layer was grown at 300 °C under Se-rich conditions. After the buffer layer growth, the multilayers were grown. Ten monolayers (10 MLs) thick ZnSe spacer (barrier) were grown by opening the Zn and Se shutters together, after which the Se shutter was closed to produce a Zn-terminated surface. Then all shutters were closed to desorb excess Zn from the surface. The Te shutter was opened for 5 s to deposit Te onto the Zn- terminated surface. This was followed by closing of all shutters for - $t_{\text{all-off}}$ seconds followed by opening of the Zn shutter to produce another Zn terminated surface. This wait time ($t_{\text{all-off}}$) was chosen as one of the varied parameters. Four values, 0, 3, 6 and 9 s were tried, forming sample series II (see below) for this work. We note that Te (Zn) was deposited without Zn (Te), which enhances surface diffusion. Since a very small Te flux is used during the deposition, only a fraction of a Te monolayer (submonolayer) is formed, which leads to formation of type-II QDs. The lack of full ZnTe monolayers is also supported by monitoring the RHEED oscillations during the growth. This procedure was repeated three times, before the Se shutter was again opened to start the next growth sequence. The whole cycle was repeated for between 100 and 200 times. The overall thickness of the samples is ∼ 500 to 600 nm.

More details on growth procedure are described elsewhere (see, e.g., ref. [85]). Figure 4.1(a), (b) and (c) demonstrate the shutter sequence during the growth procedure, a schematic of sample structure and that of ZnTe submonolayer quantum dots, respectively.

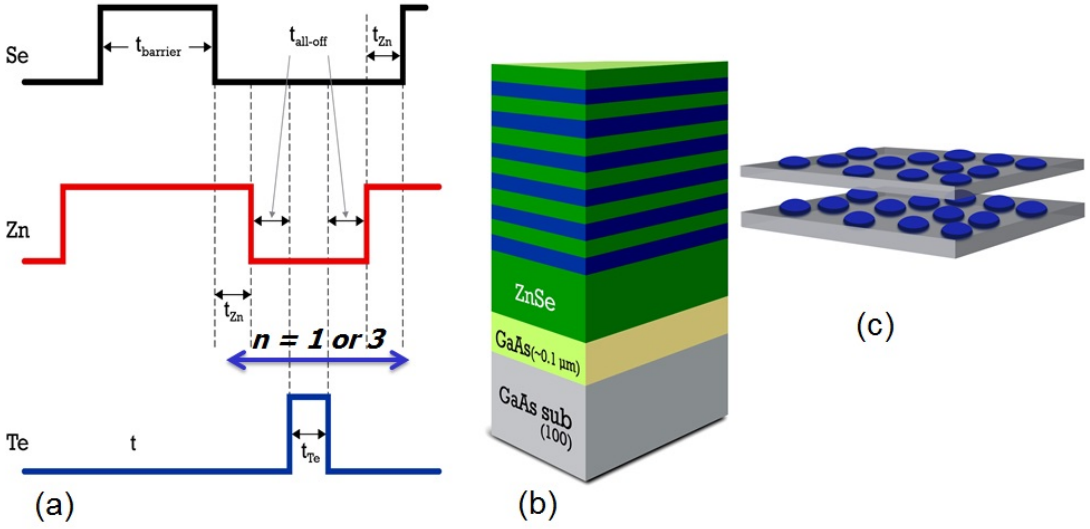

Figure 4.1: Schematics of a) shutter sequence for sample growth b)sample structure c) ZnTe submonolayer QDs layers.

Two different series of samples were grown which are summarized in Table I. For sample series I (samples D36, D38, D40) the Te effusion cell temperature ($T_{\text{Te source}}$) was varied during the growth, whereas, for series II (D28, D30, D32, D34), samples were grown by varying the wait time ($t_{\text{all-off}}$) after the Te shutter was opened while

Series I		
Sample	$T_{T_e source}$	PL peak energy (at 10 K)
D36	$215°C$	2.680 eV
D38	$225°C$	2.474 eV
D40	$245°C$	2.285 eV
Series II		
Sample	$t_{\text{all-off}}$	PL peak energy (at 10 K)
D28	0 s	2.430 eV
D30	3 s	2.411 eV
D32	6 s	2.414 eV
D34	9 s	2.460 eV

Table 4.1: Sample information with varied MBE growth parameters

following the shutter sequence.

4.1.2 Effect of varying Te effusion cell temperature

The PL spectra at 10 K for samples D36, D38 and D40, with increasing the Te effusion cell temperature ($T_{T_e source}$), are shown in Figure 4.2. The corresponding peaks are observed at ∼2.680, 2.474, and 2.285 eV.

We propose that the red shift of the peak position from sample D36 to D40 correlates with the higher $T_{T_e source}$, i.e. higher Te beam intensity [86], and leads to the formation of larger nano-islands[1]. This is supported by the facts that samples D36 and D38 show the presence of two broad PL peaks (and some other characteristic sharp features) when studied carefully; these latter features (∼ 2.70 and 2.73 eV) present at the higher energy side are characteristic of relatively low Te fraction in the [39, 85, 88]. A high energy band (blue) between 2.60 and 2.75 eV and a lower energy band (green) at ∼2.50 eV are clearly present. The blue band is generally accepted to be due to the emission from the excitons bound to isoelectronic Te_2 complexes. The

---

[1] We predict the larger Te beam intensity contributed primarily towards increasing the size of the QDs. The concentration of Te in these samples is estimated to be between 50 to 70% (see Y. Gong et al., J. Appl. Phys. **99**, 064913 (2006); Gong, et al., Phys. Rev. B **77**, 155314 (2008)). The red shift in peak position strengthens our prediction regarding the composition estimation, as in case of increase in Te concentration over 60%, the peak position is expected to show a blue shift following the band bowing effect as a function of Te composition [87].

green band is attributed to the emission from excitons bound to both isoelectronic $Te_{n\geq 2}$ clusters and confined to type-II QDs [39, 88]. Contribution from a peak near the tail of the green band, between 2.2 and 2.3 eV is also present in the PL spectra of samples D38 and D40, which is a result of larger, Te rich, ZnTe QDs [88]. The PL peak of sample D40 at ∼2.28 eV shows the absence of the higher energy peaks and is narrower. This peak is thus mainly due to larger QDs and with a more uniform size distribution than in samples D36 and D38.

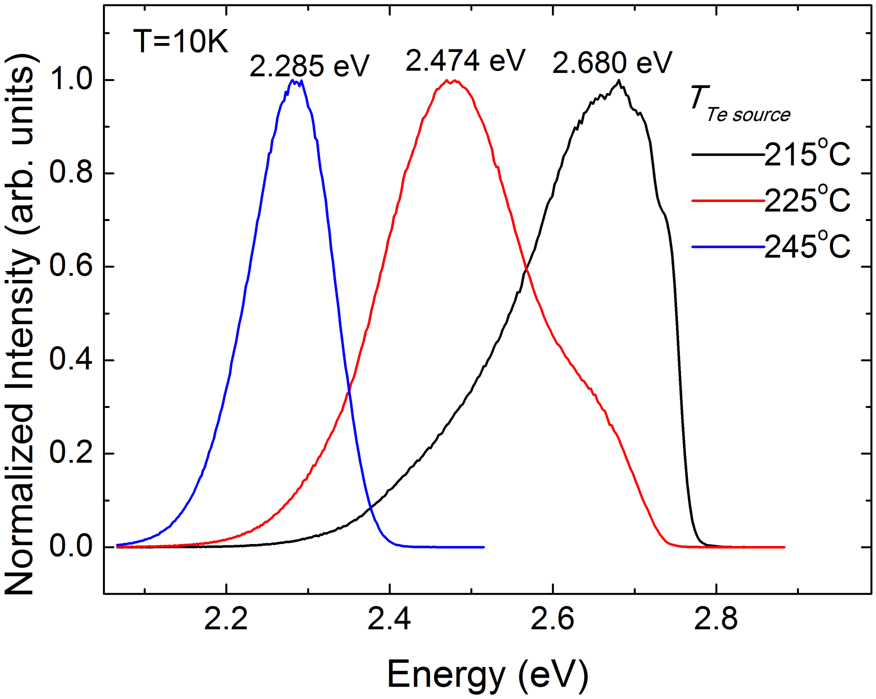

Figure 4.2: Low temperature PL of ZnTe/ ZnSe QDs as a function of $T_{T_e source}$ for sample series I.

The excitation intensity dependence of the emission energy at 20% height of the peak on the low energy side of samples D36, D38 and D40 are shown in Figure 4.3 The blue shift of the emission energy with increasing excitation intensity has been previously reported for various type-II quantum structures [36, 37, 89, 90]. For our material system, due to a large valence band offset (0.8-1.0 eV) [14, 91] the hole is strongly confined within the ZnTe-rich QD whereas the electron is located within the ZnSe-rich barriers.

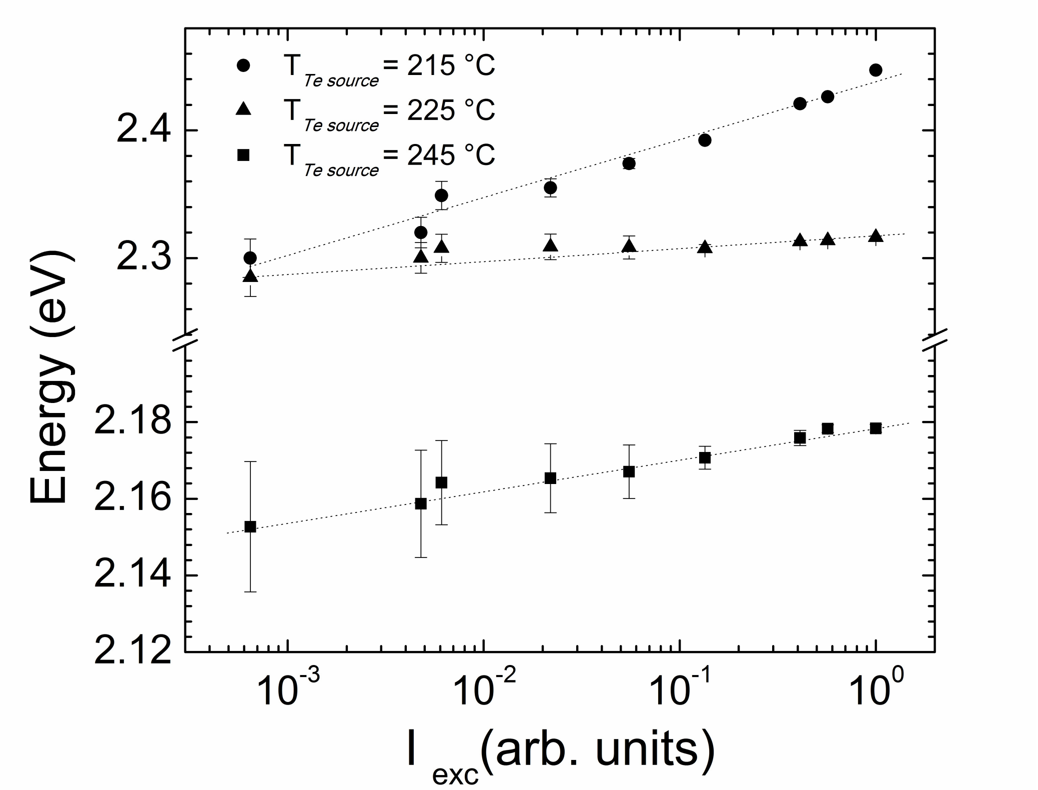

Figure 4.3: Excitation intensity deendence of emission energy at 20% height of the peak on the lower energy side for sample series I with varied $T_{T_esource}$. The dotted lines are for eye guidance

The Coulomb interaction creates an electric field across the interface which results in band bending. On increasing the excitation intensity, more electron and hole pairs are excited and the band bending effect is increased. The emission spectra thus, shift to higher energies with increasing excitation intensity. And this effect is at least partially attributed to type II quantum structures. We also note that the magnitude of the shift in emission energy with changing the excitation intensity over three orders of magnitude is the largest for sample D36 ($\sim$ 147 meV) followed by that in samples D38 ($\sim$ 31 meV) and D40 ($\sim$ 26 meV). We attribute this observation to be an indication towards the size of the QDs. Larger QDs have closely spaced energy levels and on changing the excitation intensity, the relative change in energy levels for the carriers is smaller for larger QDs, and thus the smaller QDs will show a larger shift as compared to that shown by larger QDs for the same amount of change in excitation intensity. This supports our conclusion that size of the QDs increased from sample D36 to D38 and further in sample D40 due to increasing $T_{T_e source}$.

SIMS measurements were performed on these samples to determine the Te concentrations and confirm our predictions. Figure 4.4 shows the SIMS profile for Te concentrations for samples in series I. Indicatively, the average Te concentration is highest in sample D40 followed by samples D38 and D36.

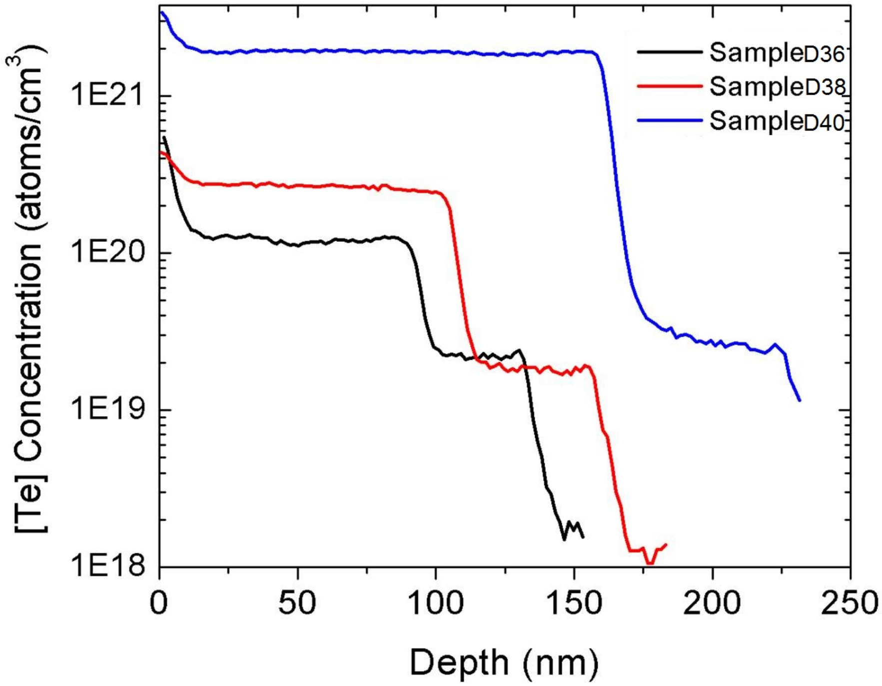

Figure 4.4: SIMS profiles of sample Series I indicating $T_{T_e source}$ is the key parameter in controlling the [Te] concentration in the samples.

The low temperature TRPL for samples D36 and D38 taken at the same energy of 2.38 eV and for samples D38 and D40 taken at 2.33 eV are shown in Figures 4.5 and 4.6, respectively. Sample D36 shows faster decay than sample D38 (Figure 4.5) which is indicative of smaller QDs in sample D36. This is explained by lifetime being dependent on the overlap of the carrier wavefunctions, which is larger for smaller QDs.

Such observation also supports our observation of a red shift of PL peak position of sample D38 w.r.t. sample D36. At the same time, Figure 4.6 indicates that sample

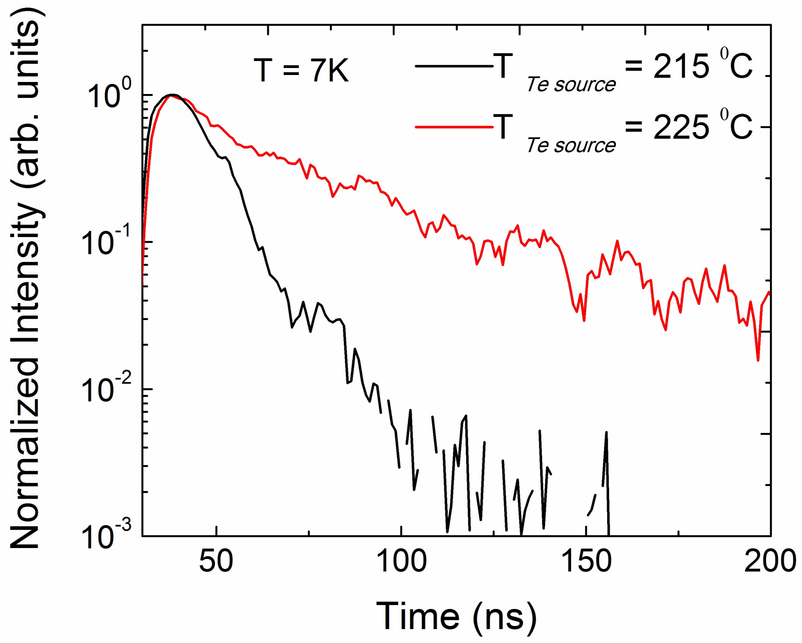

Figure 4.5: Time decay curves for samples D36 and D38 taken at 2.38 eV.

D40 exhibits faster recombination lifetime in comparison to sample D38. Although it is counter-intuitive and not well understood, we point out that such a behavior of PL lifetime at low energy ($<$ 2.35 eV) in Zn-Se-Te systems has been previously reported and is tentatively attributed to impurities or defect states formed on the QD surface, the origin of which may be related to the strain relaxation of larger QDs due to strain interaction of the coupled QD layers [88]. This is reported to increase dislocation and defect formation significantly in InAs QDs [92]. Such dislocations will significantly decrease the PL lifetime of the QDs due to an increased contribution from nonradiative processes. Previously this low energy emission was mixed with other processes in one sample, rather than dominate, as seen here, and we thus, plan further studies of this matter.

The 10 K PL for the sample series II with different wait time durations, i.e. time for which all the shutters are off ($t_{\text{all-off}}$) is shown in Figure 4.7

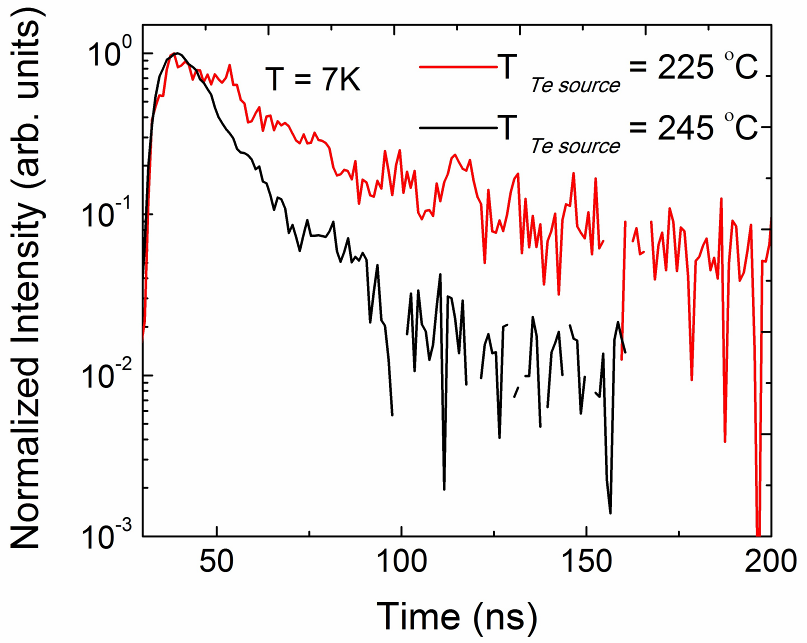

Figure 4.6: Time decay curves for samples D38 and D40 taken at 2.33 eV.

4.1.3 Effect of varying 'wait-time'

The PL peaks for samples D28, D30, D32 and D34 are observed at 2.430, 2.411, 2.414 and 2.460 eV, respectively. We discuss such an observation in terms of $t_{\text{all-off}}$ affecting a competition between surface diffusion of Te ad-atoms (which is responsible for the formation of the QDs) and their desorption [93].

We estimate that for tall-off between 0 and 3 sec, diffusion of Te ad-atoms leads to their aggregation into the nano-islands, thus allowing formation of larger QDs (shown by the red shift in the peak position of samples D28 and D30 $\sim$ 19 meV). Increasing $t_{\text{all-off}}$ from 3 to 6 sec, results in the PL blue shift ($\sim$3 meV, for samples D30 and D32), indicating onset of desorption of Te ad-atoms. Further increasing $t_{\text{all-off}}$ to 9 sec, showed a significant blue shift ($\sim$ 46 meV) of the PL for samples D32 to D34, which we explain as due to increased desorption of Te ad-atoms and thus a decrease or loss in QD size. This sample series also exhibits the blue shift of emission energy taken at 20% height of the peak on the low energy side with increasing excitation

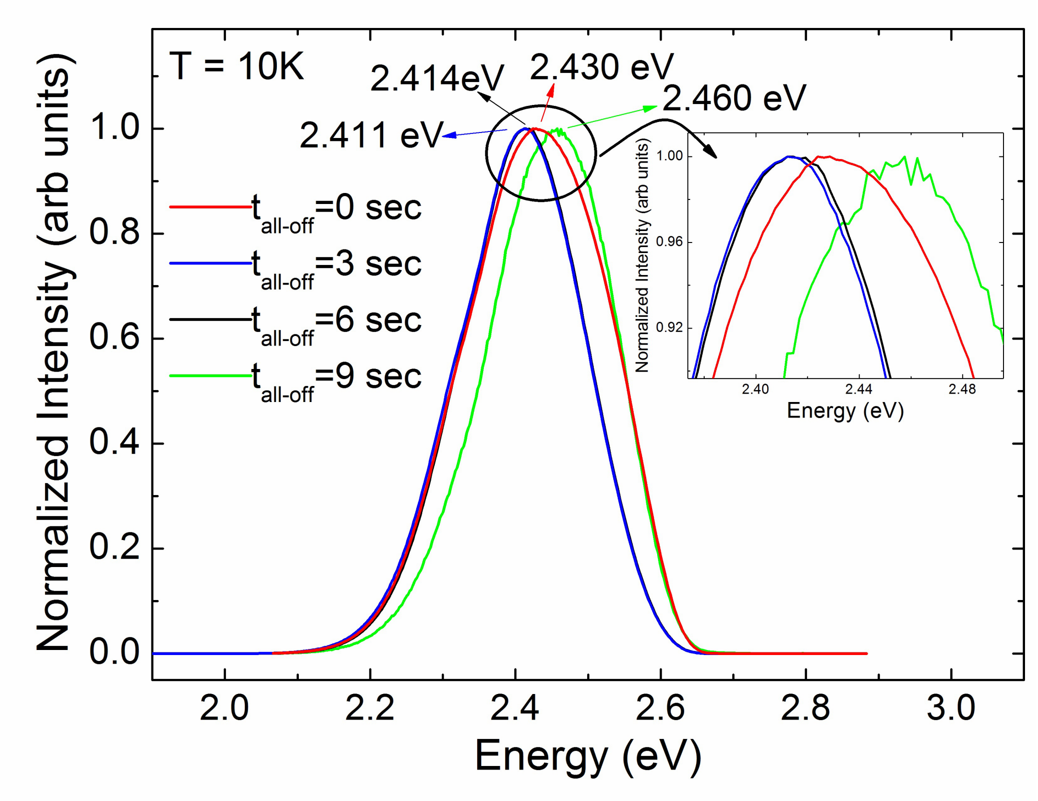

Figure 4.7: Low temperature PL of ZnTe/ ZnSe QDs grown with different $t_{\text{all-off}}$.

intensity over three orders of magnitude (shown in Figure 4.8).

As explained above, the blue shift is due to the presence of type-II QDs where the band bending and the generation of excited carriers are dependent on the excitation intensity. The higher the excitation intensity, the larger is the band bending and the higher is the PL peak position, observed as the blue shift. As explained above, the magnitude of the emission energy shift may be seen as an indication of the size of the QDs. The shift is largest in sample D34 ($\sim$ 53 meV) followed by that in sample D (29 meV). Samples D30 ($\sim$ 15 meV) and D32 ($\sim$ 23 meV) show a smaller shift in the emission energy. This strengthens our prediction that smaller to larger QDs are present in samples D34, D28, D32 and D30, respectively. The excitation intensity dependence of the PL emission can also be accounted in terms of relative change in carrier concentration with varying the excitation intensity taking in account that the volume density of carriers is higher for smaller QDs at higher excitation intensity as

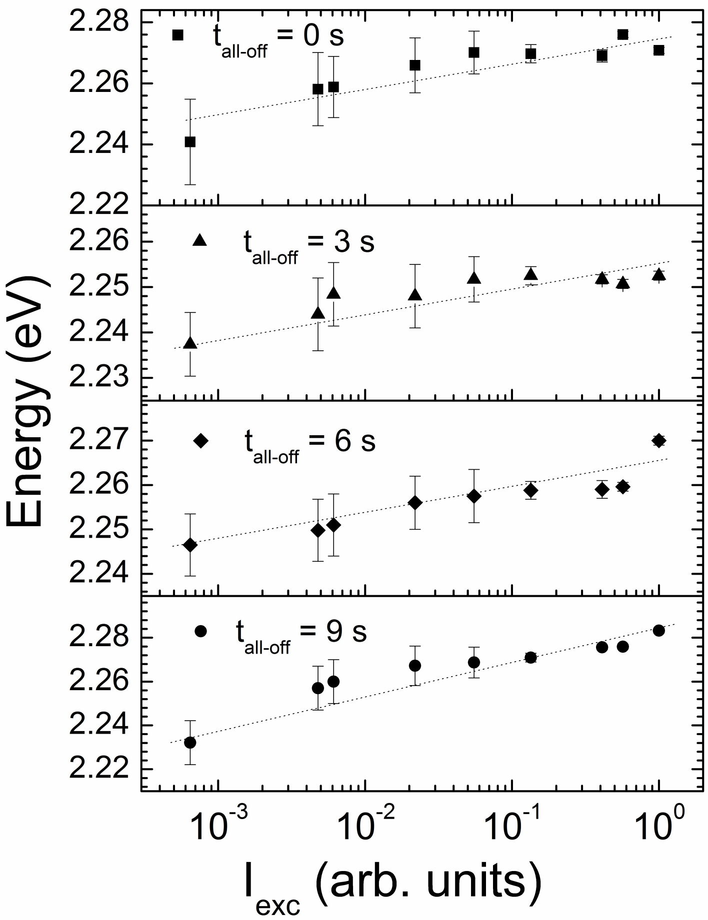

Figure 4.8: Excitation intensity dependence of the emission energy at 20% height of the peak on the low energy side for samples in series -II for varied $t_{\text{all-off}}$. The dotted lines are guides to the eye.

compared to that of the larger QDs.

The low temperature TRPL for samples from series II is shown in Figure 4.9. Although not significant, but indicatively, sample D34 exhibits faster decay, than samples D28, D30 and D32. This confirms the presence of smaller QDs in sample D34 due to the loss of Te ad-atoms through the process of desorption. At the same time, sample D30 exhibits relatively long lifetime as expected, due to formation of larger QDs as a result of diffusion and aggregation of Te ad atoms.

It may be further noted, that the difference in magnitude of the PL emission

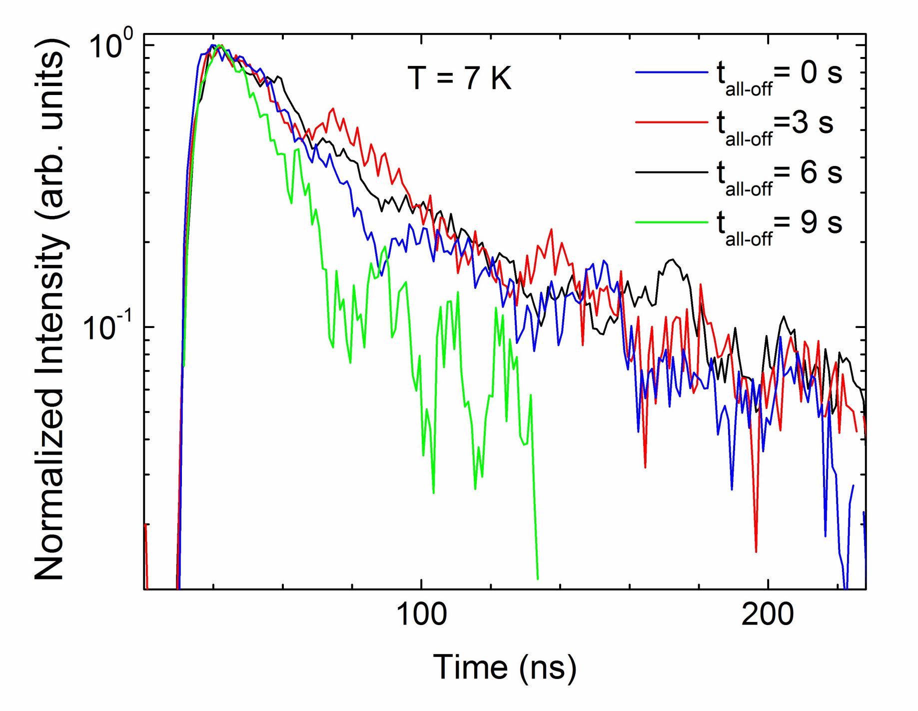

Figure 4.9: Low temperature TRPL of ZnTe/ ZnSe QDs grown with different $t_{\text{all-off}}$.

energy shift over the same order of magnitude change in the excitation intensity and also in the lifetimes between the various samples in series II is not as significant as compared to that in series I. Also, the peak positions for sample series II are relatively closer than that for sample series I, indicating more comparable size distribution in sample series II.

4.1.4 Conclusions

Optical studies showed that higher $T_{T_esource}$ facilitated higher Te flux which led to clustering of Te adatoms. We observed a signature of larger QDs formed with $T_{T_esource} = 245°\text{C}$ as compared with $T_{T_esource} = 225°$ and 215°C. Also it is shown that, while increasing $t_{\text{all-off}}$ from 0 to 3 s led to diffusion of Te adatoms and formation of larger dots, further increasing $t_{\text{all-off}}$ up to 9 s resulted in desorption of Te adatoms, leading to smaller QDs. Low temperature PL and excitation intensity dependent PL along with TRPL studies support our conclusions.

Chapter 5

Excitonic AB-effect in type-II ZnTe/ ZnSe stacked quantum dots

In this chapter we will discuss our findings on observation of excitonic Aharonov-Bohm (AB) effect via magneto-optical emission in stacked type-II ZnTe/ ZnSe submonolayer quantum dots.

5.1 Sample information

As explained in Chapter 5, samples were grown by following specific MEE shutter sequences with submonolayer insertion of Te in the Zn-Te-Zn deposition cycle sandwiched between the ZnSe barrier layers. Detailed Optical and Magneto Optical studies were performed on various samples. We will concentrate on three samples D55, D50 and D51 for these discussions. Sample D55 was grown with a single Zn-Te-Zn deposition cycle, while sample D50 and D51 were grown with three such deposition cycles with low and high Te fluxes, respectively. The relevant sample information are listed in Table 5.1.

Sample	Zn-Te-Zn Deposition Cycle	Te Flux (10^{-7} Torr)	B_{AB} from Magneto-PL
D55	Single	0.26	2.02 T
D50	Triple	0.24	2.06 T
D51	Triple	0.38	1.93 T

Table 5.1: Sample information

5.2 Structural information

HRXRD analysis was performed in order to extract relevant structural parameters. Figure 5.1 shows the $\omega - 2\theta$ curves for samples D50 and D51 respectively along (004) reflection. HRXRD peaks corresponding to the GaAs substrate along (004) reflection for both samples. The sharpness and intensities of the visible superlattice (SL) peaks up to second order are indicative of high crystalline quality of the samples. Other than the SL peaks, an additional peak corresponding to GaAs (004) is observed.

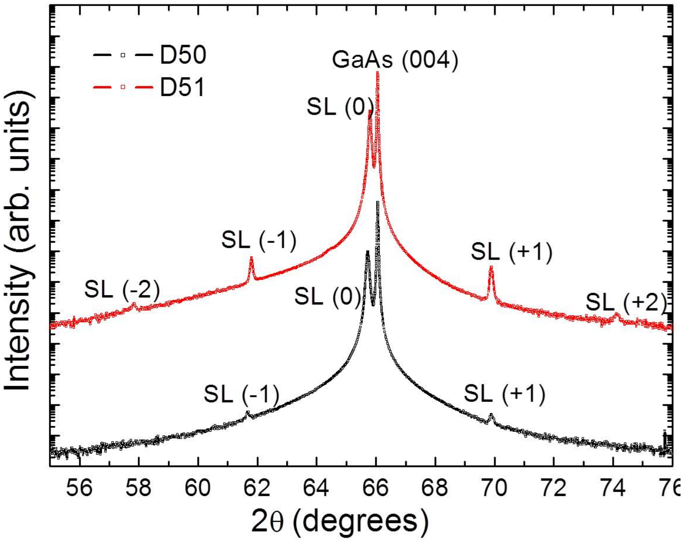

Figure 5.1: HRXRD plots along (004) reflection for samples D50 and D51.

The superlattice period is obtained to be $\sim$ 2.55 nm for both samples. The calculated in-plane lattice mismatches of the SL structures for samples were found out to be relatively small, $\sim$ 0.12-0.13 for both. The vertical lattice mismatch of the SL was found to be $\sim$ 0.41 for sample D50 and $\sim$ 0.38 for D51. The SL strain is $\sim$60 percent for both samples.

5.3 Optical Characterization

The low temperature ($\sim$ 10 K) PL of sample D55 (shown in Figure 5.2(a) for two different excitation intensities) consist of a broad blue band overlaid with sharp lines (at $\sim$ 2.66, 2.695, 2.726, 2.757 and 2.767 eV) along with small peaks at $\sim$ 2.693, 2.717, 2.748 and 2.765 eV. The first two sharp lines with higher energy are zero phonon lines (2.767 and 2.757 eV); one can see at least three phonon replicas at 2.726, 2.695 and 2.66 eV (ZnSe LO phonon energy is $\sim$ 31 meV).

Apart from the distinctive sharp lines generally seen in samples grown with minimal Te concentration, this sample shows the signature of co-existence of Te($n \geq 2$) isoelectronic centers (ICs) and the QDs [94]. The latter could only be observed at elevated temperatures, when the band edge PL is suppressed due to thermal ionization of isoelectronic bound excitons (IBEs)[94]. Excitation intensity (I_{exc}) dependent PL at low temperature does not reveal significant shift in peak energy for the blue band dominant transitions as shown in the inset of Figure 5.2(a), the excitation intensity dependence of emission energy at 20% height of the peak on the lower energy side.

Low temperature PL for sample D50 with triple deposition cycle but comparable Te flux (to that of sample D55) is shown in Figure 5.2(b). The QDs dominant PL (generally seen as a broad green band' with peak around 2.5 eV, and sometimes with a low energy shoulder,[78] and as low as 2.3 eV [88, 95]) is convoluted with the emission due to IBEs [39]. This triple-cycle sample exhibited a high degree of separation of QD containing layers from the barriers as observed by the presence of the band edge emission, which previously was seen only in samples grown with a single Zn-Te-Zn MEE cycle (e.g. as seen in sample D55) [94]. We note that the sharp lines are seen at same energies ($\sim$ 2.66, 2.694, 2.726, 2.757 and 2.767 eV) as for sample D. Two different excitation intensity PL plots are overlaid for eye guidance. The excitation intensity dependent PL (inset of Figure 5.2(b)), showed blue shift of $\sim$ 37 meV in emission energy at the green band energy position, which is a consequence of carrier concentration dependent band bending effect for spatially separated charged carries

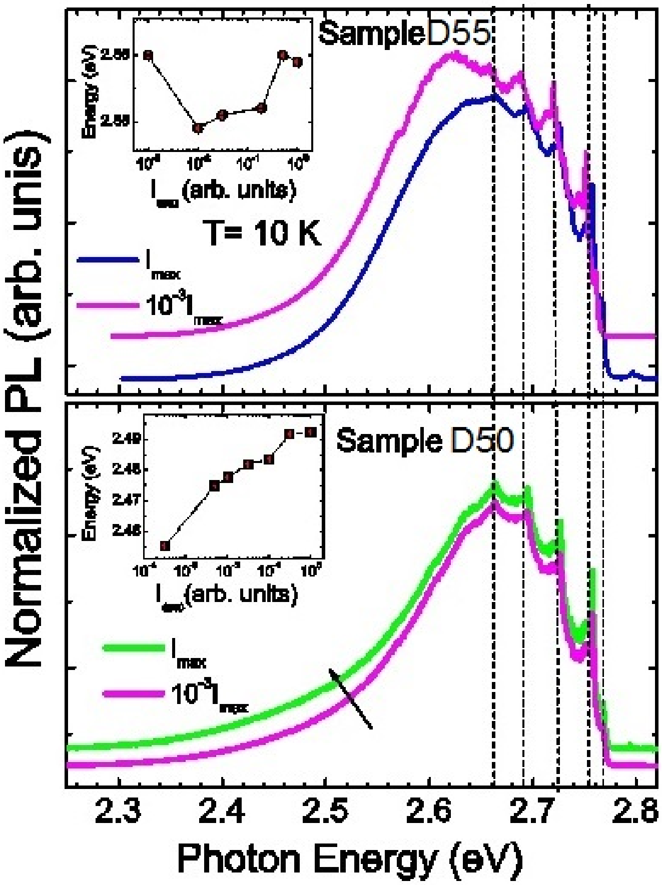

Figure 5.2: Low temperature PL of a) Sample D55 and b) Sample D50. The respective insets show the excitation intensity dependence of PL emission energy for each. Vertical dashed lines are for eye guidance comparing the spectral position of sharp lines for the two samples

in type-II excitons.

The PL at 10 K for sample D51 is shown at two different excitation intensities in the inset of Figure 5.3. Three Gaussian peaks were used to decompose the PL spectrum; the ‘green band is formed by two Gaussians (“Green band 1” at ~ 2.52 eV and “Green band 2” at ~ 2.4 eV) while the third Gaussian represents the blue band at$\sim$ 2.67 eV. As reported previously [39, 95], in these systems, the PL of the QDs (generally seen as ‘green bands’ $\sim$ 2.5 eV and as low as 2.3 eV [88]) is convoluted with the emission from excitons bound to isoelectronic centers (ICs) of various sizes Te($n \geq 2$) (generally seen as ‘blue band$\sim$ 2.6 eV and higher energy shoulders). The

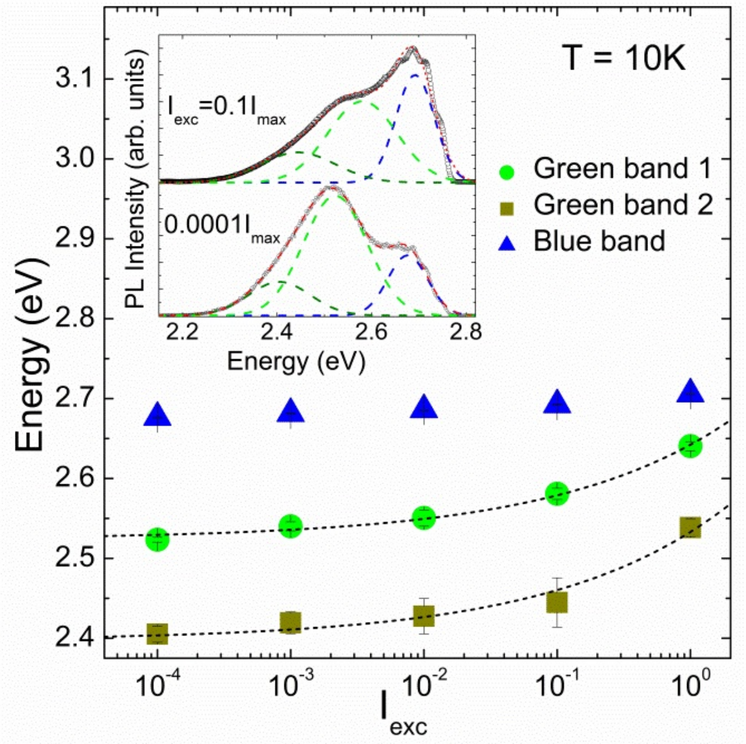

Figure 5.3: Low temperature PL behavior of Sample D51- Plot of PL 'green' and 'blue' bands as a function of excitation intensity (I_{exc}); dashed line is the result of fitting with $I_{exc}^{1/3}$. Inset: Low temperature (10 K) PL at two different I_{exc}. The spectrum is decomposed into three Gaussian peaks.

excitation intensity dependence of each of the three decomposed Gaussian peaks is shown in Figure 5.3. The "Green" bands 1 and 2 exhibit large shift (∼116 meV and ∼133 meV, respectively) when I_{exc} is varied over four orders of magnitude. Such a shift that closely follows the cube root of I_{exc} (fitted by dashed lines in Figure 5.3). The IC-bound exciton dominated 'blue' band shows a relatively smaller shift of ∼31 meV, which may be related to its significant overlap with the QD- related band. Evidently, with decreasing the excitation intensity, the QD PL starts to dominate, as the IC-related transitions are suppressed.

5.4 Magneto-PL studies

5.4.1 Narrow-Robust AB 'oscillations': Built-in electric field

Our samples can be described by a model considered in [94]; the samples are stacks of multiple ZnTe-rich disks, containing strongly confined holes, while the electrons are located in the ZnSe barriers (Figure 5.4 shows a schematic of the model). It is assumed that not all QDs are occupied by holes, and electrons move around a whole stack attracted by Coulomb interaction with the holes across the barriers. Such a configuration averages out the QD size variation and ensures cylindrical symmetry, which is ideal for the observation of AB effect. Due to the cylindrical symmetry, the exciton ground state in stacked type-II disk-like QDs initially has a zero orbital angular momentum, which changes to higher values with increasing magnetic field (See detailed discussion in Chapter 3). This transition of the angular momentum to a non-zero value influences the optical properties as [71]: the ground state energy oscillates as the orbital angular momentum states cross and the PL intensity changes due to optical selection rules. Experimentally, the latter is often observed as one or more oscillations ('peaks'), which can arise due to such factors as QD shape

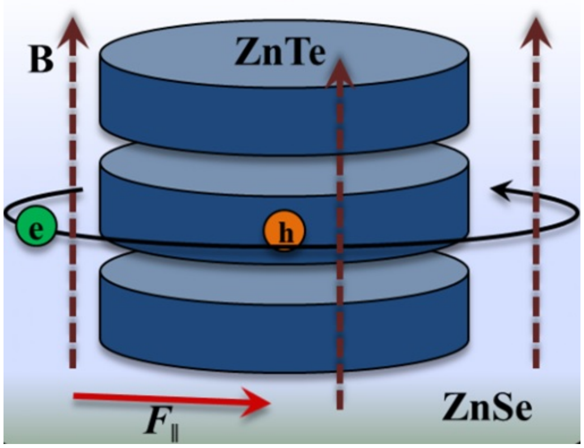

Figure 5.4: Schematic of the stacking of QDs; type-II exciton is comprised by electron in ZnSe and hole strongly confined within the ZnTe QD. The Magnetic field (B) is applied in the Faraday geometry. Such a geometry is ideal for observation of AB effect. F_x indicates the $x-$ component of built in electric field in the system.

anisotropy, e.g. elongation [17], presence of impurities [84], and/or built-in electric field [96]. In such cases the excitonic states do not possess a definite value of the angular momentum and optical selection rules are relaxed. Also in real experimental conditions where the whole system is in the magnetic field, the wavefunction of one carrier is "squeezed" closer and "pushed" away to the QD boundary before and after the angular momentum transition, respectively, that leads to an increase followed by a decrease in the PL emission. In the case one of the carriers is strongly confined in the QDs, as the hole in our material system [17, 78], the lowest exciton state as a function of the magnetic field undergoes the transition to non-zero orbital momentum at such a magnetic field, B_{AB}, that

$$\pi R_e^2 B_{AB} = \Phi_0/2 \tag{5.1}$$

where $\Phi_0 = h/e$ is the universal flux quantum, R_e is the radius of the electronic orbit, h and e are the Plancks constant and the electron charge, respectively.

In Figures 5.5 (a), (b) and (c) we show, the normalized integrated PL intensity as a function of the normalized magnetic flux for samples D55, D50 and D51 respectively. All three samples showed AB oscillation in the integrated intensity which confirmed the presence of type-II QDs. The respective insets show the peak at B_{AB} values $\sim$ 2.02, 2.06 and 1.93 T for each sample. Using Equation 5.1, the characteristic radius of electronic orbit was determined to be 18.0, 17.8 and 18.4 nm for sample D55, D50 and D51 respectively. The initial drop in emission intensity is attributed to magnetic field induced carrier trapping effects at interfaces [17] (this requires further investigation and will be discussed in the last chapter).

Considering that the stacking of QDs results in averaging out size variations in QDs and that at low temperature the $L = 0$ (i.e. ground state) dominates, the magnetic flux was calculated for corresponding area enclosed by the electron trajectory with the goal to compare our observations with theoretical calculations for QRs [97]. The AB peak is at $\Phi_0/2$ in normalized flux units. The magnitude of the AB oscillation relative to the background in integrated PL is $\sim$ 3 to 4% for these samples. We will show in later sections that the magnitude of the oscillations is even larger for specific emission energies, and it reaches 6% for sample D55 and 4% for samples D50 and

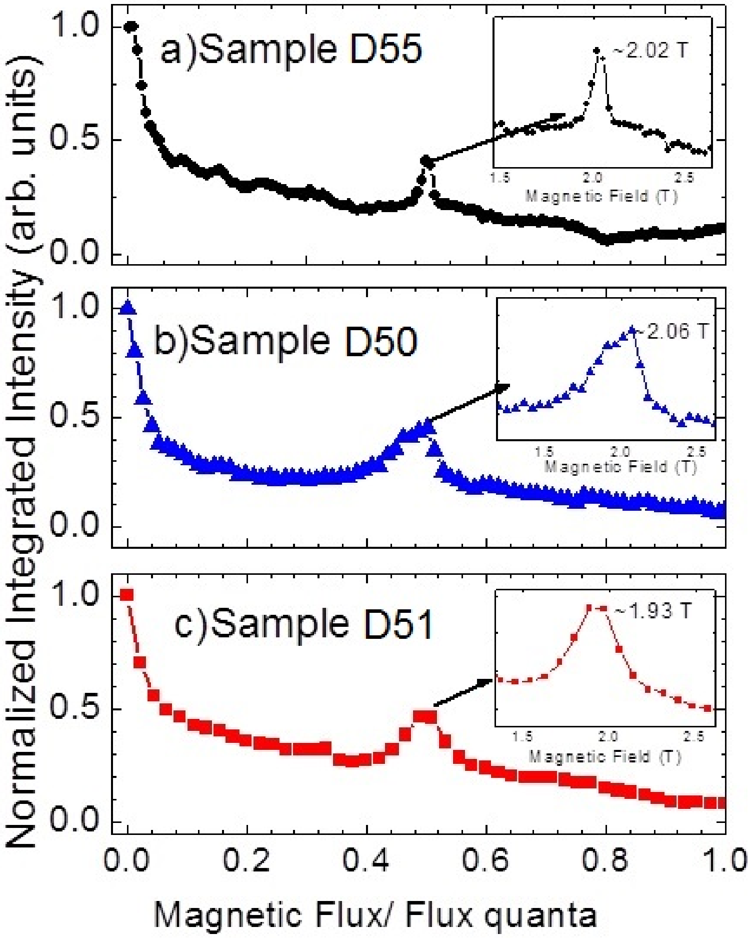

Figure 5.5: Normalized integrated PL intensity as a function of normalized magnetic flux a) Sample D55; b) Sample D50; c)Sample D51. Insets show enlarged peak region as a fucntion of the magnetic field.

D51. The full-width-at-half-maximum (FWHM) of the oscillation in the normalized magnetic flux is ∼0.02 for sample D55 and ∼0.06 to for samples D50 and D51. Such magnitude of the AB oscillation peak is larger [79, 80] and the peaks are significantly narrower [79, 80, 96] than the values reported literature for both QDs [79, 80] and QRs [96, 97].

We compare the widths of the AB 'peaks' with theoretical predictions available for type-I QRs [97] even though there is a critical difference between two system, since we are not aware of such calculations for type-II QDs. Without the electric field, the FWHM of ∼ 0.3 in units of normalized magnetic flux has been predicted for the bright excitons. This is substantially wider than what we observe for our samples; however, if one assumes a presence of a strong in-plane electric field ($u_0 = 0.3$ in Ref. [97] notations) then the observed FWHM can easily be explained and understood. For a direct comparison, Figure 5.6 shows the calculated oscillator strength (black curves) as a function of normalized flux which is overlaid by our data (green and orange curves. For the bright excitonic states, it is clearly observed that the oscillation in oscillator strength decreases with increasing the applied in-plane electric field. Our data indicates, the presence of an in-built electric field from this direct comparison.

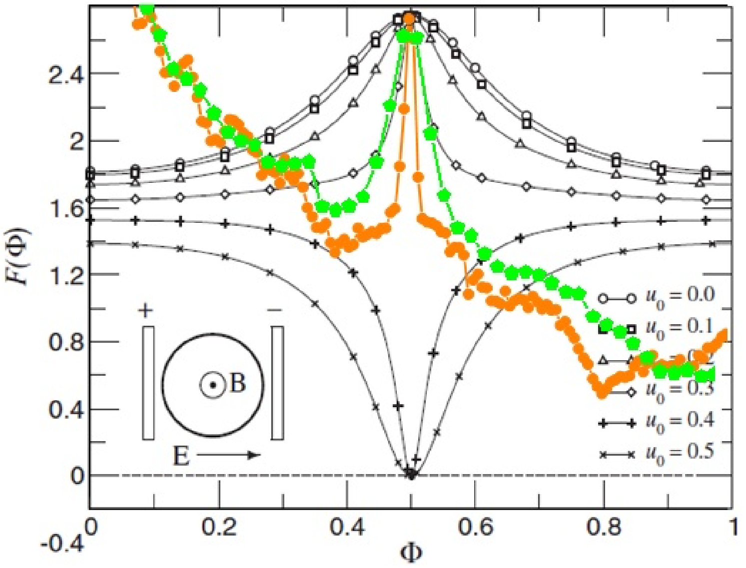

Figure 5.6: The calculated oscillator strength (black curves) as a function of normalized flux (from ref. [97]) which is overlaid by our data (green and orange curves) showing comparable width of AB peaks (for bright excitonic state) in the presence of electric field.

Moreover, the electric field also leads to enhancement of the AB effect [76, 96, 98], explaining such robust oscillation. For instance, in the presence of the built-in electric field, a relatively large (∼9%) AB oscillation in intensity was seen for some of the QRs described in Ref. [96].

Built-in Electric field: Temperature dependent PL

The signature of presence of built-in electric field has been theoretically investigated via calculation of oscillator strength (shown in Figure 5.7(b) taken from Ref. [96]) and also experimentally observed for InAs/GaAs QRs (Figure 5.7(a) taken from [96]). An initial increase of PL intensity was seen with increasing temperature for the case with presence of built-in electric field. It was suggested that with electric field, the oscillator strength can increase by the activation of more efficient channels for optical recombination at excited states with e-h separation smaller than in the ground state.

We also investigated the temperature dependence of PL to verify the presence of built-in electric field in our system. In Figure 5.7 (c), the behavior of integrated intensity of each of the three contributing bands from the PL of sample D51 (as decomposed in Figure 5.3) is shown as a function of temperature.

The decrease of the PL intensity with increasing temperature is expected, due to the increase in non radiative transitions and luminescence quenching. However, we also observed an initial increase of the PL intensity with temperature for $T < 80$ K which is eminent at the QD dominated lower energy green band (2.48 eV).

Clearly, we observed a similar temperature dependent PL behavior (as predicted and experimentally observed for InAs/GaAs QRs [96] which confirmed the presence of built-in electric field in their system but we also note that the initial increase is seen for the lower energy green band in our case. Thus, we cannot completely disregard and distinguish the probability and contribution from carrier redistribution effects with increasing temperature, however along with the narrow and robust AB oscillation (and the comparisons done in previous section), this observation only strengthens the possibility of built-in electric field in our system.

Built-in electric field: Discussions

The built-in electric field in a zinc-blende system grown along [001], like ours, can have piezo-electric origin due to anisotropic strain [99, 100].

In our system, during the QD growth, the strain fields arise due to the lattice

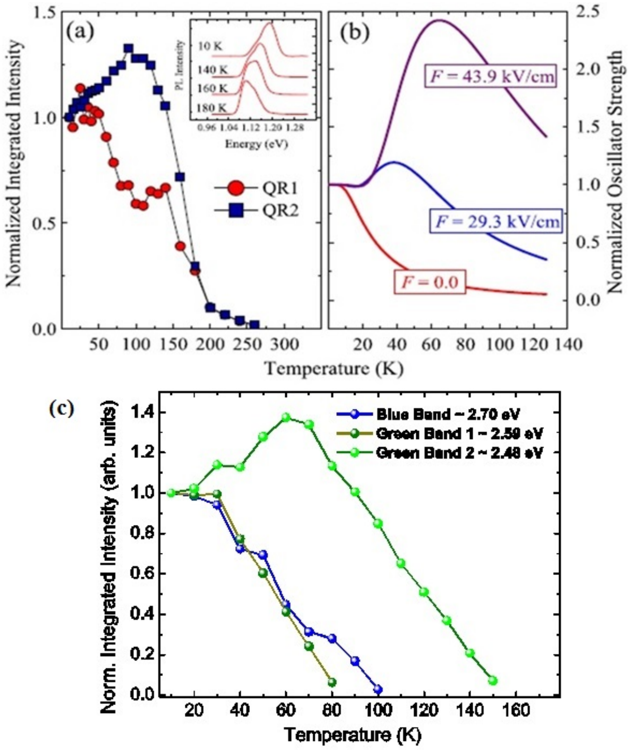

Figure 5.7: Temperature dependent studies: (a) PL integrated intensity for InAs/ GaAs QR taken from Ref. [96] (b) Theoretical calculation for Oscillator strength in the absence and presence of built-in electric field in InAs/ GaAs QRs, taken from Ref. [96] (c) PL integrated intensity behavior of the different bands in Sample D51 (type-II ZnTe/ ZnSe stacked QDs) showing initial increase in QD dominant green band, indicating presence of built-in electric field.

mismatch between the ZnTe QDs and ZnSe matrix [101]; the anisotropic nature of the strain is supported by the following observations:

(i) as reported previously some QDs in these systems are elongated [17], which can lead to anisotropic strain, similar to that reported for InGaAs/GaAs QR [96];

(ii) the vertical correlation, required to form stacks, strongly indicates the presence of elastic anisotropy that plays crucial role for effective lateral and/or vertical self-organization in QD superlattices[102]; vertical correlation of stacked QDs in a similar system of type-II ZnMgTe/ZnSe superlattice was reported recently [103].

We hope to stimulate the theoretical investigations of the magnetic field-dependent oscillator strength with and without the presence of an electric field, for type-II QDs specifically, in order to confirm our hypothesis.

Chapter 6

Distinguishability of QD stacks via optical studies and Spectral Analysis of AB effect

In this chapter we discuss a unique approach to get insight into material structure of the samples. Spectral analysis of Magneto-PL measurements on the samples D55, D50 and D51 (which exhibited AB oscillations and were discussed in the previous chapter), along with spectral studies of time resolved PL results will be put forward to show that one can distinguish the presence of different stacks in these systems.

6.1 Spectral Analysis of AB Peaks

The AB oscillation in PL intensity has been most commonly reported in terms of integrated PL intensity [17, 78, 80, 96] or PL peak intensity [104], which can not distinguish the contribution from different emission centres in the ensemble QR or QD system, and can be seen as an overall averaged interpretation. We, however, studied the evolution of the AB oscillation, at spectral energies across the PL spectrum.

In Figures 6.1, 6.2 and 6.3 for samples D55, D50 and D51 respectively, the AB peaks in PL intensity are shown at three different spectral energies, corresponding to the lower and higher energy sides as well as the peak of the spectrum.

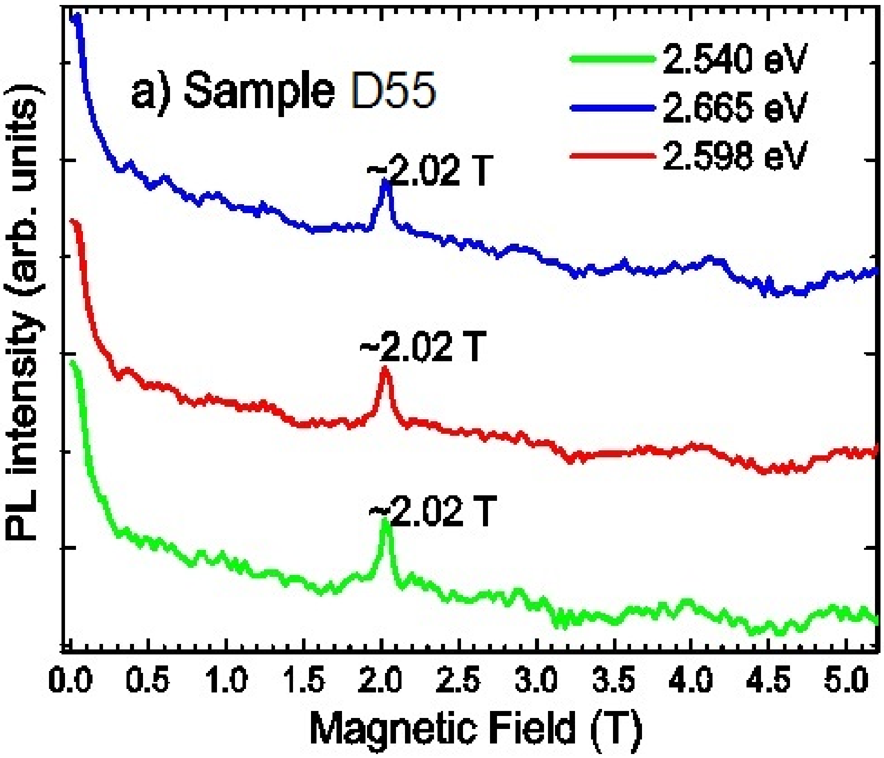

Figure 6.1: Magneto-PL at three spectral position of spectrum of Figure 5.2 (a), showing the AB oscillations in Sample D55.

We derive interesting observations, e.g. for sample D55, the AB peak is seen at a constant B_{AB} value of ~ 2.02 T for all three energies (2.540, 2.598 and 2.664 eV), whereas for sample D50, the AB oscillation (displayed for spectral energies 2.465, 2.520 and 2.641 eV) show a distinctive change in values of B_{AB}. Moreover, careful examination of the transition region clearly displays, a "double AB peak", as plotted for 2.52 eV, for sample D50 (inset of Figure 6.2). For sample D51 we show AB oscillations at energies 2.318, 2.480 and 2.650 eV are seen with B_{AB} showing changed values $\sim$ 1.88, 1.925 and 2.05 T respectively.

As seen from Equation 5.1, the B_{AB} value is determined by the radius of the electronic orbit. So we infer for samples D50 and D51, that the electronic orbit changes across the PL spectra, which signifies the presence of more than one stacks of QDs with different effective radii for the orbiting electron. For our sample system, where in the hole is strongly confined within the ZnTe QD, the radius of electronic

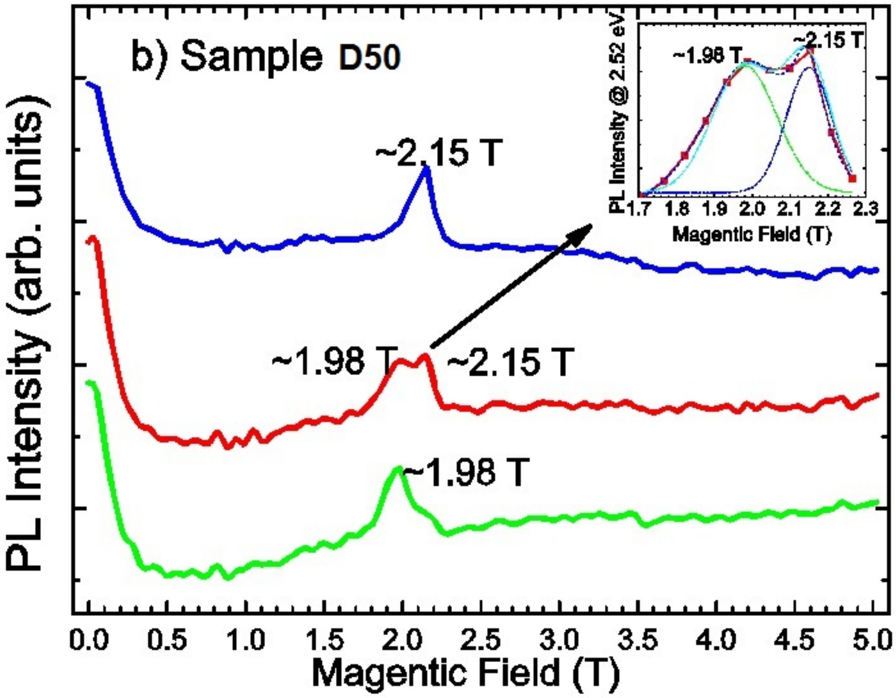

Figure 6.2: Magneto-PL at three spectral position of spectrum of Figure 5.2(b), showing the AB oscillations Sample D50. Inset shows enlarged picture of double AB peak as seen in sample D50 at 2.52 eV.

orbit in ZnSe is essentially the lateral spread of the type-II exciton. Thus, the probing of precise B_{AB} values across the spectra allowed us to determine the lateral size of the type-II exciton with sub-nanometer precision [82]. This is remarkable information for submonolayer QDs considering the fact that they are hard to be imaged. In sample D55, however, B_{AB} does not change significantly, so the radius of electronic orbit is the same across the spectrum; we conclude from such an observation that only one QD stack is present in sample D55. We also note that the FWHM of each of the AB peaks (0.12 to 0.17 T, shown in inset of Figure 6.2) comprising the 'double peak' in sample D50 is comparable to the FWHM of the AB peak in sample D55 (0.14 T), suggesting that two QD stacks in sample D50 have similar properties to the QDs of sample D55. This also suggests that both samples have a similar built-in electric field, which originates in the lattice mismatch between ZnTe and ZnSe. We note, that for sample D51 a broadening of AB peak FWHM (originally 0.3 T) is observed rear the

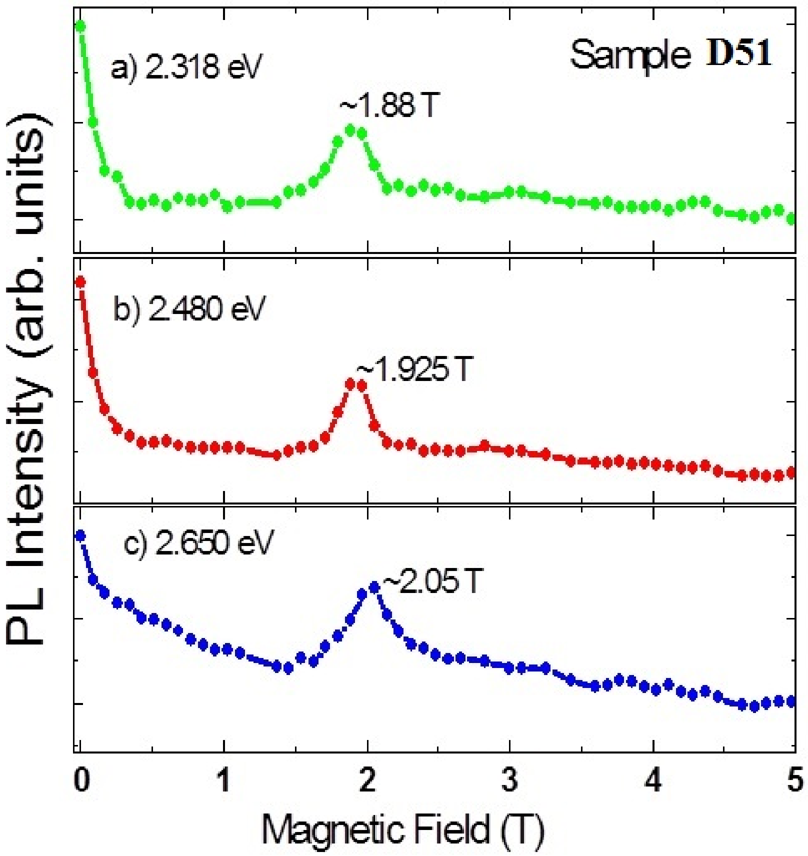

Figure 6.3: Magneto-PL at three spectral position of spectrum of Figure 5.3(a), showing the AB oscillations Sample D51.

transition region which indicate contribution from different stacks at such energies.

To strengthen these conclusions and to obtain a more complete picture, we show in Figures 6.4 and 6.5, the behavior of AB oscillations as a function of the spectral energies for the three samples.

Figures 6.4 (a)-(c) show the spectral analysis of low temperature magneto-PL in sample D55. The spectral behavior of B_{AB} and the magnitude of oscillation are plotted in Figures 6.4 (b) and (c) respectively which are related to the PL shown in Figures 6.4 (a). The magnitude is determined w.r.t. the background emission intensity.

No significant change in B_{AB} across the spectral positions was observed for sample D55 which indicates almost no distinguishable excitonic size variation. The PL

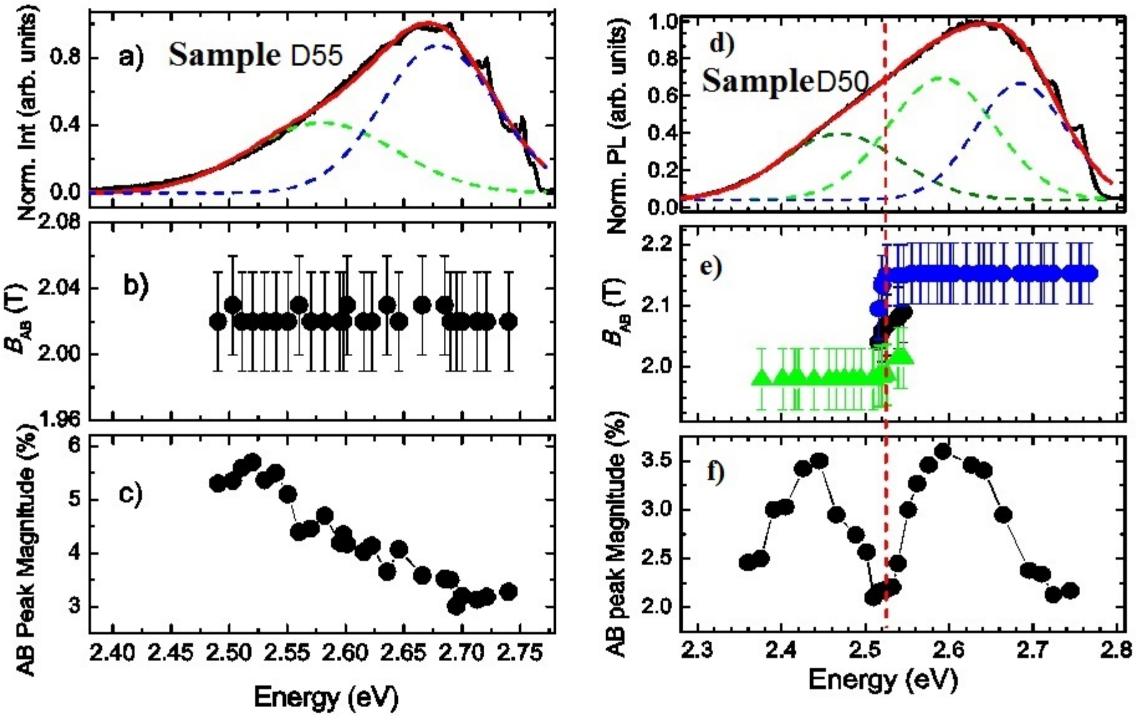

Figure 6.4: Spectral Analysis of AB oscillations in sample D55: (a) PL spectrum decomposed into two Gaussians; b) B_{AB}; (c) Magnitude of the AB oscillations, Spectral Analysis of AB oscillations in sample D50: (d)PL spectrum decomposed into three Gaussians; (e) B_{AB}; (f) Magnitude of the AB oscillations,

spectrum is decomposed into two Gaussian peaks (Figures 6.4 (a)) attributed to the presence of 'green' ($\sim$ 2.56 eV) and a cumulative blue ($\sim$ 2.68 eV) band which can be associated with the QDs and ICs dominated emissions, respectively.

The spectral plots of B_{AB} and the magnitude of oscillation for sample D50 are shown in (Figures 6.4(d)-(f). We observe B_{AB} changes from a lower value of $\sim$1.98 T at the lower energy side (below $\sim$2.47 eV) to a higher value of $\sim$2.15 T at the higher energy side (above $\sim$2.55 eV) for this sample. The error in determination of B_{AB} is less than the observed change (also displayed in the plot). An average of the B_{AB} is represented from the two peaks as observed in the 'double AB peak' (Figure 6.4(e) to indicate the transition in B_{AB}. The 'double peak' B_{AB} values are also shown in (Figure 6.4(e) (blue and green markers) for the transition spectral region. The transition of B_{AB} from a lower value to a higher one is observed within a relatively narrow spectral range between 2.49 and 2.54 eV.

To relate such an observation to the PL spectra, three Gaussian peaks were used to decompose the PL (Figure 6.4 (d)) ; the 'green' band is formed by two Gaussians ('Green band 1' at ~2.59 eV and 'green band 2' at ~2.48 eV) with comparable weights, while the third Gaussian represents a "combined" 'blue' band for the higher energies dominated by the IBEs. Under such conditions, the best fitting resulted in a "reduced" overlap of the lower energy Gaussians in the close proximity of the spectral region of interest, indicating that the change in transition field is observable due to the subdued emission from the two overlapping PL bands. The contribution from two different type-II excitons also explains the asymmetry of the AB peak in the integrated intensity of sample D50, as the emission of one of the excitons dominate in a specific spectral region.

Figure 6.5 (a)-(b) show the spectral analysis of AB oscillations in intensity for sample D51. The spectral behavior of B_{AB} is (Figure 6.5 (a)) is shown to relate to the PL spectra (in magneto-PL conditions) shown in Figure 6.5 (b).

The value of B_{AB} changed from 1.88 T (below ~2.37 eV) up to 2.02 T (above ~2.62 eV) and the variations are measurable beyond the experimental error. The size of type-II excitons from observed values of B_{AB} for different QD stacks ranges from 18.7 to 18.0 nm, for the lowest and highest obtained values of B_{AB}, respectively. The presence of different sets of QDs stacks is clearly distinguishable within the region of transitions in B_{AB}. The PL spectrum (Figure 6.5 (b)) is thus decomposed into three Gaussian peaks which were used to include the contributions from the two 'green' bands (the lower energy green band at ~2.40 eV, the higher energy green band at ~2.49 eV), and a blue band ~2.66 eV with "reduced" overlap in the spectral region where the B_{AB} changes its value, for the changes in B_{AB} are observable due to the subdued emission from the overlapping bands in the PL. It is thus evident that different sets of QDs stacks are dominant at specific spectral regions in sample D51 as was also seen in sample D50.

The difference in the PL peak energy between the two stacks, estimated from the peaks of the two Gaussians used to form the green band, is ~150 meV for sample D50 and ~90 meV for sample D51. Such a larger difference is unattainable by any realistic

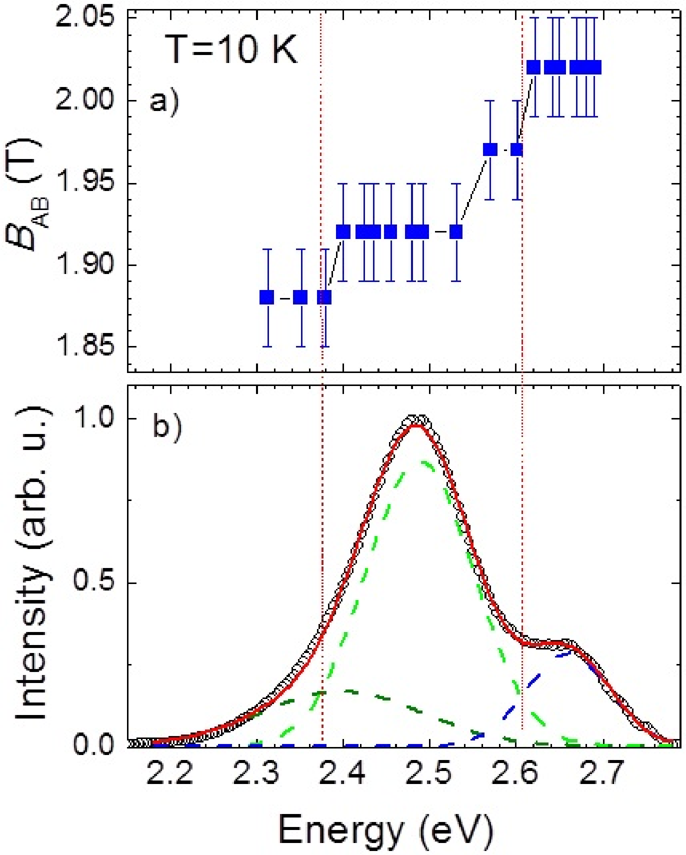

Figure 6.5: Spectral Analysis of AB oscillations in sample D51: (a) B_{AB} as a function of spectral energy; b) PL spectrum decomposed into three Gaussian bands .

change in the QD radius [1]; thus other factors, such as thickness, chemical composition of QDs, and strain, which can change the band offsets (which determine the potential seen by the electron), are also significant in understanding of the observed PL. Thus, we suggest that the two stacks are distinguishable not only in terms of radius of electronic orbit or the lateral sizes of QDs, but also due to the change in QD thickness and/or change in the band offsets because of the variations in Te composition.

---

[1] We calculated the hole confinement energy inside a cylindrical dot of radius a and thickness d; The energy is given by $E = \frac{\hbar^2}{2m_h^*}[x_{ms}^2 + \frac{n_z^2\pi^2}{d^2}]$ where m_h^* is the effective mass of hole in ZnTe, x_{ms} are the solutions for $\frac{J_1(x_{ms})}{J_0(x_{ms})} = \frac{N_1(x_{ms})}{N_0(x_{ms})}$ where $J(x_{ms})$ and $N(x_{ms})$ are the Bessel functions of the first and second kind, respectively taken for m=0 and s=1. For ground state $n_z = 1$ and with realistic values of dot radii ~9 to 11 nm, $d = 1$ nm, the energy is observed to change by ~ 0.1 to 0.2 meV only. For details: see Appendix 2.

Spectral variation of magnitude of AB peak

The spectral variation of the magnitude of the AB peak for samples D55 and D50 are shown in Chapter 6 (Figure 6.4 (c) and (f), respectively) The magnitude of an AB oscillation is expected to be related to the change in the oscillator strength of the exciton during the AB transition. The change in the oscillator strength is predicted to be smaller with a larger oscillator strength (or the overlap integral between electron and hole wavefunctions) in QRs, due to favorable AB configuration [76], whereas no such theoretical predictions for type-II QDs are available, to the best of our knowledge. Our observations, however, contradict this conclusion at least partially, as it would then be expected for 'smaller' dots, the stronger oscillator strength [76], would give rise to a smaller AB amplitude. In sample D55 we do observe such a trend in the magnitude of oscillation, even though we did not see any change in B_{AB} (which suggests almost constant size of the QD stacks). For sample D50, we observe a variation in the magnitude of the AB oscillation for both lower and higher energy sides of the spectra with a decrease in the AB amplitude at the transition spectral region. The maximum magnitude for each stack is almost the same, although the corresponding excitons have different sizes, and therefore different overlap integrals. We intend to address this aspect in greater detail in future work.

6.1.1 AB oscillations at IBE spectral energies

Interestingly, the AB oscillations were also observed at the spectral positions dominated by the ICs (sharp shoulders above 2.69 eV) as shown in Figure 6.6, although the magnitude of oscillation is decreased at such spectral positions, while the value of B_{AB} remained constant for all three samples (previously only integrated intensity over the whole spectrum, which might have included QDs, was reported [48]).

This suggests that even though oscillations are observed for the spectral range of IC, the QDs control the transition field. In the ZnSe:Te barrier, it is here the electron moves around the stack, the concentration of ICs is high, and thus, there is a finite probability for this electron to recombine with a hole localized at the IC rather than with the one confined within the QD. At zero magnetic field no differences

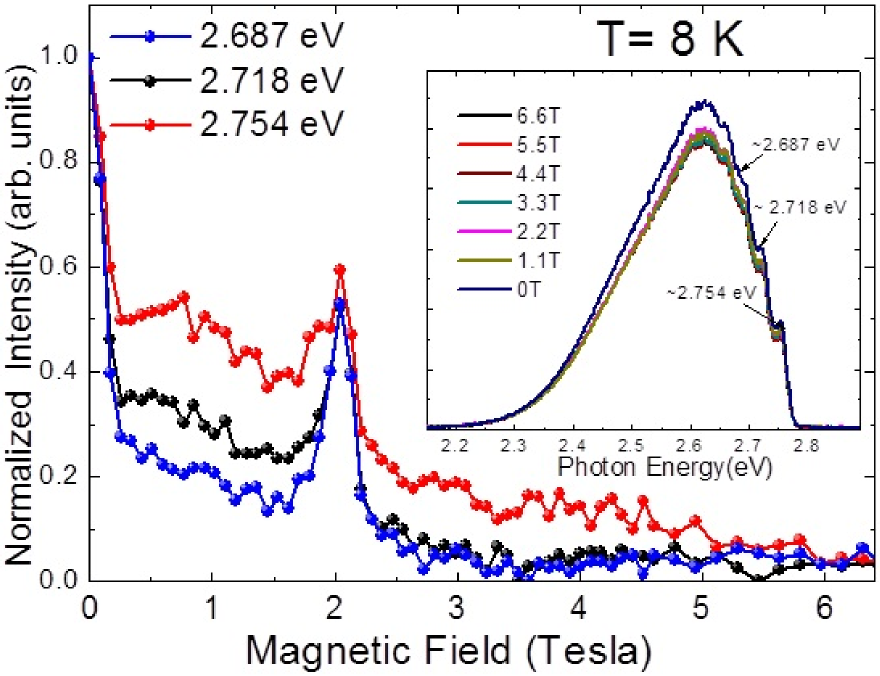

Figure 6.6: AB oscillation as seen at IBE dominant spectral energies.

in the PL intensity can be observed. However, in the presence of a magnetic field, the orbiting electrons that underwent the orbital momentum transition will carry the information of the acquired AB phase, and manifest it via the oscillation in the ICs-related emission. The constant value of B_{AB} at the IC dominated spectral positions, for all the three samples: 2.02 T (Sample D55), 2.15 T (sample D50) and 1.97 T (sample D51) suggest that the contribution from the low energy tail of the QD dominated emission bands may not significantly affect the AB oscillation at the spectral positions dominated by excitons bound to IC.

6.2 Distinguishable QD Stacks-Spectral Time Resolved PL

Further confirmation of distinguishability of QDs stacks within the ensemble system is obtained from TRPL measurements. The time decay curves at various spectral positions across the PL spectrum are shown in Figure 6.7 for samples B and C (that showed signature of different stacks from magnet-PL studies), respectively. A slower decay for lower energy side is observed as was also seen previously [88, 95] indicating dominance of 'larger' dots on lower energy side and 'smaller' dots and/or IC dominant transitions on higher energy side. Moreover, the PL emission decay curves exhibit a 'bundling' at the spectral regions of the green band (below 2.51 eV) and blue band (above 2.58 eV). We note that the decay curve 'bundles' are observed at spectral positions for which the B_{AB} values (as observed from spectral analysis of magneto-PL results) remained constant (e.g. between ∼2.4 to 2.5 eV and for ∼2.6 eV and above).

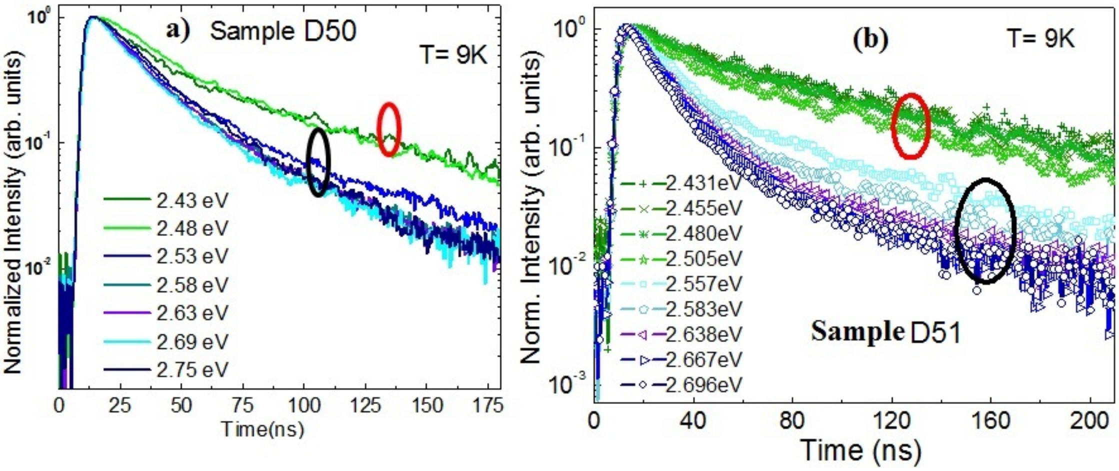

Figure 6.7: TRPL showing bundling of decay curves in green and blue spectral regions for samples a) D50 and b) D51.

We also suggest that initial decay is due to 'faster' dots, and the tail is dominated by 'slower' dots contributing via 'overlap'. As the lifetime of radiative recombination depends on the overlap of electron and hole wavefunctions (the larger the overlap, the faster is the decay), such an observation is a direct consequence of the presence of different QDs stacks with distinctive overlap of the wavefunctions, which is dependent on the lateral size of type-II excitons.

6.3 Conclusions

- Narrow and robust AB oscillations confirmed the presence of type-II QDs and strongly indicated the presence of built-in electric field.
- We probed the lateral size distribution of QDs in stacked type-II ZnTe/ZnSe system via a spectral study of the excitonic AB effect and also high precision estimation of radius of the electronic orbit was possible.
- Time resolved spectral studies demonstrated ‘bundling’ of decay curves at the ‘blue’ and ‘green’ spectral region which confirmed the presence of distinguishable QDs stacks.
- From all these studies it has been realized that lateral size distribution in the system is not significant and hence the broadening of PL is attributed to strong electron-phonon coupling.
- AB oscillation at spectral position dominated by excitons bound to ICs was experimentally observed.
- The behavior of magnitude of oscillation is not completely understood and we intend to address this issue in upcoming work.

Chapter 7

Outlook

7.1 Influence of AB effect on lifetime of magneto-excitons

We showed that cw-photoluminescence exhibits oscillation in emission intensity as a function of the magnetic field (flux) and explained it via the Optical AB effect. It remains, of particular interest to explore the influence of the AB- effect on the life time of the type-II magneto-excitons. The importance lies in the fact that at the transition field B_{AB}, the ground state of exciton traverses from optically 'Bright' to 'Dark' state. Consequence of this effect on the radiative life time has never been reported before.

With the goal of directly 'catching' the relative change in lifetime before and after the AB transition and measuring the life time of 'dark' excitons formed at the transition field, we performed many sets of magneto-TRPL measurements on our samples. Figure 7.1 shows time decay curves for sample D50 with applied magnetic field in the window of interest (AB transition peak was observed $\sim$2.1 T). From the data it is hard to observe any significant change while the double-exponential fitted lifetime as a function of magnetic field, (as shown in Figure 7.2) show nominal change near the transition region.

The lifetime shows a small decrease right before the AB transition peak ($\sim$2.1

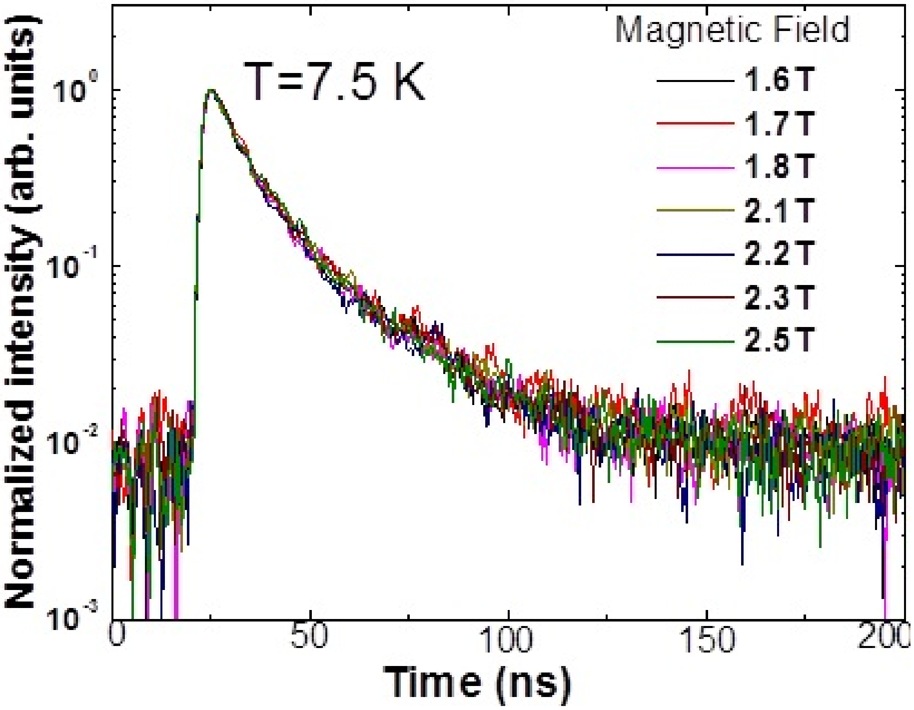

Figure 7.1: Low temperature magneto-TRPL: Time decay curves at various applied magnetic field values near the 'window' of AB-transition. This data is for sample D50 at 2.63 eV.

T) in magnetic field , which may be due to the 'squeezing' of e-h wavefunction as discussed before. Also, there is a increase following the transition (magnetic field window higher than 2.1 T) which is expected due to dominance of the 'dark' sates after transition. This change in life time, although consistent with our predictions, is very small and hard to be distinguished from the real data.

In reality, the excitonic recombination processes have contributions from both coherent and incoherent mechanisms. While it is true that the AB effect should affect the lifetime of the excitonic recombination, it remains hard to isolate the incoherent contributions that overshadow the overall change which remain order of magnitude smaller. It will likely be possible that at much longer times, when the coherent mechanisms survive, one may be able to 'see' the change in lifetime.

To our instrumental capabilities, we could not detect good signals at such longer times ($\gtrsim$ 500-600 ns). We aim to improve our collection optics with the aim of

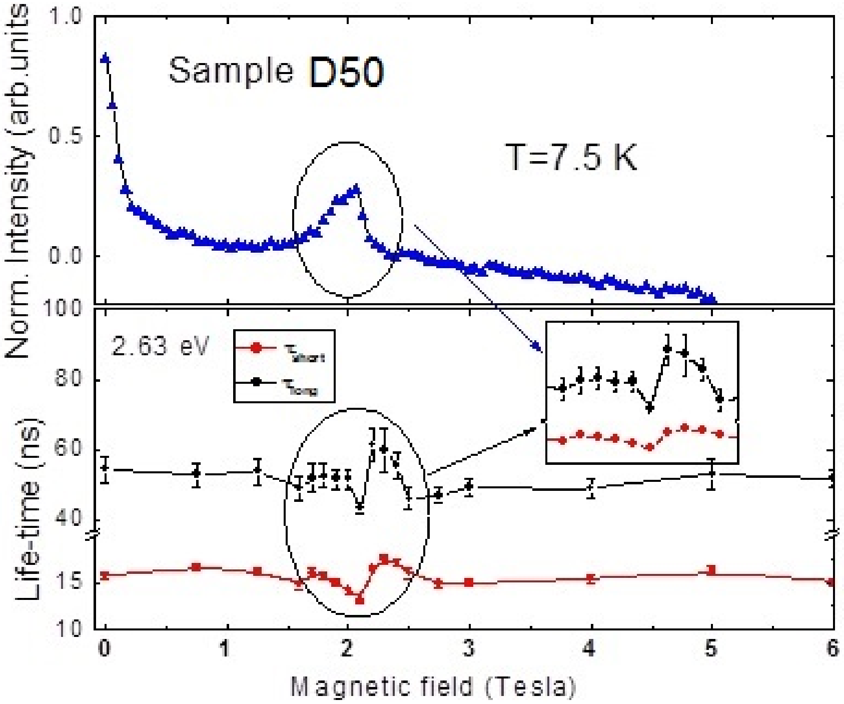

Figure 7.2: Double exponential fitted lifetime, as a fnction of magnetic field. The highlighted portion of the spectra is enlarged in the inset to show its possible correlation with the AB peak in intensity (shown on top panel).

increasing the dynamic range of the data and future endeavors will be made in this directions.

7.2 AB 'Oscillation' in Energy

The experimental observation of excitonic Aharonov- Bohm effect via optical emission is predicted to be observed for both intensity and energy. Previously, in Ref. [78], AB oscillation in energy was reported for ZnTe/ ZnSe QDs. From our recent samples and experiments, however, we observe narrow and robust AB oscillation in PL emission intensity (as discussed in Chapters 5 and 6), while the behavior of PL emission energy as a function of magnetic field is not very clear (Figure 7.3). We note a unique signature 'oscillation' which is not yet fully understood. To better understand this behavior we tried to correlate the observation with the emission intensity. And in

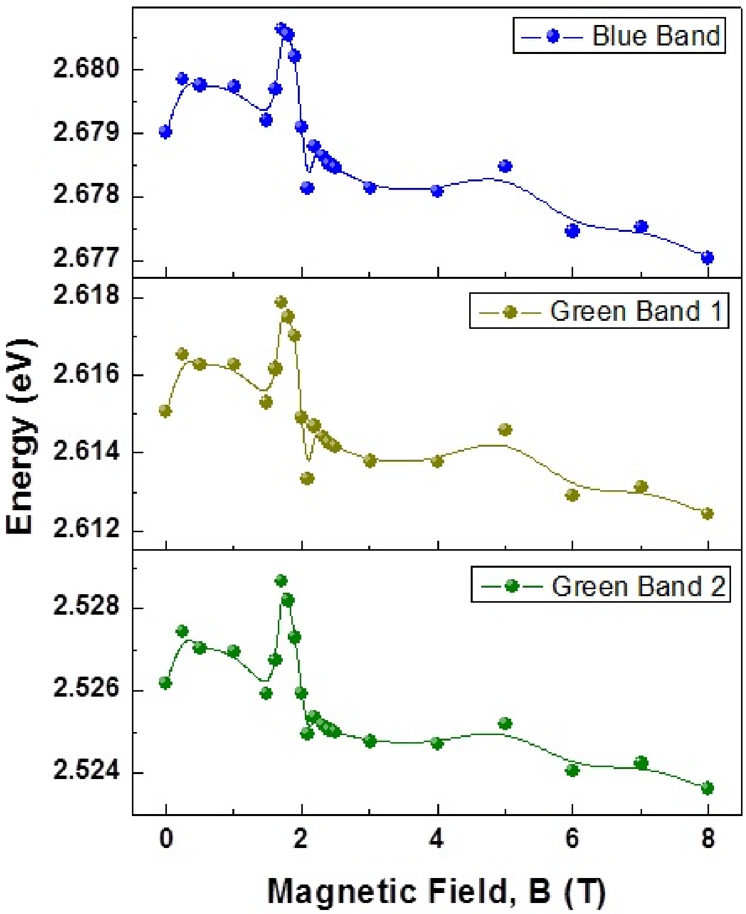

Figure 7.3: Energy 'Oscillation' for the green and blue bands contributing to PL, as a function of magnetic field-Sample D50.

Figure 7.4 we show the behavior of the emission energy at 30% of PL peak on the lower side (bottom panel) with the emission intensity as a function of magnetic field.

Although not completely clear the origin of such behavior, and considering the complexity of the real system and the fact that manifestation of AB energy is on much smaller scales, we suspect such behavior of energy is related to interplay of multiple processes. We propose that while the intensity is governed by the e-h overlap and population of bright/dark states within different windows of magnetic fields, the energy dependence on magnetic field is governed by the interplay of Coulomb interaction and magnetic field dependence of different angular momentum *L* states. Our initial suspect for the energy behavior is the following: the initial increase in

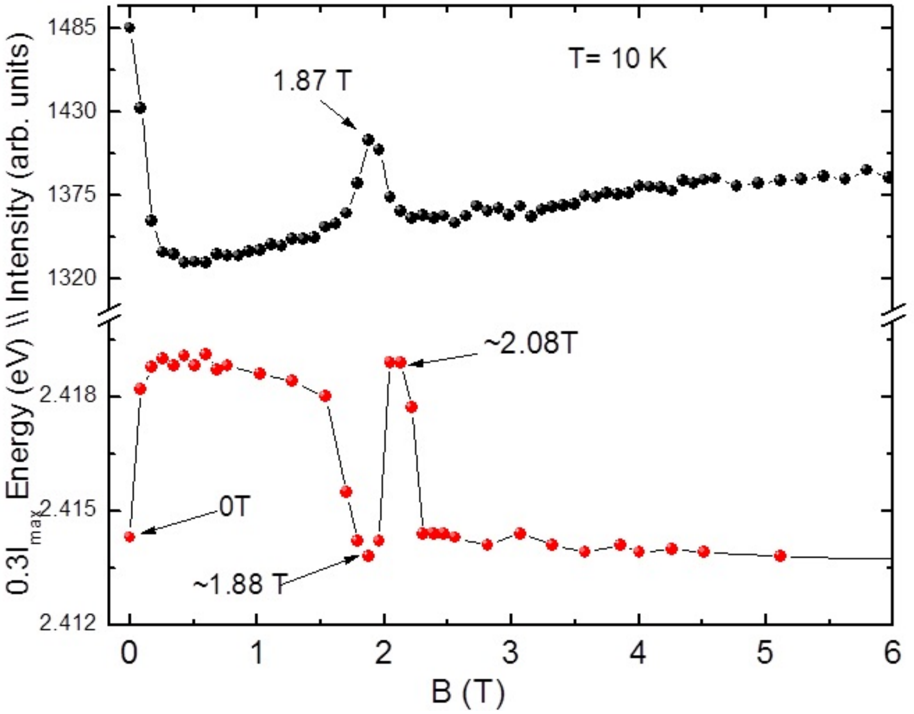

Figure 7.4: PL emission intensity (top panel) and energy (bottom panel) as a function of magnetic field for 30% of peak on the lower energy side.

emission energy with increasing magnetic is due to the magneto excitonic behavior (h-band energy is not affected much). We note, the measure and degree of such effect remain open for discussion. Right before the AB transition happens and the ‘Peak’ of intensity is observed, the e-h are ‘squeezed’ towards each other, intensity increases due to rise in overlap of e-h wavefunctions while due to increase in Coulomb attraction, total energy of emission drops. We note that this change in energy is ~ 2 to 4 meV. At the AB transition magnetic field, the drop in intensity is observed, but increase in energy is seen. Such an observation can be due to distribution of states and ‘anticrossing’ of states. Following the transition field, emission energy decreases which is expected after the transition.

More detailed and higher resolution experiments are needed to be performed to confirm such predictions along with self consistent theoretical modeling to understand the physics.

7.3 Outlook for Future Research

The material system; ZnTe/ ZnSe stacked QDs, studied here is fundamentally interesting. Owing to many complicated mechanisms and their interplay the scopes for future research are vast. Especially interesting are some of the following:

1. PL in the presence of externally applied electric field (i) parallel and (ii) perpendicular to the growth direction (normal to the sample). Such studies can reveal Stark shift and inverse Stark shift related effects.
2. PL measurements in the presence of externally applied magnetic field (Faraday geometry) and electric field (in-plane), to explore the possibility of controlling life-time of excitons and light storage application as predicted by Ref. [97].
3. Very low temperature ($\lesssim$ 2 K)PL and Magneto-PL, to observe effects after suppressing phonon related processes. This work will be done at the NHMFL, Tallahhassee, Fl.
4. Temperature dependent magneto-PL are under investigation and interesting observations at high magnetic fields are observed. Detailed studies on this matter is in progress.
5. Polarization dependent experiments will be done for obtaining information about spin dependent information.

Appendix

A Excitonic AB effect

A.1 Polarized Exciton

The Hamiltonian for the system of polarized exciton enclosing magnetic flux lines, describing the angular motion is [71]:

$$\begin{aligned}\hat{H}_{exc} = -\frac{\hbar^2}{2m_eR_e^2}\frac{\partial^2}{\partial\theta_e^2} - \frac{i\hbar\omega_e}{2}\frac{\partial}{\partial\theta_e} - \frac{\hbar^2}{2m_hR_h^2}\frac{\partial^2}{\partial\theta_h^2} + \frac{i\hbar\omega_h}{2}\frac{\partial}{\partial\theta_h} \\ +\frac{m_e\omega_e^2R_e^2 + m_h\omega_h^2R_h^2}{8} + u_c(|\theta_e - \theta_h|)\end{aligned} \tag{0.1}$$

where $m_{e,h}$ are the e and h effective masses, $\omega_{e(h)} = |e|B/(m_{e(h)}c)$ are the cyclotron frequencies of $e(h)$, B is the magnetic field and u_c is the Coulomb potential (averaged over the radial co-ordinate).

Depending on the strength of the e-h coupling (Figure 2.2) different energy behavior are predicted [71]. In the case of weak coupling, the e and h can be seen in single particle view; the excitonic energy is obtained [71] to be:

$$E_{exc} = E_{exc0} + \frac{\hbar^2}{2m_eR_e^2}\left(l_e + \frac{\Phi_e}{\Phi_0}\right)^2 + \frac{\hbar^2}{2m_hR_h^2}\left(l_h + \frac{\Phi_h}{\Phi_0}\right)^2 \tag{0.2}$$

where $\Phi_{e,h} = \pi R_{e,h}^2 B$ is the magnetic flux with R_e and R_h are the radius of the e and h orbits, respectively. As the magnetic flux increases, the ground state $(l_e, l_h) = (0, 0)$ successively changes in favor of other states: (0,+1), (-1,+1), (-1,+2), producing a sequence of ground state total angular momentum values of $L = l_e + l_h = 0, 1, 0, 1$ and so on (Note that the total angular momentum is conserved whereas l_e and l_h

are not good quantum numbers). In this case multiple oscillations in both energy and intensity of PL emission are expected [71]. When strong coupling of e and h is considered, Coulomb interaction is important and the system is seen as a 'rotating dipole'. The energy is given by:

$$E_{exc} = E_{exc0} + \frac{\hbar^2}{2MR_0^2}\left(L + \frac{\Delta\Phi}{\Phi_0}\right)^2 \tag{0.3}$$

where $L = l_e + l_h$; $R_0 = \frac{R_e+R_h}{2}$; $M = \frac{m_e R_e^2 + m_h R_h^2}{R_0^2}$ and the net magnetic flux through the area between the trajectories is:

$$\Delta\Phi = \pi(R_e^2 - R_h^2)B = 2\pi(R_e - R_h)R_0 B \tag{0.4}$$

In this case, as the flux increases, the ground state changes successively from $L = 0$ to 1, 2, 3 and so on which leads to single oscillation in PL emission intensity due to transition of angular momentum states from 'bright' ($L = 0$) to 'dark' (L is non zero) state. The 'dark' excitons are expected to possess significantly longer recombination lifetime due to forbidden optical transition.

Furthermore, in the case of strong hole confinement, $R_h \to 0$, so equation 0.3 gives:

$$E_{exc} = E_{exc0} + \frac{\hbar^2}{2MR_e^2}\left(L + \frac{\Phi_e}{\Phi_0}\right)^2 \tag{0.5}$$

where $\Phi_e = \pi R_e^2 B$, which is the case for disk-like type-II QDs as discussed in Section 3.3.

A.2 Neutral Exciton

Starting from the general Hamiltonian 2.18, considering a special case as described by Römer et. al, [72]

$$r_e = r_h = \rho$$

the implication of which is that $\Delta\Phi = 0$ (as in ref. [71]). Due to the finite size of the exciton, flux sensitivity emerges via AB effect. This effect is demonstrated by oscillations both in the energy and in the oscillator strength (relates to the intensity of PL emission) of the exciton absorption.

The problem has been approached in the following manner using perturbative method; In the absence of e and h interaction, the wave functions of electrons and holes are given by

$$\Psi_N^e(\theta_e) = \frac{1}{\sqrt{2\pi}} e^{iN\theta_e}; \Psi_N^h(\theta_h) = \frac{1}{\sqrt{2\pi}} e^{iN'\theta_h} \tag{0.6}$$

where N and N' are integers. The corresponding energies are:

$$E_N^{(e)} = \frac{\hbar^2}{2m_e\rho^2}\left(N - \frac{\Phi}{\Phi_0}\right)^2; E_N^{(h)} = \frac{\hbar^2}{2m_h\rho^2}\left(N' - \frac{\Phi}{\Phi_0}\right)^2 \tag{0.7}$$

where R is the radius of the ring, $m_{e(h)}$ is the effective mass of $e(h)$. Presence of an interaction potential $V[R(\theta_e - \theta_h)]$ is considered , where $R(\theta_e - \theta_h) = 2\rho \sin\frac{\theta_e - \theta_h}{2}$ is angular the distance between e and h. The excitonic trial wavefunction were taken of the form:

$$\Psi(\theta_e, \theta_h) = \sum_{N,N'} A_{N,N'} \Psi_N^e(\theta_h) \Psi_{N'}^h(\theta_h) \tag{0.8}$$

The coefficients $A_{N,N'}$ were found from the equation:

$$\sum_{N,N'} A_{N,N'}[E_N^{(e)} + E_N'^{(h)} - \Delta]\Psi_N^e(\theta_h)\Psi_{N'}^h(\theta_h) + V[R(\theta_e - \theta_h)]\Psi(\theta_e, \theta_h) \tag{0.9}$$

The interaction potential was approximated to a Dirac delta function

$$V_0\delta(\theta_e - \theta_h) \tag{0.10}$$

considering that only when the electron and hole are close together the interaction is significant.

Using the above and in the limit of large ρ, when

$$|V_0| \gg \epsilon_0 \qquad \text{where} \qquad \epsilon_0 = \frac{\hbar^2}{2\rho^2}\left(\frac{1}{m_e} + \frac{1}{m_h}\right) \tag{0.11}$$

the energy spectrum for ground state is given by:

$$E_{exc} = -\frac{\pi^2 V_0^2}{\epsilon_0}\left[1 + 4cos\left(\frac{2\pi\Phi}{\Phi_0}\right) exp\left(-\frac{2\pi^2|V_0|}{\epsilon_0}\right)\right]. \tag{0.12}$$

The second term in the brackets of equation 0.12 describes the excitonic AB effect in this picture. We note, however, the ‘oscillation’ here lies within the ground state for which total angular momentum of the system (N_0) is zero. Starting from the general Hamiltonian we discussed before and imposing $r_e = r_h \equiv \Delta\Phi = 0$ we see that the oscillations described in Govorov's paper do not appear here. Moreover, we note that the total angular momentum $N_0 = N + N' \neq 0$ has not been addressed in this picture.

From the general Hamiltonian for the case $\Delta\Phi = 0$ we notice that H_{θ_0} reduces to

$$H = \frac{\hbar^2}{2MR_\theta^2}(-i\partial\theta_0)^2$$

The H_{int} part of the Hamiltonian (in is flux dependent and produces oscillations as seen in equation 0.12.

Further modifications upon this approach including numerical analysis in the presence of a specific potential [105] and tunability of this effect via application of external in-plane electric field [97] for excitonic storage and an experimental interpretation of AB oscillation in the presence of built-in electric field [96] has been reported.

A.3 Excitonic AB phase

The general Hamiltonian (2.18) can be rewritten in the form:

$$H = \left[-\frac{\hbar^2}{2MR_0^2}\partial^2_{\theta_0} - \frac{\hbar^2}{2}\frac{MR_0^2}{m_e R_e^2 m_h R_h^2}\partial^2_\Delta\right] - \left[\frac{i\hbar|e|}{2\pi}\left(\frac{\Phi_e}{m_e R_e^2}\partial_{\theta_e} - \frac{\Phi_h}{m_h R_h^2}\partial_{\theta_h}\right)\right] + U_c \tag{0.13}$$

We study here two cases in the settings of magnetic flux conditions (in the presence and absence of magnetic field at the site of the exciton) to learn about the similarities and differences arising in context of the AB-effect.

Case 1: For $\Phi_e = \Phi_h = \Phi$. At first we specialize the second term in the Hamiltonian:

$$-\frac{i\hbar|e|}{2\pi}\Phi\left[\frac{m_h R_h^2 + m_e R_e^2}{m_e R_e^2 m_h R_h^2}\partial_\Delta + \frac{1}{MR_0^2}\left(\partial_{\theta_e} - \partial_{\theta_h}\right)\right] \tag{0.14}$$

The contribution to the energy from the angular part is similar to equation 0.3, only that in this case $\Delta\Phi = 0$. Therefore there is no AB-like effect through this term.

Now lets consider the remaining part of the Hamiltonian (note that this part is absent for a fixed dipole because then there is no internal dynamics).

$$H_\Delta = -\frac{\hbar^2}{2}\left[\frac{MR_0^2}{m_e R_e^2 m_h R_h^2}\partial_\Delta^2 + \frac{2i|e|\Phi}{2\pi\hbar}\frac{MR_0^2}{m_e R_e^2 m_h R_h^2}\partial_\Delta\right] + U_c$$

$$= -\frac{\hbar^2}{2}\frac{MR_0^2}{m_e R_e^2 m_h R_h^2}\left[\partial_\Delta^2 \frac{2i|e|\Phi}{2\pi\hbar}\partial_\Delta\right] + U_c \tag{0.15}$$

Indeed the eigen wavefunction can be redefined to the form:

$$\psi_\Delta = \exp\left[-\frac{i|e|\Phi\Delta}{2\pi\hbar}\right]\psi(\Delta) \tag{0.16}$$

which clearly carries the Berry- phase.

Case 2: Now considering the situation with $\Phi_e \neq \Phi_h$; The angular part of the Hamiltonian:

$$-\frac{i\hbar|e|}{2\pi}B\pi\left[\frac{1}{m_e}\partial_{\theta_e} - \frac{1}{m_h}\partial_{\theta_h}\right] = -\frac{i\hbar|e|}{2\pi}\left[\frac{B\pi}{M}\partial_\Delta + \frac{\Delta\Phi}{MR_0^2}\right] \tag{0.17}$$

The energy eigen values consist of the AB- like term due to $\Delta\Phi \neq 0$. Also, the wavefunction is of the form:

$$\psi(\theta_0) = \exp\left[-\frac{i|e|\Delta\Phi\theta_0}{2\pi\hbar}\right]\exp[-i\theta_0 L]\psi(\Delta) \tag{0.18}$$

which carry the Berry- like phase factor dependent on $\Delta\Phi$. The AB-effect, thus is seen through angular part of the Hamiltonian.

Considering the remaining (internal) part of the Hamiltonian,

$$H_\Delta = -\frac{\hbar^2}{2}\frac{MR_0^2}{m_e R_e^2 m_h R_h^2}\partial_\Delta^2 - \frac{i\hbar|e|}{2\pi}\frac{B\pi}{M}\partial_\Delta + U_c(|\Delta|)$$

$$= -\frac{\hbar^2}{2}\left[\frac{MR_0^2}{m_e R_e^2 m_h R_h^2}\partial_\Delta^2 + \frac{2i|e|B}{2\hbar M}\partial_\Delta\right] + U_c \tag{0.19}$$

with

$$H_\Delta^{B=0}\psi = -\frac{\hbar^2}{2}a^2\partial_\Delta^2 - \frac{\hbar^2}{2}b^2 + U_c \tag{0.20}$$

the wavefunction can be written in the form:

$$\psi = e^{-\frac{ib}{a}\Delta}\psi(\Delta) \tag{0.21}$$

where

$$\frac{b}{a} = \frac{m_e R_e^2 m_h R_h^2}{MR_0^2}\frac{|e|B}{2\hbar}\frac{m_e + m_h}{m_e m_h}$$

Clearly, this is not a Berry-phase effect.

We note that to completely solve the internal Hamiltonian would require numerical calculations which remain beyond the scope of this work.

B Cylindrical potential well problem with finite barrier

Let's consider the problem of cylindrical potential well defined as given below,

$$
\begin{aligned}
V(r, z, \phi) &= -V_0 && -a \leq r \leq a \\
&= 0 && \text{otherwise}
\end{aligned}
$$

Also the height of the well is L.

The Schr"oedinger equation for holes is

$$-\frac{\hbar^2}{2m}\nabla^2\psi + V\psi = E\psi$$

Using $\psi = R(r)Z(z)\Phi(\phi)$ we get

$$Z(z) = A_1 \sin k_z z$$

with $k_z = \frac{n_z \pi}{L}$ where n_z takes non-zero positive integer values. Similarly the angular part gives

$$\Phi(\phi) = Be^{im\phi}$$

The radial part satisfies Bessel's equation whose solutions are

$$R(\rho) = C_1 J_m(\rho) + C_2 N_m(\rho)$$

Here $\rho = Kr$ with $K^2 = k_z^2 + k^2$ and $k = \sqrt{\frac{2m(E+V_0)}{\hbar^2}}$. Hence the full solution is

$$
\begin{aligned}
\psi_{inside} &= C \sin k_z z e^{im\phi} J_m(\sqrt{k^2 - k_z^2} r) && -a \leq r \leq a \\
\psi_{outside} &= A \sin k_z z e^{im\phi} N_m(\sqrt{k^2 - k_z^2} r) && \text{otherwise}
\end{aligned}
$$

The coefficient C is given by

$$C = A\frac{N_0(Ka)}{J_0(Ka)}$$

The energy spectrum of the problem is given by

$$E = \frac{\hbar^2}{2m}\left[x_{ms}^2 + \frac{n_z^2\pi^2}{L^2}\right] - V_0 \tag{0.22}$$

with x_{ms} being the solution for K of the following equation:

$$\frac{J_1(Ka)}{J_0(Ka)} = \frac{N_1(Ka)}{N_0(Ka)}$$

The solutions can be obtained numerically the above equation and by finding the intersection points $K = x_{ms}$.

We obtained solutions for $m = 0$ and $s = 1$ (i.e. the first crossing point) for realistic values of $a \sim 9$ to 11 nm, $m_h^* = 0.6m_e$ for effective mass of hole in ZnTe and $L \sim 1$ nm, to observe that the change in energy is merely $\sim$ 0.1 to 0.2 meV.

Bibliography

[1] O. Madelung. *Semiconductors: Data Handbook*. Springer, 3rd edition, 2004.

[2] D. Lee, A. Mysyrowicz, A. V. Nurmikko, and B. J. Fitzpatrick. Exciton self-trapping in ZnSe-ZnTe alloys. *Phys. Rev. Lett.*, **58**, 1475, 1987.

[3] K. Suzuki, U. Neukirch, J. Gutowski, N. Takojima, T. Sawada, and K. Imai. Recombination kinetics of S1 and S2 bands in ZnSe-ZnTe superlattices. *Journal of Crystal Growth*, **184**, 882–885, 1998.

[4] J. Phillips. Evaluation of the fundamental properties of quantum dot infrared detectors. *J. of Appl. Phys.*, **91**, 4590–4594, 2002.

[5] B. Julsgaard, J. Sherson, J.I. Cirac, J. Fiurasek, and E.S. Polzik. Experimental demonstration of quantum memory for light. *Nature*, **432** (7016), 482–486, 2004.

[6] A. I. Lvovsky, B. C. Sanders, and W. Tittel. Optical quantum memory. *Nature Photonics*, **3** (12), 706–714, 2009.

[7] M. P. Hedges, J. J. Longdell, Y. Li, and M. J. Sellars. Efficient quantum memory for light. *Nature*, **465** (7301), 1052–1056, 2010.

[8] K. F. Reim, J. Nunn, V. O. Lorenz, B. J. Sussman, K. C. Lee, N. K. Langford, D. Jaksch, and I. A. Walmsley. Towards high-speed optical quantum memories. *Nature Photonics*, **4** (4), 218–221, 2010.

[9] H.J. Briegel, W. Dur, J.I. Cirac, and P. Zoller. Quantum repeaters: The role of imperfect local operations in quantum communication. *Phys. Rev. Lett.*, **81** (26), 5932–5935, 1998.

[10] L. V. Hau, S. E. Harris, Z. Dutton, and C. H. Behroozi. Light speed reduction to 17 metres per second in an ultracold atomic gas. *Nature*, **397** (6720), 594–598, Feb 18 1999. ISSN 0028-0836. doi: {10.1038/17561}.

[11] T. F. Krauss. Why do we need slow light? *Nature Photonics*, **2** (8), 448–450, aug 2008. ISSN 1749-4885. doi: {10.1038/nphoton.2008.139}.

[12] B. Wu, J. F. Hulbert, E. J. Lunt, K. Hurd, A. R. Hawkins, and H. Schmidt. Slow light on a chip via atomic quantum state control. *Nature Photonics*, **4** (11), 776–779, 2010.

[13] N. Akopian, L. Wang, A. Rastelli, O. G. Schmidt, and V. Zwiller. Hybrid semiconductor-atomic interface: slowing down single photons from a quantum dot. *Nature Photonics*, **5** (4), 230–233, 2011. ISSN 1749-4885. doi: {10.1038/NPHOTON.2011.16}.

[14] F. Malonga, D. Bertho, C. Jouanin, and J. M. Jancu. Tight-binding study of ZnSe/ZnTe strained superlattices: Determination of the band offset from the optical properties. *Phys. Rev. B*, **52**, 5124, 1995.

[15] J. R. Madureira, M. P. F. de Godoy, M. J. S. P. Brasil, and F. Iikawa. Spatially indirect excitons in type-II quantum dots. *Appl. Phys. Lett.*, **90**, 212105–3, 2007.

[16] C. Y. Jin, H. Y. Liu, S. Y. Zhang, Q. Jiang, S. L. Liew, M. Hopkinson, T. J. Badcock, E. Nabavi, and D. J. Mowbray. Optical transitions in type-II InAs/-GaAs quantum dots covered by a GaAsSb strain-reducing layer. *Appl. Phys. Lett.*, **91**, 021102–3, 2007.

[17] I. L. Kuskovsky, W. MacDonald, A. O. Govorov, L. Muroukh, X. Wei, M. C.

Tamargo, M. Tadic, and F. M. Peeters. Optical Aharonov-Bohm effect in stacked type-II quantum dots. *Phys. Rev. B*, **76**, 035342, 2007.

[18] Z. I. Alferov. Nobel lecture: The double heterostructure concept and its applications in physics, electronics, and technology. *Rev. Mod. Phys.*, **73**, 767, 2001.

[19] O. Aktas, Z. F. Fan, S. N. Mohammad, A. E. Botchkarev, and H. Morkoc. High temperature characteristics of AlGaN/GaN modulation doped field effect transistors. *Appl. Phys. Lett.*, **69** (25), 3872 –3874, dec 1996.

[20] W. Liu. *Heterostructure bipolar transistors*. CRC Press, Inc., 2003. From *RF and microwave semiconductor device handbook*, by M. Golio.

[21] G.L. Patton, S.S. Iyer, S.L. Delage, S. Tiwari, and J.M.C. Stork. Silicon-germanium base heterojunction bipolar transistors by molecular beam epitaxy. *Electron Device Letters, IEEE*, **9** (4), 165 –167, april 1988.

[22] M. T. Bjork, B. J. Ohlsson, C. Thelander, A. I. Persson, K. Deppert, L. R. Wallenberg, and L. Samuelson. Nanowire resonant tunneling diodes. *Appl. Phys. Lett.*, **81** (23), 4458 –4460, dec 2002. ISSN 0003-6951. doi: 10.1063/1.1527995.

[23] B. L. Sharma and R. K. Purohit. *Semiconductor heterojunctions*. Pergamon Press Oxford, New York, 1st edition, 1974. ISBN 0080177476.

[24] S. J. Choi, K. Djordjev, S. J. Choi, P. D. Dapkus, W. Lin, G. Griffel, R. Menna, and J. Connolly. Microring resonators vertically coupled to buried heterostructure bus waveguides. *IEEE Journal of Lightwave Technology*, **16** (3), 828–830, mar 2004.

[25] K. Djordjev, S. J. Choi, S. J. Choi, and P. D. Dapkus. Active semiconductor microdisk devices. *IEEE Journal of Lightwave Technology*, **20** (1), 105–113, 2002.

[26] K. Kasahara, Y. Tashiro, N. Hamao, M. Sugimoto, and T. Yanase. Double heterostructure optoelectronic switch as a dynamic memory with low-power consumption. *Appl. Phys. Lett.*, **52** (9), 679–681, 1988. doi: 10.1063/1.99345. URL `http://link.aip.org/link/?APL/52/679/1`.

[27] Y. Honda, I. Suemune, N. Yasuhira, and M. Yamanishi. A new optoelectronic device based on modulation-doped heterostructure: demonstration of functions as both lateral current injection laser and junction field effect transistor. *Photonics Technology Letters, IEEE*, **2** (12), 881 –883, dec. 1990. ISSN 1041-1135. doi: 10.1109/68.62017.

[28] R. Kohler, A. Tredicucci, F. Beltram, H. E. Beere, E. H. Linfield, A. G. Davies, D. A. Ritchie, R. C. Iotti, and F. Rossi. Terahertz semiconductor-heterostructure laser. *Nature*, **417** (6885), 156–159, May 2002. ISSN 0028-0836. doi: 10.1038/417156a. URL `http://dx.doi.org/10.1038/417156a`.

[29] S. J. Choi, K. Djordjev, S. J. Choi, and P. D. Dapkus. Microdisk lasers vertically coupled to output waveguides. *IEEE Photonics Technology Letters*, **15** (10), 1330–1332, October 2003.

[30] G. H. Wannier. The structure of electronic excitation levels in insulating crystals. *Phys. Rev.*, **52**, 191–197, Aug 1937. doi: 10.1103/PhysRev.52.191. URL `http://link.aps.org/doi/10.1103/PhysRev.52.191`.

[31] J. Frenkel. On the transformation of light into heat in solids. I. *Phys. Rev.*, **37**, 17–44, Jan 1931. doi: 10.1103/PhysRev.37.17. URL `http://link.aps.org/doi/10.1103/PhysRev.37.17`.

[32] J. Frenkel. On the transformation of light into heat in solids. II. *Phys. Rev.*, **37**, 1276–1294, May 1931. doi: 10.1103/PhysRev.37.1276. URL `http://link.aps.org/doi/10.1103/PhysRev.37.1276`.

[33] R. J. Elliott. Intensity of optical absorption by excitons. *Phys. Rev.*, **108**, 1384–1389, Dec 1957. doi: 10.1103/PhysRev.108.1384. URL `http://link.aps.org/doi/10.1103/PhysRev.108.1384`.

[34] J. I. Pankove. *Optical processes in semiconductors.* Englewood Cliffs, N.J. : Prentice-Hall, 1971. ISBN 0136380239. Includes bibliographical references.

[35] P. Y. Yu and M. Cardona. *Fundamentals of Semiconductors: Physics and Materials Properties.* Springer, 2005. ISBN 3540254706. URL `http://www.worldcat.org/isbn/3540254706`.

[36] N. N. Ledentsov, J. Böhrer, M. Beer, F. Heinrichsdorff, M. Grundmann, D. Bimberg, S. V. Ivanov, B. Ya. Meltser, S. V. Shaposhnikov, I. N. Yassievich, N. N. Faleev, P. S. Kop'ev, and Zh. I. Alferov. Radiative states in type-II GaSb/GaAs quantum wells. *Phys. Rev. B*, **52**, 14058–14066, 1995.

[37] F. Hatami, M. Grundmann, N. N. Ledentsov, F. Heinrichsdorff, R. Heitz, J. Böhrer, D. Bimberg, S. S. Ruvimov, P. Werner, V. M. Ustinov, P. S. Kop'ev, and Zh I. Alferov. Carrier dynamics in type-II GaSb/GaAs quantum dots. *Phys. Rev. B*, **57** (8), 4635, 1998.

[38] T. Baier, U. Mantz, K. Thonke, R. Sauer, F. Schäffler, and H.-J. Herzog. Type-II band alignment in $\mathrm{Si/Si_{1-x}Ge_x}$ quantum wells from photoluminescence line shifts due to optically induced band-bending effects: Experiment and theory. *Phys. Rev. B*, **50** (20), 15191, 1994.

[39] Y. Gu, I. L. Kuskovsky, M. van der Voort, G. F. Neumark, X. Zhou, and M. C. Tamargo. Zn-Se-Te multilayers with submonolayer quantities of Te: Type-II quantum structures and isoelectronic centers. *Phys. Rev. B*, **71** (4), 045340–4, 2005.

[40] V. A. Shuvayev, I. L. Kuskovsky, L. I. Deych, Y. Gu, Y. Gong, G. F. Neumark, M. C. Tamargo, and A. A. Lisyansky. Dynamics of the radiative recombination in cylindrical nanostructures with type-II band alignment. *Phys. Rev. B*, **79**, 115307, 2009.

[41] L. M. Roth, B. Lax, and S. Zwerdling. Theory of optical magneto-absorption effects in semiconductors. *Phys. Rev.*, **114**, 90–104, 1959.

[42] N. Miura. *Physics of semiconuctors in high magnetic fields.* Oxford University Press, 2008.

[43] J. J. Hopfield and D. G. Thomas. Fine structure and magneto-optic effects in the exciton spectrum of cadmium sulfide. *Phys. Rev.*, **122** (1), 35, 1961.

[44] N. Miura, H. Kunimatsu, K. Uchida, Y. Matsuda, T. Yasuhira, H. Nakashima, Y. Sakuma, Y. Awano, T. Futatsugi, and N. Yokoyama. Magneto-optical study of excitons in quantum wells, wires and dots in high magnetic fields. *Physica B: Condensed Matter*, **256-258**, 308–318, 1998.

[45] R. Rinaldi, P. V. Giugno, R. Cingolani, H. Lipsanen, M. Sopanen, J. Tulkki, and J. Ahopelto. Zeeman effect in parabolic quantum dots. *Phys. Rev. Lett.*, **77** (2), 342, 1996.

[46] Th. Wimbauer, K. Oettinger, Al. L. Efros, B. K. Meyer, and H. Brugger. Zeeman splitting of the excitonic recombination in $\mathrm{In}_x\mathrm{Ga}_{1-x}\mathrm{As}$/GaAs single quantum wells. *Phys. Rev. B*, **50** (12), 8889, 1994.

[47] M. Hayne and B. Bansal. High-field magneto-photoluminescence of semiconductor nanostructures. *Luminescence*, **27** (3), i–i, 2012. ISSN 1522-7243. doi: 10.1002/bio.2399. URL `http://dx.doi.org/10.1002/bio.2399`.

[48] Y. Gong, W. MacDonald, G. F. Neumark, M. C. Tamargo, and I. L. Kuskovsky. Optical properties and growth mechanism of multiple type-II ZnTe/ZnSe quantum dots grown by migration-enhanced epitaxy. *Phys. Rev. B*, **77** (15), 155314–6, 2008.

[49] Y. Aharonov and D. Bohm. Significance of electromagnetic potentials in the quantum theory. *Phys. Rev.*, **115** (3), 485, 1959.

[50] J. J. Sakurai. *Modern Quantum Mechanics (Revised Edition).* Addison Wesley, 1st edition, 1993. ISBN 0201539292.

[51] B. H. Bransden and C. J. Joachain. *Quantum Mechanics.* Prentice Hall, second edition, 2000.

[52] D. J. Griffiths. *Introduction to quantum mechanics*. Pearson Prentice Hall, 2 edition, 2005.

[53] M. V. Berry. Quantal phase factors accompanying adiabatic changes. *Proc. R. Soc. of London*, **392** (1802), 45–57, 1984.

[54] R. G. Chambers. Shift of an electron interference pattern by enclosed magnetic flux. *Phys. Rev. Lett.*, **5**, 3–5, Jul 1960. doi: 10.1103/PhysRevLett.5.3. URL `http://link.aps.org/doi/10.1103/PhysRevLett.5.3`.

[55] M. Peshkin. The Aharonov-Bohm Effect - Why it cannot be eliminated from Quantum-Mechanics. *Physics Reports - Review Section of Physics Letters*, **80** (6), 375–386, 1981.

[56] M. Peshkin and A. Tonomura. *The Aharonov-Bohm Effect*. Springer, 1989.

[57] R. A. Webb, S. Washburn, C. P. Umbach, and R. B. Laibowitz. Observation of Aharonov-Bohm oscillations in normal-metal rings. *Phys. Rev. Lett.*, **54**, 2696–2699, Jun 1985. doi: 10.1103/PhysRevLett.54.2696. URL `http://link.aps.org/doi/10.1103/PhysRevLett.54.2696`.

[58] M. Buttiker, Y. Imry, and M. Ya. Azbel. Quantum oscillations in one-dimensional normal-metal rings. *Phys. Rev. A*, **30**, 1982–1989, Oct 1984. doi: 10.1103/PhysRevA.30.1982. URL `http://link.aps.org/doi/10.1103/PhysRevA.30.1982`.

[59] Y. Gefen, Y. Imry, and M. Ya. Azbel. Quantum oscillations and the Aharonov-Bohm effect for parallel resistors. *Phys. Rev. Lett.*, **52**, 129–132, Jan 1984. doi: 10.1103/PhysRevLett.52.129. URL `http://link.aps.org/doi/10.1103/PhysRevLett.52.129`.

[60] M. Buttiker, Y. Imry, R. Landauer, and S. Pinhas. Generalized many-channel conductance formula with application to small rings. *Phys. Rev. B*, **31**, 6207–6215, May 1985. doi: 10.1103/PhysRevB.31.6207. URL `http://link.aps.org/doi/10.1103/PhysRevB.31.6207`.

[61] G. Timp, A. M. Chang, J. E. Cunningham, T. Y. Chang, P. Mankiewich, R. Behringer, and R. E. Howard. Observation of the Aharonov-Bohm effect for $\omega_c\tau > 1$. *Phys. Rev. Lett.*, **58**, 2814–2817, Jun 1987. doi: 10.1103/PhysRevLett.58.2814. URL `http://link.aps.org/doi/10.1103/PhysRevLett.58.2814`.

[62] C. J. B. Ford, T. J. Thornton, R. Newbury, M. Pepper, H. Ahmed, D. C. Peacock, D. A. Ritchie, J. E. F. Frost, and G. A. C. Jones. Electrostatically defined heterojunction rings and the Aharonov-Bohm effect. *Appl. Phys. Lett.*, **54** (1), 21–23, 1989. doi: 10.1063/1.100818. URL `http://link.aip.org/link/?APL/54/21/1`.

[63] A. Fuhrer, S. Luscher, T. Ihn, T. Heinzel, K. Ensslin, W. Wegscheider, and M. Bichler. Energy spectra of quantum rings. *Nature*, **413** (6858), 822–825, October 2001. ISSN 0028-0836. doi: 10.1038/35101552. URL `http://dx.doi.org/10.1038/35101552`.

[64] J. Yau, E. P. De Poortere, and M. Shayegan. Aharonov-Bohm Oscillations with Spin: Evidence for Berry's Phase. *Phys. Rev. Lett.*, **88**, 146801, Mar 2002. doi: 10.1103/PhysRevLett.88.146801. URL `http://link.aps.org/doi/10.1103/PhysRevLett.88.146801`.

[65] L.C. Mur, C.J.P.M. Harmans, and W.G. van der Wiel. Competition between h/e and h/2e oscillations in a semiconductor Aharonov-Bohm interferometer. *New Journal of Physics*, **10**, 073031, 2008. URL `http://doc.utwente.nl/59273/`. Open access article.

[66] S. Viefers, P. Koskinen, P. Singha Deo, and M. Manninen. Quantum rings for beginners: energy spectra and persistent currents. *Physica E Low-Dimensional Systems and Nanostructures*, **21**, 1–35, feb 2004. doi: 10.1016/j.physe.2003.08.076.

[67] M. Wilkens. Quantum phase of a moving dipole. *Phys. Rev. Lett.*, **72** (1), 5–8, 1994. PRL.

[68] G. Spavieri. Quantum effect of the Aharonov-Bohm type for particles with an electric dipole moment. *Phys. Rev. Lett.*, **82** (20), 3932–3935, 1999. PRL.

[69] A. V. Chaplik. Magnetoexcitons in quantum rings and in antidots. *JETP Lett*, **62**, 900, 1995.

[70] A. B. Kalametsev, V. M. Kovalev, and A. O. Govorov. Magnetoexcitons in type-II quantum dots. *JETP Lett.*, **68**, 669 – 672, 1998.

[71] A. O. Govorov, S. E. Ulloa, K. Karrai, and R. J. Warburton. Polarized excitons in nanorings and the optical Aharonov-Bohm effect. *Phys. Rev. B*, **66**, 081309–13, 2002.

[72] R. A. Römer and M. E. Raikh. Aharonov-Bohm effect for an exciton. *Phys. Rev. B*, **62**, 7045–7049, 2000.

[73] K. L. Janssens, B. Partoens, and F. M. Peeters. Magnetoexcitons in planar type-II quantum dots in a perpendicular magnetic field. *Phys. Rev. B*, **64**, 155324, 2001.

[74] K.L. Janssens, B. Partoens, and F.M. Peeters. Type-II quantum dots in magnetic fields: excitonic behaviour. *Microelectronics Journal*, **34**, 347, 2003.

[75] M. Tadić, V. Arsoski, N. Čukarić, and F.M. Peeters. The optical excitonic Aharonov-Bohm effect in a few nanometer wide Type-I nanorings. *Acta Physica Polonica A*, **117**, 974–977, 2010.

[76] B. Li and F. M. Peeters. Tunable optical Aharonov-Bohm effect in a semiconductor quantum ring. *Phys. Rev. B*, **83** (11), 115448, 2011. PRB.

[77] E. Ribeiro, A. O. Govorov, W. Carvalho Jr, and G. Medeiros-Ribeiro. Aharonov-Bohm signature for neutral polarized excitons in Type-II quantum dot ensembles. *Phys. Rev. Lett.*, **92**, 126402–04, 2004.

[78] I. R Sellers, V. R. Whitesides, I. L. Kuskovsky, A. O. Govorov, and B. D. McCombe. Aharanov-Bohm excitons at elevated temperatures in type-II ZnTe/ZnSe quantum dots. *Phys. Rev. Lett.*, **100**, 136405, 2008.

[79] I. R. Sellers, V. R. Whiteside, A. O. Govorov, W. C. Fan, W. C. Chou, I. Khan, A. Petrou, and B. D. McCombe. Coherent Aharonov-Bohm oscillations in type-II (Zn,Mn)Te/ZnSe quantum dots. *Phys. Rev. B*, **77** (24), 241302, 2008. PRB.

[80] M. H. Degani, M. Z. Maialle, G. Medeiros-Ribeiro, and E. Ribeiro. Two-dimensional magnetoexcitons in type-II semiconductor quantum dots. *Phys. Rev. B*, **78**, 075322, 2008.

[81] B. Roy, H. Ji, S. Dhomkar, F. J. Cadieu, L. Peng, R. Moug, M. C. Tamargo, Y. Kim, D. Smirnov, and I. L. Kuskovsky. Enhancement and narrowing of the Aharonov-Bohm oscillations due to built-in electric field in stacked type-II ZnTe/ZnSe quantum dots: Spectral analysis. *Phys. Rev. B*, **86**, 165310, 2012.

[82] B. Roy, H. Ji, S. Dhomkar, F. J. Cadieu, L. Peng, R. Moug, M. C. Tamargo, and I. L. Kuskovsky. Determination of excitonic size with sub-nanometer precision via excitonic Aharonov-Bohm effect in type-II quantum dots. *Appl. Phys. Lett.*, **100**, 213114, 2012.

[83] B. Roy, H. Ji, S. Dhomkar, F. J. Cadieu, L. Peng, R. Moug, M. C. Tamargo, and I. L. Kuskovsky. Distinguishability of stacks in ZnTe/ZnSe quantum dots via spectral analysis of Aharonov-Bohm oscillations. *The European Physical Journal B*, **86**, 2013. ISSN 1434-6028. doi: 10.1140/epjb/e2012-30629-5.

[84] L. G. G. V. Dias da Silva, S. E. Ulloa, and A. O. Govorov. Impurity effects on the Aharonov-Bohm optical signatures of neutral quantum-ring magnetoexcitons. *Phys. Rev. B*, **70**, 155318–25, 2004.

[85] I. L. Kuskovsky, C. Tian, G. F. Neumark, J. E. Spanier, I. P. Herman, W. C. Lin, S. P. Guo, and M. C. Tamargo. Optical properties of delta -doped ZnSe:Te grown by molecular beam epitaxy: The role of tellurium. *Phys. Rev. B*, **63** (15), 155205, 2001.

[86] T. Yao, Y. Miyoshi, Y. Makita, and S. Maekawa. Growth rate and sticking coefficient of ZnSe and ZnTe grown by molecular beam epitaxy. *Jpn. J. Appl. Phys.*, **16**, 369, 1977.

[87] M.J.S.P. Brasil, R.E. Nahory, F.S. Turco-Sandroff, H.L. Gilchrist, and R.J. Martin. Evolution of the band gap and the dominant radiative recombination center versus the composition. *Appl. Phys. Lett.*, **58** (22), 2509, 1991. ISSN 00036951. URL `http://search.ebscohost.com.queens.ezproxy.cuny.edu:2048/login.aspx?direct=true&db=iih&AN=4345584&site=ehost-live`.

[88] M. C. K. Cheung, A. N. Cartwright, I. R. Sellers, B. D. McCombe, and I. L. Kuskovsky. Time-resolved photoluminescence of type-II quantum dots and isoelectronic centers in Zn-Se-Te superlattice structures. *Appl. Phys. Lett.*, **92**, 032106, 2008.

[89] E.R. Glaser, B.R. Bennett, B.V. Shanabrook, and R. Magno. Photoluminescence studies of self-assembled InSb, GaSb, and AlSb quantum dot heterostructures. *Appl. Phys. Lett.*, **68**, 3614–3616, 1996.

[90] Y. S. Chiu, M. H. Ya, W. S. Su, and Y. F. Chen. Properties of photoluminescence in type-II GaAsSb/GaAs multiple quantum wells. *J. Appl. Phys.*, **92**, 5810, 2002.

[91] S. Wei and A. Zunger. Chemical trends in band offsets of Zn- and Mn-based II-VI superlattices: d-level pinning and offset compression. *Phys. Rev. B*, **53**, R10457, 1996.

[92] H. Y. Liu, I. R. Sellers, T. J. Badcock, D. J. Mowbray, M. S. Skolnick, K. M. Groom, M. Gutierrez, M. Hopkinson, J. S. Ng, J. P. R. David, and R. Beanland. Improved performance of 1.3 μ m multilayer InAs quantum-dot lasers using a high-growth-temperature GaAs spacer layer. *Appl. Phys. Lett.*, **85**, 704–706, 2004.

[93] S. Tatarenko, B. Daudin, and D. B. Cunff. Zn and Te desorption from the (100) ZnTe surface. *Appl. Phys. Lett.*, **66**, 1773–1775, 1995.

[94] I. L. Kuskovsky, Y. Gong, G. F. Neumark, and M. C. Tamargo. Photoluminescence and magneto-optical properties of multilayered type-II ZnTe/ZnSe quantum dots. *Superlattices Microstruct.*, **47**, 87–92, 2010.

[95] B. Roy, A. Shen, M. Tamargo, and I. Kuskovsky. Effects of varying MBE growth conditions on layered Zn-Se-Te structures. *J. Electron. Mater.*, **40**, 1775–1780, 2011.

[96] M. D. Teodoro, V. L. Campo, V. Lopez-Richard, E. Marega, G. E. Marques, Y. Galvão Gobato, F. Iikawa, M. J. S. P. Brasil, Z. Y. AbuWaar, V. G. Dorogan, Yu. I. Mazur, M. Benamara, and G. J. Salamo. Aharonov-Bohm interference in neutral excitons: Effects of built-in electric fields. *Phys. Rev. Lett.*, **104**, 086401, 2010.

[97] A. M. Fischer, V. L. Campo Jr, M. E. Portnoi, and R. A. Romer. Exciton storage in a nanoscale Aharonov-Bohm ring with electric field tuning. *Phys. Rev. Lett.*, **102**, 096405–4, 2009.

[98] A. V. Maslov and D. S. Citrin. Enhancement of the Aharonov-Bohm effect of neutral excitons in semiconductor nanorings with an electric field. *Phys. Rev. B*, **67**, 121304, 2003.

[99] A. G. Kontos, N. Chrysanthakopoulos, M. Calamiotou, T. Kehagias, P. Komninou, and U. W. Pohl. Structural properties of ZnSe epilayers on (111) GaAs. *J. of Appl. Phys.*, **90** (7), 3301–3307, 2001.

[100] K. Hingerl, R. E. Balderas-Navarro, A. Bonanni, and D. Stifter. Influence of anisotropic in-plane strain on critical point resonances in reflectance difference data. *Papers from the 28th conference on the physics and chemistry of semiconductor interfaces*, **19** (4), 1650–1657, 2001.

[101] S. J. Kim, B.-C. Juang, W. Wang, J. R. Jokisaari, C.-Y. Chen, J. D. Phillips, and X. Q. Pan. Evolution of self-assembled type-II ZnTe/ZnSe nanostructures: Structural and electronic properties. *J. of Appl. Phys.*, **111** (9), 093524, 2012.

[102] V. Holý, G. Springholz, M. Pinczolits, and G. Bauer. Strain induced vertical and lateral correlations in quantum dot superlattices. *Phys. Rev. Lett.*, **83**, 356–359, 1999.

[103] U. Manna, I. C. Noyan, Q. Zhang, I. F. Salakhutdinov, K. A. Dunn, S. W. Novak, R. Moug, M. C. Tamargo, G. F. Neumark, and I. L. Kuskovsky. Structural properties and spatial ordering in multilayered ZnMgTe/ZnSe type-II quantum dot structures. *J. of Appl. Phys.*, **111** (3), 033516, 2012.

[104] L. Schweidenback, T. Ali, A. H. Russ, J. R. Murphy, A. N. Cartwright, A. Petrou, C. H. Li, M. K. Yakes, G. Kioseoglou, B. T. Jonker, and A. Govorov. Optical Aharonov-Bohm oscillations in InGaAs quantum wells. *Phys. Rev. B*, **85**, 245310, 2012.

[105] C. Gonzalez-Santander, F. Dominguez-Adame, and R. A. Römer. Excitonic Aharonov-Bohm effect in a two-dimensional quantum ring. *Phys. Rev. B*, **84**, 235103, 2011.